Description of Anisotropic Properties of Trabecular Bone

By

DEAN INGLIS, B. ENG.

A Thesis

Submitted to the School of Graduate Studies

in Partial Fulfilment of the Requirements

for the Degree

Doctor of Philosophy.

McMaster University

DOCTOR OF PHILOSOPHY (2001) **McMaster University**

(Civil Engineering) **Hamilton, Ontario**

TITLE: **Description of Anisotropic Properties of Trabecular Bone**

AUTHOR: **Dean Inglis, B. Eng. (McMaster University)**

SUPERVISORS: **Dr. S. Pietruszczak, Dr. C. E. Webber**

NUMBER OF PAGES: **xiv, 181**

Abstract

This thesis presents a comprehensive approach to numerical modelling of human bone. Bone has been shown, in general, to be a heterogeneous material with orthotropic symmetry. The geometric arrangement of its porous micro-structure can be detected by high resolution tomographic imaging and then characterized by a 'fabric tensor.' This tensorial measure of material fabric can be correlated with mechanical properties and subsequently employed within numerical analyses of bone. In this work, the fabric tensor is incorporated into an elastic constitutive framework and a novel failure criterion for bone is proposed, which is seen as an important contribution to the numerical analysis of bone within the finite element (FE) methodology. The identification of fabric from micro-computed tomography (micro-CT) images of representative bone samples is achieved by a unified computational framework, described by a language independent pseudo-code. As a contribution to the constitutive representation of bone material, a new measure of fabric is defined and then identified using synthetic data of simple geometric shapes and micro-CT scans of human trabecular bone.

The current potential for improvement in FE modelling of the mechanical behaviour of bone is illustrated through a discussion of bone fracture. The numerical analysis is an extension of the results presented in Pietruszczak et al. (1997, 1999) wherein a high resolution geometric model with heterogeneous distribution of orientation-dependent mechanical properties was employed. The use of the material model within a FE analysis is illustrated by a FE analysis pertaining to the prediction of fracture within a femur, under the simulated conditions of a fall to the hip. In particular, the distribution of damage within a femur is assessed under two porosity distributions, simulating a healthy and an aged bone.

Acknowledgments

I would like to begin by thanking my supervisor, Dr. Stan Pietruszczak, for his support on so many levels over the duration of my Ph.D. Not only has he helped in my academic pursuits and development, but he introduced me to the game of squash which has become a great source of diversion from the rigours of academic work. I am equally indebted to my co-supervisor, Dr. Colin Webber, who assisted with many components of the bone modelling work, who welcomed me into the Bone Interest Group discussions, and who contributed substantial financial support. I am grateful to him for providing the opportunity to pursue my interests in computer vision and image processing, which has now lead to a full time research and programming contract. I would also like to thank Dr. Dieter Stolle for his support and encouragement over the years and for his contagious enthusiasm for finite element programming.

There are a number of people to thank without whose technical expertise this project could not have been brought to fruition. Thanks to Mr. Peter Koudys for helping design and fabricate a phantom container, used for CT imaging, and for letting me store a cow femur, longer than was necessary, in his lab freezer. I would also like to acknowledge Dr. Claude Nahmias for his assistance with the spiral CT imaging of the (human) femur. Thanks to Dr. Chris Gordon for providing access to and explaining the MUMC display system and his contour extraction codes, and for the opportunity to work with him as an interface designer. Thanks also to Ms. Anna Robertson for her assistance in accurately measuring the density of several of the phantom compartments. Many thanks to Dr. Ralph Mueller for donating two superb 3D micro-CT images of trabecular bone biopsies, which were used in the sections on fabric detection. Thanks also to Dr. Anders Odgaard for his e-mail discussion on fabric detection and for providing a copy of his detection source code. Finally, I would like to

thank Dr. Gyan Pande for his support and for our discussions on fabric detection while I was in Swansea, UK.

I would be remiss if I did not acknowledge my friend Rudy who provided welcome and well-timed distractions, and to his wife Arlene for her expert advice on matters of employment and for providing financial support through CPEC. Many thanks to Spencer, particularly for his advice and criticisms of the early drafts of the thesis, and for being a sounding board nearly every day on our journeys back and forth to McMaster.

I would also like to acknowledge the financial support of the Department of Civil Engineering at McMaster.

Finally, I would like to thank my wife, Erin, for her undying commitment and support during the last nine years of both undergraduate and graduate work.

Table of Contents

List of Figures

List of Tables

CHAPTER 1 Introduction and Background

The specification of the mechanical state at which fracture is induced in bone tissue is essential for the evaluation of the risk of hip and other bone fractures. It is also important for developing a deeper understanding of the process of healing and the repair of bone. Moreover, there are numerous orthopaedic design applications and clinical problems which require an in-depth understanding of the mechanics of bone interaction with synthetic materials. To gain insight into these and other complex biomechanical problems, numerical modelling techniques are generally employed. Analytical solutions are difficult, if not impossible, to obtain due to the inherent difficulty in modelling bone material and the complex geometry and boundary conditions of typical problems. A technique which has been widely accepted in the biomechanics community and which is well suited to such problems is the finite element (FE) method.

The literature review in this chapter will demonstrate that numerical analyses of bone related problems have, in general, been lacking in geometric resolution and constitutive representation. In light of this, the primary objective of this research was to implement and evaluate a new constitutive model and failure criterion for anisotropic bone. Numerical studies using FE analysis were conducted in order to investigate the biomechanical problem of fracture risk in the proximal femur. Using X-ray computed tomography (CT), image processing and solid modelling techniques, a realistic geometric model of a human femur was created and then meshed for the numerical studies. The FE analyses of a healthy and of a simulated osteoporotic femur were conducted and discussed within the context of the distribution of a suitably defined failure parameter. A related objective was to develop new methods for detecting the principal directions of material symmetry of representative bone

specimens in order to quantify certain components of the constitutive formulation mentioned above.

A brief description of bone tissue in terms of its salient features is provided in section 1.1. Bone, in general, is considered to be an anisotropic, heterogeneous material. The mechanical properties of bone, described in section 1.2, have been shown in the literature to depend on the geometric arrangement of bone's porous micro-structure, or 'fabric.' A tensorial measure of bone architecture, known as a 'fabric tensor,' is introduced in section 1.3 which sufficiently characterizes the elastic symmetry of bone. The desirability of a fabric-based description of bone constitutive properties within FE analyses is discussed in section 1.4 within the context of a biomechanical problem which has received considerable attention over the last decade: fracture prediction in the proximal femur. The final section of this chapter, section 1.5, summarizes the general scope and purpose of this research.

1.1 General Characteristics of Bone

Bone is a living, self-regulating material with geometric and material characteristics which change over time. The focus of the present research is on the description of mechanical properties of bone without incorporating the remodelling aspects of bone behaviour. Bone may be broadly classified into two distinct types of tissue; cortical and trabecular (or cancellous). These tissues are distinguished primarily by the composition and geometric arrangement of their basic cellular components. The organic matrix of both tissues is composed of collagen fibres and ground substance which is mineralised to various degrees by hydroxyapatite and other mineral substances. Macroscopically, cortical bone is comprised of closely packed cylindrical cells, known as osteons, which are themselves composed of concentrically arranged lamellae interlaced with a network of microscopic

blood vessels traversing axially and radially outward. The osteons are packed together and form the hard outer shell of most skeletal structures. Trabecular bone is considerably different. It is composed of a network of interconnected rod- and plate-like elements, known as trabeculae, with marrow occupying the void spaces in between. In addition, smaller ellipsoidal voids called lacunae are found within the solid matrix of both tissues. These voids are interconnected to one another and to the larger vessels by small tunnels called canaliculae. The two types of bone tissue may be roughly distinguished in terms of their porosity; for cortical bone, $\eta \approx\leq 40\,\%$ while for trabecular bone, $\eta \approx\geq 70\,\%$ (Martin, 1982). Alternatively, a distinction may be made based on apparent density; for cortical bone, $\rho_a \approx (1.7 - 2.0)\,g\,cm^{-3}$ while for trabecular bone, $\rho_a \approx (0.1 - 0.3)\,g\,cm^{-3}$ (Keller, 1994). Given such a wide range of structural composition, it is not surprising, then, that bone material is a heterogeneous substance. That is, the mechanical properties of bone vary from one bone to another as well as regionally within the same bone (Evans, 1973; Goldstein et al., 1983; Ashman et al., 1989).

1.1.2 The Mechanical Properties of Bone

Bone has been classified as having isotropic, transversely isotropic or orthotropic elastic symmetry. There are increasing difficulties with identifying the elastic constants of higher material symmetry groups. For example, an isotropic material requires the identification of two independent elastic constants; a transversely isotropic material requires five constants; and an orthotropic one requires nine constants. Initial research into bone properties focussed on developing a correlation between bulk mechanical properties (i.e., Young's modulus) and various, easily identifiable, physical parameters such as density, porosity, or mineral content. Schaffler et al. (1988) developed power law relations between the elastic modulus, porosity and apparent density for compact bone using least squares analyses of data obtained from

simple mechanical tests. Similarly, Currey (1988) developed linear and power law relations between Young's modulus, porosity and mineral content from simple bending and tension tests. The preceding empirical relations were derived from simple uni-axial test data and were limited to an elastic, isotropic description. Early experiments using ultrasound indicated that bone is transversely isotropic (Lang, 1970; Reilly et al., 1975; Lappi et al.,1979). A more refined use of acoustic microscopy (Van Buskirk et al., 1981; Ashman et al.,1984; Kohles et al., 1997) has indicated that bone (both cortical and trabecular) is an orthotropic material. A comprehensive review of typical values of the elastic constants reported for cortical and trabecular bone may be found, for example, in Cowin (1986). It is further noted that, although the material properties of the solid matrix may be shown to be locally heterogeneous and anisotropic, when a representative sample of bone tissue is viewed as a continuum (Harrigan et al., 1988), the matrix may be considered as isotropic and homogenous (Cowin, 1997). Thus, it has been hypothesised that the anisotropic mechanical properties of bone are governed primarily by the geometric arrangement of the porous micro-structure.

In addition to the description of elastic stiffness properties, there has been a complementary effort in the identification of ultimate strength characteristics of bone. For example, Keller (1994) performed destructive mechanical tests on cortical and trabecular bone specimens to determine the dependency of compressive mechanical properties of bone tissue on several typical measures of bone composition. Using plate-like specimens of femoral cortical bone, Zioupos et al. (1998) correlated flexural strength and other mechanical properties with age. However, the results of these studies are of little use for more advanced, contemporary analyses since the anisotropic nature of bone was not accounted for. Keaveny et al. (1999) developed power law relations between directionally dependent strength characteristics and apparent density for bovine trabecular bone using a transversely isotropic material model. The data were also used to develop and validate a multi-axial failure

criterion, known as the Tsai-Wu criterion, as a function of apparent density. However, the failure criterion was found to be inadequate for predicting the strength of new specimens. Evidently, further research remains to be conducted in order to establish the conditions at failure in trabecular and cortical bone under general stress conditions.

1.3 Fabric Tensor Characterization of Bone Architecture

The anisotropic material properties of bone have been found to depend upon the structural arrangement of its porous micro-structure. A suitable means of characterizing the architecture of bone, and as a result, establishing a relation between mechanical properties and micro-structure, has been the focus of considerable and diversified research effort. Stereology, a branch of mathematical science, has been used to estimate three-dimensional (3D) morphological parameters from two-dimensional (2D) or one-dimensional (1D) geometric entities (Weibel, 1980). Whitehouse (1974) developed stereological measurement techniques for describing the anisotropy of trabecular bone architecture on 2D planar sections. Whitehouse defined the 'mean intercept length' (MIL) at some arbitrarily chosen direction as the relative bone area divided by the total projected boundary perimeter per unit area. When MIL data is plotted as a radius from the origin at the angle of measurement, a curve remarkably close to an ellipse is generated. A departure from isotropy is characterized by the ratio of the ellipse semi-axes. Harrigan and Mann (1984) extended the work of Whitehouse to 3D by taking MIL measurements on three mutually perpendicular planes of cubic bone specimens and introduced a tensor-valued measure of bone architecture called the 'mean intercept length tensor.' Cowin (1985) is credited with developing a constitutive relation between the fourth rank elasticity tensor of a porous, anisotropic linear elastic material (e.g., bone) and a symmetric second rank tensor, known as a 'fabric tensor.' Zysset et al. (1995) developed a more general approach relating even ranked fabric tensors to the

fourth rank elasticity tensor, ensuring invertibility, positive definiteness and appropriate material symmetry for an arbitrary fabric.

With the advent of new stereological procedures (Odgaard et al., 1990; Smit et al., 1998) and 3D imaging techniques such as micro-computed tomography (micro-CT) (Sasov, 1987; Sasov and Van Dyck, 1998) and high resolution magnetic resonance imaging (MRI) (Chung et al., 1995), the material fabric of a representative bone sample may be readily detected. Numerous researchers have attempted to correlate orthotropic or transversely isotropic elastic material constants with fabric data either statistically with material testing data (Turner et al., 1990; Goulet et al., 1994), or by large scale 3D FE analyses (Van Rietbergen et al., 1996; Odgaard et al., 1997). However, there are problems associated with both approaches. With the former, the influence of boundary conditions on the necessarily small size of representative samples may confound test results. With the latter, isotropic elastic constants must be assumed for individual bone elements since an open question yet remains as to what the material properties of individual bone constituents (i.e., trabeculae, osteons) are. Recent developments in mechanical testing procedures by Keaveny et al. (1997) may eradicate some of these problems and make the identification of orthotropic constants more reliable.

There are several issues which remain to be addressed with regard to the use of fabric measures in general. With the exception of Odgaard et al.(1997), few researchers have performed comparative or parametric studies of the various fabric measures and none have rationally justified which measure(s) should be employed when conducting numerical studies of larger bony structures (e.g., femur, tibia etc.). Clearly, a unique approach to calculating fabric data does not exist as is evident from the numerous techniques readily available in the literature. Moreover, measures adopted for numerical analyses of bone should have some physical significance which can be rationally correlated with mechanical properties. Finally,

the influence of neglecting higher order, even ranked tensors in fabric-based constitutive formulations for bone remains to be assessed.

1.4 Finite Element Modelling of Bones

The field of biomechanics encompasses many aspects of physiology, kinesiology, mathematics and engineering and is, therefore, cross-disciplinary by nature. Solutions to problems within this area often involve engineers, medical practitioners, applied physicists, computer scientists, and statisticians. Typical problems which have been explored over the past several decades include stress analysis of bones, bone remodelling/resorption phenomena, bone-prosthesis interactions (loosening), and bone fracture and repair. Evidently, there are considerable difficulties which an analyst encounters when modelling bone and its environment. There is the composite nature of the system, whether it is between a human bone and a metal prosthesis, or within the structural composition of the bone itself. The kinematic and loading conditions to consider are complex and time-dependent in nature. Finally, there is significant variability between individual bones which makes meaningful extrapolation of results to the human population in general very difficult. Clearly, the study of bone mechanics requires specialized numerical and diagnostic techniques. The FE method provides a powerful numerical tool with which to analyse bone behaviour under a wide variety of conditions and has been applied extensively to biomechanical problems. Comprehensive reviews of FE analyses in biomechanics may be found in Husikes et al. (1983), Huiskes et al. (1993), and Gilbertson et al. (1995).

1.4.1 Geometric Modelling of Bones

One of the most significant components of a FE model is the geometric description of the system or object being analysed. Even with the advent of powerful and versatile pre-processor software for generating computer models, the organic and convoluted forms of bones in general create a major stumbling block in the modelling process. Serial reconstruction techniques, until recently, were commonly used to build 3D models of bones (Little et al., 1986; Harrigan et al., 1991; Dalstra et al.,1995). Typically, sequential cross-sections are cut from a sample embedded in hardened resin at a chosen slice thickness. The sections are photographed at a set camera magnification which dictates the in-plane resolution. The images are then digitized and the periosteal and endosteal bone contours are delineated either automatically with a contour extraction algorithm or manually with peripheral digitizing hardware. Finally, the sequence of 2D contours is reconstructed using standard computer aided design (CAD) paradigms into a 3D solid or surface model. In general, the process is time-consuming and destructive, thereby limiting application of this technique to in vitro situations.

Dual-energy X-ray absorptiometry (DEXA) (Mourtada et al., 1996) and CT (Brown et al., 1988; Marom et al., 1990; Nambu et al., 1991; Hobatho et al., 1991; Lotz et al., 1991; Rubin et al., 1993; Mann et al., 1995; Merz et al., 1996; Mann et al., 1997; McNamara et al., 1997; Verdonschot et al., 1997) have been used in conjunction with various image processing and reconstruction algorithms to form 3D bone models. As is evident from the numerous references, CT-based model generation has become extremely popular. This is due, in part, to the availability of the scanning equipment but, more importantly, to the fact that CT offers thin slices of high contrast images in digital form. In addition, several researchers have used CT data to map material properties to elements within their FE models (Marom et al., 1990; Rubin et al., 1993; Verdonschot et al., 1997). This technique is extremely useful in creating

a realistic description of the heterogeneous distribution of material properties within bone structures. For example, Rubin et al. (1993) employed a standard density calibration phantom to establish a relation between CT number and ash density. An experimentally derived relation between apparent and ash density was found to give a final expression for apparent density based on CT number. The stiffness properties of the elements within their femur model were then calculated using a power law relation between apparent density and Young's moduli. A significant advantage of this technique is that given sufficient spatial resolution, models of increased precision may be created. The present author has successfully generated high resolution femur models using a variation of the aforementioned CT techniques (Pietruszczak et al., 1997,1999).

1.4.2 Boundary and Loading Conditions

To ensure some measure of validity, the use of the FE method requires accurate modelling of geometry, boundary and loading conditions and material behaviour. These issues will be discussed here in the context of femoral bone/implant modelling studies. Firstly, numerous studies have assumed lower degrees of elastic symmetry (i.e., isotropy) and material homogeneity (Hampton et al., 1980; Vichnin et al., 1986; Brown et al., 1988; Harrigan et al., 1991a; McNamara et al., 1997). Furthermore, the majority of FE studies involving the femur have reduced its geometric representation to the femoral head and roughly 50% of the diaphysis. The free end of the diaphysis is inevitably given a fixed boundary condition. A sketch of a typical femur model is shown in figure1.1. Saint Venant's principle is generally invoked as the justification for this simplification since the region of interest, the proximal femur, is relatively far from this boundary. It is unclear as to whether modelling the entire femoral shaft with an intact knee is necessary or if this seemingly drastic simplification is, in fact, justified. However, as previously discussed, it has become

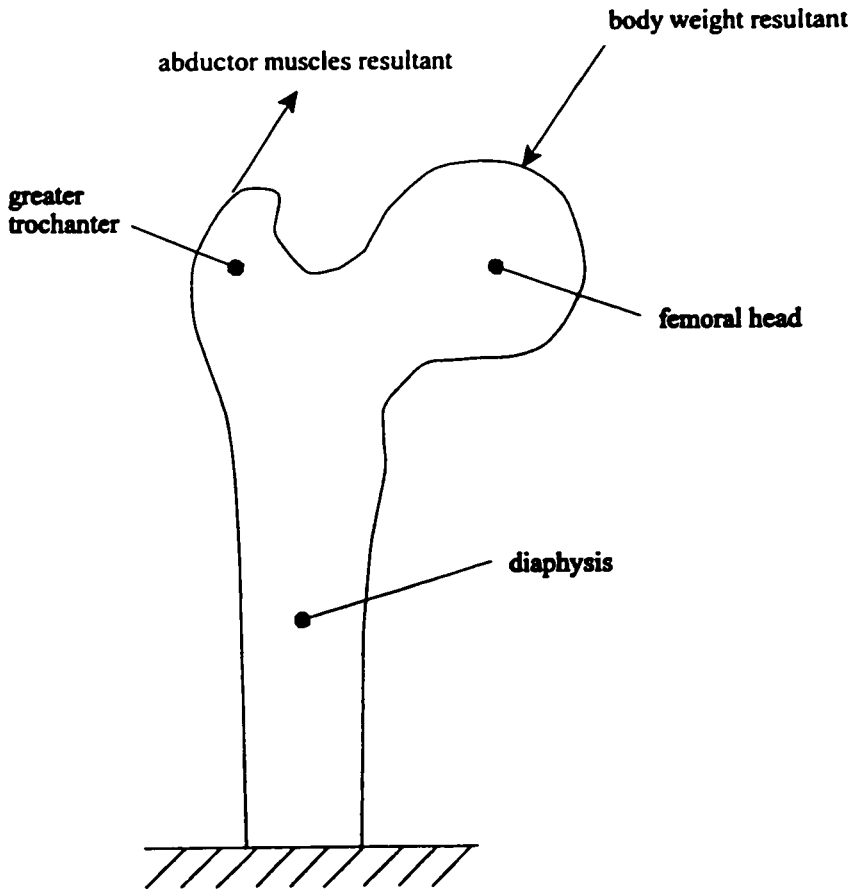

Figure 1.1: Typical boundary and loading conditions on a femur model.

technologically and economically feasible to generate anatomically complete and highly accurate 3D models which incorporate a heterogeneous distribution of orthotropic stiffness properties. Secondly, within a hip implant system, the loading condition typically represented is the one-legged stance phase of the gait cycle. This is generally characterized in terms of an aggregate muscle group acting on the greater trochanter and a body weight resultant applied to the femoral head (see figure 1.1). The traction conditions are usually modelled as resultant point loads (Brown et al., 1988; Merz at al., 1996; Mann et al., 1997) although they are clearly distributed in nature. The distribution of contact areas on the femoral head (Greenwald et al., 1971; Bay et al., 1997) as well as the relative magnitudes

(McLeish et al., 1970; Crowninshield et al.,1978) and insertion areas of the major hip abductors (Clark et al., 1987) are available and should, therefore, be included in numerical studies.

1.4.3 Material Failure in Bone

Over the last decade, a number of 3D FE analyses simulating fracture in the human proximal femur have been carried out (Keyak et al., 1998; Lotz et al., 1991a, 1991b; McNamara et al., 1996; Merz et al., 1996; Taylor et al., 1996). Most of these analyses make use of simple failure criteria which have been developed for a class of isotropic, non-porous materials. In particular, a number of authors have used von Mises criterion (e.g., Lotz et al., 1991a, 1991b; Merz et al., 1996) which was originally developed for metals. In general, assessment of the risk of failure based on these criteria may not be reliable as bone tissue is porous and strongly anisotropic. As previously mentioned, a substantial amount of work has provided evidence of anisotropy in bone, which may be quantified using an orientation distribution function characterized by fabric tensors. In addition, previous studies (Reilly et al., 1975; Burstein et al., 1976; Carter et al, 1978; Torzilli et al., 1981; Stone et al., 1983; Keaveny et al., 1994) have clearly demonstrated that the mechanical behaviour of bone is, in general, inelastic and the strength in tension is considerably lower than in compression. Given this evidence, the specification of the conditions at failure should include both these effects, i.e. the directional dependence of strength characteristics as well as their sensitivity to all three basic stress invariants. A general failure criterion which incorporates a measure of internal bone architecture was proposed by Pietruszczak et al. (1997) and implemented by the present author in a FE study of bone fracture therein. Here, attainment of the proposed criterion is reached in simple tension and signifies a brittle failure mode.

1.5 Objectives of the Research

As indicated in the preceding discussion, there are many avenues of exploration available within the field of numerical modelling of bone behaviour. Previous limitations imposed by the complexity of the problem can now be generally overcome with currently available computer hardware, software, high resolution medical imaging, and improved image processing techniques. Some of these limitations are addressed in the numerical example presented in Pietruszczak et al. (1997): an anatomically accurate 3D geometric model, heterogeneous distribution of fabric-based orthotropic material properties, realistic traction conditions, analysis incorporating directionally dependent failure criteria. The primary focus of the more recent developments is on the identification of tensorial measures of bone architecture and their incorporation within an elastic constitutive framework.

A new and substantial component of the research is the investigation and algorithmic specification of a unified computational approach to identifying and quantifying bone fabric from micro-CT images. The mathematical framework, introduced in chapter 2, is based on the general notion of a scalar valued and orientation dependent 'distribution function' of the kind originally described by Kanatani (1984). A modification to the basic distribution function is incorporated which can account for higher order fluctuations in measurement data while maintaining the desirability of restricted forms of material symmetry. Currently used measures of fabric that are based on lineal intercept quantities are discussed and a new computational technique for obtaining several of these measures is also presented. In addition, a new measure of material fabric based on the concept of 'average pore size' is introduced and formally specified. In chapter 3, a language independent pseudo-code is outlined and then employed in the development of component and aggregate algorithms for the measurement of fabric in micro-CT images. The algorithms are verified in chapter 4 using data sets which describe simple geometric entities, and the performance characteristics

of the different measures are assessed. In chapter 5, a non-linear data fitting scheme is developed in order to quantify the constants appearing in a given distribution function. An approach to visualizing orientation and symmetry information is presented in chapter 6 which was adopted from the field of magnetic resonance imaging. Finally, the performance of the different fabric measures is assessed in the context of two micro-CT images of femoral trabecular bone samples.

A basic methodology for modelling bone related problems has been developed and employed by the present author in two published papers: Pietruszczak et al. (1997) and Pietruszczak et al.(1999). Many aspects of the research presented in these papers are repeated in chapter 7 of this thesis. Specifically, the geometric modelling techniques developed for generation of a high resolution FE model of a femur are described as presented in Pietruszczak et al. (1997), and the mathematical formulation of a constitutive model and failure criterion for bone is repeated from Pietruszczak et al. (1999). Finally, the results of several FE analyses are presented to serve as an illustration of the overall modelling framework. Specifically, the results pertain to the assessment of risk of bone failure due to a fall to the hip in a healthy and a simulated aged femur.

The thesis concludes in chapter 8 with a brief overview of the presented material, the conclusions and some recommendations for future work.

CHAPTER 2 Fabric Tensors

The architecture of a porous material exhibiting an oriented micro-structure, or 'fabric,' can be described by a scalar valued, orientation dependent function. The basic components of the distribution function are the mean value of a specific 'fabric descriptor,' and a sequence of symmetric, traceless tensors describing its directional variation. A theoretical discussion of the formulation of fabric tensors from directional data can be found in Kanatani (1984). The advantage of using tensor equations is that the tensors have simple transformation rules and they can be directly employed in describing orientation dependent properties such as permeability, failure strength, or elastic moduli. In contrast with Kanatani's (1984) general framework, the focus of this chapter is on describing the distribution of data that includes both orientation and weight.

Section 2.1 describes the general form of the distribution function while section 2.2 outlines functional constraints necessary for representing bone architectures. An image-based coordinate frame of reference is defined in section 2.3 in order to facilitate the geometric and mathematical description of the detection procedures. Specific fabric descriptors appearing in the literature, based on lineal intercept measurements, are described in section 2.4 with reference to the adopted functional form. In addition, a new descriptor is presented. Finally, alternative equations for defining several of the more common descriptors appearing in the literature are presented, which were derived based on empirical observation.

2.1 Orientation Distribution Function

The distribution function is defined in such a way as to describe the directional variation of some measurable quantity per unit volume of a region under consideration. The general form is given by:

$$f(\hat{\mathbf{v}}) = C(1 + D_{ij}\hat{v}_i\hat{v}_j + D_{ijkl}\hat{v}_i\hat{v}_j\hat{v}_k\hat{v}_l + \ldots) \tag{2.1}$$

Where D's are symmetric, traceless, even-ranked tensors. Here, $f(\hat{\mathbf{v}})$ is defined over a circumsphere (i.e., the smallest sphere enveloping a volumetric domain) enclosing a representative volume of material, which may be of any simple convex shape (e.g., sphere, cylinder, prism). C represents the mean value of the descriptor, while the second and higher order tensors $D_{ijkl\ldots}$ describe its directional variation or deviation from the mean. The components of the unit vector, $\hat{\mathbf{v}}$, can be defined in terms of the spherical angles θ and φ:

$$\hat{\mathbf{v}}(\theta,\varphi) = [\sin(\theta)\cos(\varphi), \sin(\theta)\sin(\varphi), \cos(\theta)]^T \tag{2.2}$$

θ is the angle of colatitude measured in the positive sense from the x_3-axis. φ is the angle of longitude measured in the positive sense from the x_1-axis in the plane spanned by the x_1 and x_2 axes. Figure 2.1 shows the spatial relations between θ, φ, and $\hat{\mathbf{v}}$.

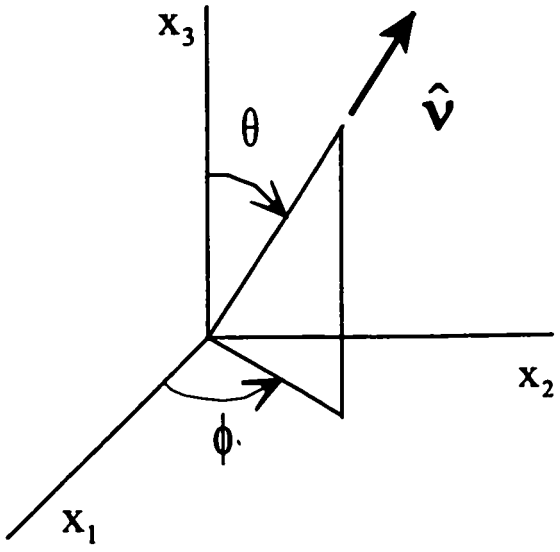

Figure 2.1: Spherical angles θ and φ and sampling direction, $\hat{\mathbf{v}}$.

2.2 Second and Fourth Order Approximations

The second order distribution function, from equation (2.1), is defined as

$$f(\hat{\mathbf{v}}) = C(1 + D_{ij}\hat{v}_i\hat{v}_j); \quad D_{kk} = 0; \quad D_{ij} = D_{ji}; \quad \hat{v}_k\hat{v}_k = 1 \tag{2.3}$$

An alternative to this formulation is

$$f(\hat{\mathbf{v}}) = 3C A_{ij}\hat{v}_i\hat{v}_j; \quad A_{kk} = 1; \quad A_{ij} = A_{ji} \tag{2.4}$$

where A_{ij} is defined as

$$A_{ij} = \frac{1}{3}(\delta_{ij} + D_{ij}) \tag{2.5}$$

For a smooth orthogonal anisotropy, it is sufficient to retain the form of equation (2.3) or equation (2.4). The interpretation is that D_{ij} becomes zero for an isotropic distribution. For non-zero D_{ij}, the eigenvectors, $\hat{\mathbf{e}}_i$, define the symmetry axes while the corresponding eigenvalues, λ_i, are the ratios of the distribution to the isotropic distribution along these axes (Kanatani, 1985), i.e.:

$$f(\hat{\mathbf{e}}_i) = C(1 + \lambda_i) \quad \Rightarrow \quad \frac{f(\hat{\mathbf{e}}_i)}{C} \propto \lambda_i \tag{2.6}$$

In geometric terms, the principal values of D_{ij} define the semi-axes of an ellipsoidal shape. If D_{ij} vanishes, the distribution function, plotted as a radial vector, defines a sphere with radius C.

The fourth order distribution function has the form

$$\begin{aligned} &f(\hat{\mathbf{v}}) = C(1 + D_{ij}\hat{v}_i\hat{v}_j + D_{ijkl}\hat{v}_i\hat{v}_j\hat{v}_k\hat{v}_l) \\ &D_{kk} = 0 \; ; \quad D_{ij} = D_{ji} \; ; \quad \hat{v}_k\hat{v}_k = 1 \\ &D_{ijkl} = D_{jikl} = D_{klij} = D_{lkij} \; ; \quad D_{mmkl} = 0_{kl} \end{aligned} \tag{2.7}$$

The fourth order symmetry conditions reduce the number of independent coefficients from 81 to 15. The traceless condition further reduces the remaining 15 components to 9. In this case, an analogous representation to equation (2.4) does not exist. With a fourth order approximation, higher material symmetries are possible, as noted by Zysset and Curnier (1995).

As previously discussed, bone material exhibits transversely isotropic and, in some instances, orthotropic material symmetry (cf. Cowin, 1981). Therefore, $f(\hat{\mathbf{v}})$ may be approximated by a second order representation. However, in order to attain a higher degree of accuracy in fitting measurement data, equation (2.3) can be extended by incorporating dyadic products of the second order tensor (Pietruszczak and Mroz, 2001). Assuming that $D_{ijkl} = bD_{ij}D_{kl}$, $D_{ijklmn} = dD_{ij}D_{kl}D_{mn}$ etc., the modified n^{th} order form is

$$\begin{aligned} f(\hat{\mathbf{v}}) &= C_0(1 + D_{ij}\hat{v}_i\hat{v}_j + C_1(D_{ij}\hat{v}_i\hat{v}_j)^2 + \ldots + C_{n-1}(D_{ij}\hat{v}_i\hat{v}_j)^n) \\ &= C_0(1 + D_{ij}\hat{v}_i\hat{v}_j + \sum_{i=2}^{n} C_{i-1}(D_{ij}\hat{v}_i\hat{v}_j)^i) \end{aligned} \tag{2.8}$$

The advantages of this equation are that orthotropic symmetry is retained, a simple geometric interpretation is preserved, and the implementation is less complex. Furthermore, one can statistically correlate measurable properties, such as elastic moduli, with the eigenvalues of D_{ij}.

2.3 Image Data and Frame of Reference

In the following sections, numerical procedures for detecting various fabric descriptors are developed which incorporate 3D rather than 2D measurements. Hence, the application of additional stereologic or other statistical methods that rely on correlating limited planar observations (e.g., Kanatani 1985, Odgaard et al., 1990) is unnecessary. This approach was prevalent before the availability of 3D modalities suitable for imaging small bone volumes, such as high resolution MRI (Jara et al., 1993) and micro-CT (Sasov, 1987). Trabecular bone images analyzed in this thesis were obtained using the latter technique.

The source of data for all fabric measurements consists of a stack of 2D images which form a 3D matrix. Images were derived from two sources: artificially constructed binary images of spherical or ellipsoidal inclusions, and binarized micro-CT images of bovine and human trabecular bone samples. Images of the former type were used to verify the detection algorithms, to illustrate computational limitations, and to establish procedural guidelines for obtaining sensible measurements. Images of the latter type were subsequently analyzed with the objectives of identifying structural orientation and establishing the degree of anisotropy in real bone samples.

The discrete elements of a 2D image are pixels (picture elements) having physical dimensions of length and width, location, and value. In a 3D image composed of a stack of 2D images, the term 'pixel' is changed to 'voxel' (volume element) to emphasize the additional dimension of depth. In general, micro-CT voxel dimensions are typically specified in μm. However, in this thesis, the focus is primarily on the detection of eigenvectors and on deriving parameters in terms of ratios of eigenvalues. Hence, specification of physical units other than quantities of voxels is unnecessary. All of the

images analyzed in this thesis were of binary form with isotropic voxel dimensions. Voxels are restricted to the binary values 0 or 1, representing void or solid space.

In order to preserve topological relations between voxel entities and to facilitate the description of the detection algorithms, a right-handed Cartesian coordinate system is defined, as shown in figure 2.2, affixed to an image having dimensions w×h×d (voxels). Analogous with 2D image display conventions, the origin is positioned at the top left-hand corner of the first image plane in the stack of 'd' images, in the geometric center of the first voxel. The centroid coordinates of a voxel are defined by a tuple of positive integer offsets from this origin. Thus, the x_1-axis ranges from 0 to w-1 (left to right in plane), the x_2-axis ranges from 0 to h-1 (top to bottom in plane), and the x_3-axis ranges from 0 to d-1 (top to bottom out of plane). The origin, **o**, is given by $[0, 0, 0]^T$ while the center of the image, **c**, is $[w/2, h/2, d/2]^T$.

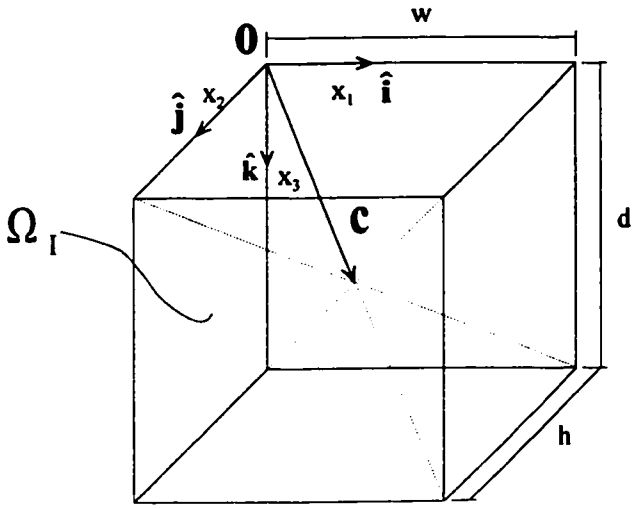

Figure 2.2: Image domain, Ω_I, with dimensions, centroid, and frame of reference fixed at **o**.

2.4 Fabric Descriptors

The science of stereology uses unbiased test probes to estimate structural parameters. Both low and high order dimensional probes, such as points, lines and planes, can be used to measure various quantities of interest, such as their count, length, surface area, and volume. For example, the unbiased test probe for measuring the area fraction of a phase of interest is a regularly spaced point grid. The grid is placed at random over a test area. Then, the grid points that fall within the phase of interest are counted and the ratio of this count to the total number of grid points is computed. This process is repeated for a number of sampling frames. The average ratio is then computed, giving an unbiased estimate of the object area fraction. Lineal probes are suitable candidates for deriving orientation dependent information since they can be counted, have the additional components of direction and length, and are simple to manipulate geometrically. For these reasons, those descriptors which rely on lineal probes have been drawn from the literature for comparison purposes and to illustrate limitations in their measurement.

In general, each fabric descriptor is based on sums and numbers of lineal intercept quantities. The probes are generally equally spaced and are rotated from a standard alignment configuration into a prescribed sampling direction (i.e., $\hat{\mathbf{v}}$). Details of the transformations are provided in chapter 3. Consider the following basic measurement quantities derived from an array of equally spaced, parallel test lines. $L(\hat{\mathbf{v}})$ is the total length of test lines and, depending on the geometry of the sampling domain (e.g., sphere, cylinder, or prism), can be a directionally dependent quantity. An intercept is an isolated line segment arising from the intersection of a test line with the boundary of the phase of interest. The sum of all intercept lengths raised to any power, α, is $\sum I^{\alpha}(\hat{\mathbf{v}})$, while $N(\hat{\mathbf{v}})$ corresponds to their number. All of the subsequent descriptor definitions can be expressed in terms of the three basic components: L, $\sum I^{\alpha}$, and N.

2.4.1 Volume Fraction - *VF*

The volume fraction (VF) of a sample depends on the geometry of the sampling domain and the volume of the phase of interest:

$$VF(\hat{\mathbf{v}}) = \frac{\sum I(\hat{\mathbf{v}})}{L(\hat{\mathbf{v}})} \tag{2.9}$$

In general, although VF is a directionally independent scalar property, a small directional variation will be observed in actual measurements. This variation is due to the approximation of phase boundaries induced by discretization. Therefore, the appropriate estimate of VF is obtained from the mean of a series of directional measurements. The exact value of VF may also be directly calculated as the ratio of the total number of phase of interest voxels to the total number of voxels within the sampling domain.

2.4.2 Mean Intercept Length - *MIL*

Mean intercept length (MIL) was originally introduced in an article by Whitehouse (1974) in which a formula was proposed for calculating the mean widths of trabeculae, as seen in 2D scanning electron microscope micrographs. The measurements were obtained from the relative bone area, A_{Ab}, and the total projected boundary perimeter per unit area, $\mathcal{F}_A$, according to the formula:

$$MIL(\omega) = A_{Ab}/(\tfrac{1}{2}\mathcal{F}_A(\omega)) \tag{2.10}$$

where ω is the angle between an array of test lines and some arbitrarily chosen fiducial direction (Whitehouse, 1974). $\mathcal{F}_A$ is calculated as the number of intersections between phase boundaries. The analogous representation in 3D is given by:

$$MIL(\hat{\mathbf{v}}) = \frac{VF}{\frac{1}{2}\mathcal{F}_v(\hat{\mathbf{v}})} = VF\,\frac{L(\hat{\mathbf{v}})}{N(\hat{\mathbf{v}})} \tag{2.11}$$

where $\mathcal{F}_v$ is the projected surface area per unit volume and VF is the volume fraction of the phase of interest. The factor of one half accounts for the fact that there are two phase interface crossings per intercept.

2.4.3 Mean Free Path - *MFP*

Mean free path (MFP) has been introduced by Underwood (1970) and implemented later by Frost et al. (1998). MFP makes use of intercept information directly and avoids calculation of the volume fraction:

$$MFP(\hat{\mathbf{v}}) = \frac{\sum I(\hat{\mathbf{v}})}{N(\hat{\mathbf{v}})} \tag{2.12}$$

A simple algebraic manipulation demonstrates that MFP gives the same measured quantity as MIL:

$$MIL(\hat{\mathbf{v}}) = VF\,\frac{L(\hat{\mathbf{v}})}{N(\hat{\mathbf{v}})} = \frac{\sum I(\hat{\mathbf{v}})}{L(\hat{\mathbf{v}})}\frac{L(\hat{\mathbf{v}})}{N(\hat{\mathbf{v}})} = MFP(\hat{\mathbf{v}}) \tag{2.13}$$

In this thesis, the simpler definition (2.12) is henceforth considered synonymous with MIL.

2.4.4 Star Length Distribution - *SLD*

Smit et al. (1998) presented a volume-based method for the determination and quantification of anisotropy in porous media. Star length distribution (SLD) essentially

determines the mean object length in a given direction for a typical point within the material. The definition using lineal probes is

$$SLD(\hat{\mathbf{v}}) = \frac{\sum I^2(\hat{\mathbf{v}})}{\sum I(\hat{\mathbf{v}})} \tag{2.14}$$

Here, the intercepts are weighted by their length. The result is that SLD is a more sensitive measurement for the detection of preferred orientations than MIL.

2.4.5 Star Volume Distribution - *SVD*

Star volume distribution (SVD), originally presented by Odgaard et al. (1990), is conceptually similar to that of SLD with the exception that intercepts are weighted more heavily. A point grid method for calculating SVD was later presented by Odgaard et al. (1997). Here, a regularly spaced point grid is generated over the sampling domain. The subset of points that fall within the phase of interest are retained for scanning. For each member of a set of uniformly distributed orientations, a test line is generated at every sampling point and an intersection with the phase of interest is determined. Averaging the cubed intercept lengths over all of the points yields the mean volume as a function of orientation. In this case, the definition of SVD is:

$$SVD(\hat{\mathbf{v}}) = \frac{\pi}{3}\frac{1}{M}\sum_{i=1}^{M} I_i^3(\hat{\mathbf{v}}) \tag{2.15}$$

where M is the number of test points. SLD can also be calculated using this point-based method:

$$SLD(\hat{\mathbf{v}}) = \frac{1}{M}\sum_{i=1}^{M} I_i(\hat{\mathbf{v}}) \tag{2.16}$$

Alternatively, as described by Smit et al. (1998), the definition of SVD using an array of parallel test lines is given by:

$$SVD(\hat{\mathbf{v}}) = \frac{\pi}{3}\frac{\sum I^4(\hat{\mathbf{v}})}{\sum I(\hat{\mathbf{v}})} \tag{2.17}$$

The point grid implementation of SVD and SLD, presented by Odgaard et al. (1997), employs a set of points determined by a randomly translated and rotated cubic grid. Random orientations are equally distributed in the probability field: $[0 \le \varphi < 2\pi; 0 \le \theta < \pi/2]$. The numerical experiments presented in this thesis are based on a stationary cubic grid and a fixed set of non-random orientations applied at each sampling point. As will be demonstrated in the verification sections of chapter four, this approach gives sensible results with relatively few sampling operations.

2.4.6 Areal Pore Size Distribution - *APS*

A new descriptor referred to as areal pore size distribution (APS), was recently introduced by Inglis and Pietruszczak (2001) and is presented here in detail. A spherical sampling domain of radius R is defined so that it encloses a representative volume of porous material. A Cartesian coordinate system is then fixed at the centroid of this sphere. In order to define the 'pore size' distribution, the sphere is cut with a plane of unit normal $\hat{\mathbf{v}}$ and on it is placed a set of uniformly distributed parallel lines aligned in an arbitrary direction, $\hat{\mathbf{u}}$, so that $\hat{\mathbf{u}}$ is orthogonal to $\hat{\mathbf{v}}$. The areal pore size may be defined as

$$\rho_A(\hat{\mathbf{v}}) = \frac{1}{2\pi}\int_{C(\hat{\mathbf{v}})} g(\hat{\mathbf{u}})dC \quad ; \quad g(\hat{\mathbf{u}}) = \frac{\sum I(\hat{\mathbf{u}})}{N(\hat{\mathbf{u}})} \tag{2.18}$$

where dC is the differential angle measured in this plane and $g(\hat{\mathbf{u}})$ is symmetric with respect to the origin; i.e., $g(\hat{\mathbf{u}}) = g(-\hat{\mathbf{u}})$. The mean pore size in the direction $\hat{\mathbf{v}}$ is defined as

$$APS(\hat{\mathbf{v}}) = \frac{1}{2R}\int_{-R}^{R}\rho_A(\hat{\mathbf{v}})dL \tag{2.19}$$

where dL is the differential distance measured along $\hat{\mathbf{v}}$.

Consider now a set of equally spaced, parallel test lines on any one of a set of M equally spaced, parallel planes. The test lines are rotated in-plane k times around a pole defined by $\hat{\mathbf{v}}$. In terms of the discrete quantities I and N:

$$APS(\hat{\mathbf{v}}) = \frac{1}{M}\sum_{j=1}^{M}\rho_{A_j}(\hat{\mathbf{v}}) \quad ; \quad \rho_{A_j}(\hat{\mathbf{v}}) = \sum_{k}\frac{\sum I(\hat{\mathbf{u}}_k)}{N(\hat{\mathbf{u}}_k)} \quad ; \quad \hat{\mathbf{u}}_k\cdot\hat{\mathbf{v}} = 0 \tag{2.20}$$

It is important that the test line density be constant for all M planes. Therefore, in the case of a spherical sampling domain, the test line spacing within each planar disc perpendicular to the sampling direction will be different. The closest spacing between test lines occurs on discs near the poles, whereas the farthest spacing between test lines occurs on the equatorial plane.

2.4.7 Areal Porosity Distribution - *AP*

Areal porosity (AP) is a measure which reflects the local distribution of porosity in the neighbourhood of a point (Pietruszczak, 1999). A unit sphere is defined enclosing a representative volume of material. On the equatorial plane having unit normal $\hat{\mathbf{v}}$, a line passing through the center of the sphere is generated along an arbitrary direction $\hat{\mathbf{u}}$, so that $\hat{\mathbf{u}}$ is orthogonal to $\hat{\mathbf{v}}$. The areal porosity distribution may be defined as

$$AP(\hat{\mathbf{v}}) = \frac{1}{4\pi}\int_{C(\hat{\mathbf{v}})} g(\hat{\mathbf{v}})dC \quad ; \quad g(\hat{\mathbf{v}}) = \sum I(\hat{\mathbf{v}}) \quad ; \quad \hat{\mathbf{v}}\cdot\hat{\mathbf{v}} = 0 \tag{2.21}$$

$C(\hat{\mathbf{v}})$ is a unit circle rounding the center of the sphere, while dC is the in-plane differential angle, and $g(\hat{\mathbf{v}})$ is the total length of interceptions of the test line with the void space.

An AP measurement is constructed in terms of the discrete quantities, I and L with:

$$AP(\hat{\mathbf{v}}) = \frac{1}{M}\sum_{k=1}^{M}\frac{\sum I(\hat{\mathbf{v}}_k)}{L(\hat{\mathbf{v}}_k)} \quad ; \quad \hat{\mathbf{v}}_k\cdot\hat{\mathbf{v}} = 0 \tag{2.22}$$

where L is a set of equally spaced, in-plane parallel test lines and I are the corresponding intercept lengths between the test lines and the phase of interest. It is important to note that the above definitions of APS and AP only apply to a spherical sampling domain.

2.4.8 Alternate Methods for Line Based Descriptors

In addition to the formulae above, alternative equations for defining MIL, SLD, and SVD are presented, which were derived based on empirical observation. In the following definitions, δ represents the test line spacing and N^P is the number of phase of interest voxels within the sampling domain.

If the test lines are spaced one voxel apart, then the following relation holds:

$$\sum I(\hat{\mathbf{v}})|_{\delta=1} = N^P + \varepsilon(\hat{\mathbf{v}}) \tag{2.23}$$

That is, the sum of intercept lengths is the sum of all phase of interest voxels within the sampling domain (i.e., the volume of the phase of interest). The error term, $\varepsilon(\hat{\mathbf{v}})$, accounts for off-axis numerical artifacts which are a result of digitally approximating a smooth,

continuous line with discrete steps. The error vanishes for orientations taken along the x_1, x_2, and x_3 axes of a 3D image (i.e., $\sum I(\hat{\mathbf{k}})|_{\delta=1} = N^P$). For uniformly distributed test lines with $\delta > 1$, the phase of interest volume is approximated by

$$\sum I(\hat{\mathbf{v}})\delta^2 \approx N^P \tag{2.24}$$

The error in the approximation will depend on the sampling orientation, the test line spacing, and the geometries of the sampling domain and of the object being measured.

A similar relation exists between the number of intercepts and the projected area of the phase of interest:

$$N(\hat{\mathbf{v}})\delta^2 \approx A^P(\hat{\mathbf{v}}) \tag{2.25}$$

Again, the projected area, A^P, is a directionally dependent quantity, depending on the structure under investigation and the sampling domain.

Alternate definitions, which incorporate equations (2.24) and (2.25), can now be provided for MIL, SLD, and SVD as follows:

$$MIL(\hat{\mathbf{v}}) \approx \frac{N^P}{N(\hat{\mathbf{v}})\delta^2} \tag{2.26}$$

$$SLD(\hat{\mathbf{v}}) \approx \frac{\delta^2}{N^P}\sum I^2(\hat{\mathbf{v}}) \tag{2.27}$$

$$SVD(\hat{\mathbf{v}}) \approx \frac{\pi}{3}\frac{\delta^2}{N^P}\sum I^4(\hat{\mathbf{v}}) \tag{2.28}$$

Definitions such as those above cannot be formulated in a simple manner for the APS and AP descriptors. This is because in the case of APS, δ varies with position along the sampling axis, while for both descriptors, N^P changes from a 3D quantity to a directionally dependent planar measurement.

CHAPTER 3 Detection Algorithms

The goal of this chapter is to provide a programming language-independent specification of the component and aggregate algorithms used to obtain fabric descriptor measurements. Mathematical and algorithmic details are presented for scanning along arbitrarily oriented lineal probes and for deriving the basic descriptor components: L, $\sum I^a$, and N. The general framework can accommodate sampling domains having a simple convex shape such as a sphere, cylinder or prism. Aggregate algorithms, incorporating either line arrays or point grids, are specified for all of the previously defined descriptors appearing in chapter 2.

Following an introductory description of a pseudo-code and its notation in section 3.1, sampling domain-dependent definitions of point inclusion tests are provided in section 3.2. Component algorithms incorporating these tests are developed in sections 3.3 and 3.4 for building more complex routines. A bisection search routine is developed for accurately locating the points of intersection between test lines and a sampling domain boundary. The routine avoids potentially complex and numerically ill-conditioned solutions to the intersection problem. An important contribution to the development of fabric detection algorithms is presented in section 3.3 wherein an algorithm known as 'pattern matching' is formally developed and described. The algorithm is designed to minimize false intercept counts and thereby improve the accuracy of descriptor measurements. Aggregate algorithms that incorporate the preceding sub-components are described in detail: line array algorithms are described in section 3.3 for measuring the newly proposed APS descriptor as well as for AP, MIL, VF, SLD and SVD, while a point grid algorithm is presented in section 3.4 as an alternative for measuring SLD and SVD. Chapter 3 concludes with an algorithm for obtaining a uniform spatial distribution of sampling directions for application within the measurement algorithms. Measurements obtained with such directions can then be subjected

to a least squares fitting procedure, which generates the coefficients of a specific distribution function. This last topic is discussed further in chapter 5. A summary table of all of the component and master algorithms is provided for convenience in Appendix A.

3.1 Algorithm Notation

In the following sub-sections, symbolic notation is used to differentiate between various geometric domains and their boundaries. The Greek letter Ω signifies a volumetric domain, while Γ signifies a spatial boundary. Subscript arabic letters differentiate between different domain entities. For example, Ω_1 symbolizes the image volume, while Γ_1 refers to the collective set of its planar surfaces.

Algorithms are presented in a programming language-independent pseudo-code, incorporating set and predicate logic notation. The use of set notation eliminates prescribing specific types of storage entities such as arrays, linked lists, stacks, deques etc., which are described in detail in Standish (1995). In the following discussions, a capital arabic letter represents a set of scalar or vector quantities. Set elements are indicated by the same letter, but in lower case. For example, the statement to add a vector element, $\mathbf{x}$, to a set of vectors, X, employs the union operator: $X \leftarrow X \cup \{\mathbf{x}\}$. In pseudo-code, the '$\leftarrow$' notation assigns a left hand variable the result of a right hand expression while reserving the use of '=' for logical equivalency tests (cf. Etter, 1993). The arrow notation, read right to left, can form compound assignment statements such as; $\mathbf{x}_1 \leftarrow \mathbf{x}_2 \leftarrow \mathbf{x}_3 \leftarrow [x, y, z]$. Vector entities are implicitly constructed with comma delimited members between square brackets. Standard vector notation is used along with the usual vector operators: $\cdot, \times, +, -, \| \ \|$. Set entities are initialized by comma delimited members between curly braces: $X \leftarrow X \cup \{\mathbf{x}_1, \mathbf{x}_2\}$ while an

empty set is formally declared with the statement: $X \leftarrow \varnothing$. The number of elements in a set is represented by the letter 'N' with a subscript corresponding to the set name. Thus, the number of vector elements in X is N_X. Subscripts are used as follows: an unbolded lowercase letter with a subscript refers to the component of a vector (e.g., $\mathbf{a} = [2, 1, 3]$; $a_2 = 1$) while a bolded lowercase letter with a subscript identifies a unique member of a vector set (e.g., $\mathbf{x}_3 \in X$; $X = \{\mathbf{x}_1, \mathbf{x}_2, ..., \mathbf{x}_n\}$).

The predicate logic symbols used in this section are; logical negation (i.e., not) '$\neg$'; and '$\wedge$'; or '$\vee$'. The set notation symbols of in '$\in$'; not in '$\notin$'; and subset '$\subset$', are also used as logical statement constructors.

The notation for calling an algorithm within a more complex algorithm is addressed in pseudo-code by formally writing a descriptive algorithm name in italics. Following the name are comma delimited arguments required to execute the algorithm, enclosed in round brackets, similar to the mathematical notation of a function. Return arguments appear to the left of the assignment symbol (e.g., $y \leftarrow \sin(x)$). Algorithm names are defined as they appear in the corresponding figure captions.

3.2 Point Inclusion Tests

Geometric inclusion tests ensure that a correct mapping occurs between the image data and the sampling locations along individual test lines. The specification of a test requires a definition of the spatial domain to which it will be applied. To begin, a sphere may be defined with centroid $\mathbf{c} = [w/2, h/2, d/2]^T$ and radius $R_G \leq \|\mathbf{c}\|$. This sphere, known as the 'global' control volume, Ω_G, is the circumsphere which effectively encloses the sampling

domain, Ω_S. Ω_G is used to define both the test probes (i.e., points or lines) and the sampling orientations. For **c** and R_G as defined, the sampling domain is the entire image volume, i.e. $\Omega_S = \Omega_I$, and the geometric centers of Ω_G and Ω_S are coincident, as shown in figure 3.1.

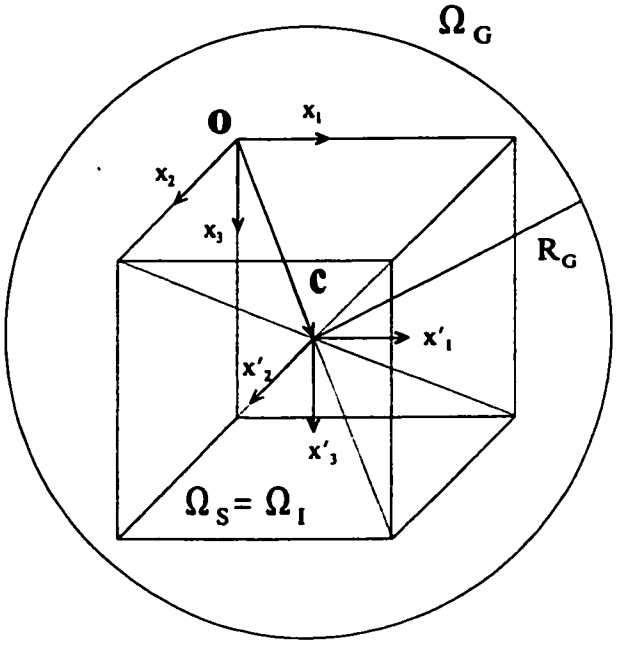

Figure 3.1: Cubic sampling domain, Ω_S, shown coincident with the image domain, Ω_I, surrounded by global control volume, Ω_G.

In figure 3.1, there are two Cartesian frames of reference which will frequently be referred to in this thesis. One is the image frame of reference positioned at the data origin, **o**, and the other is the sampling frame of reference positioned at point **c**. In general, Ω_S is specified in terms of its center, **c**, and one or more dimensional parameters, such as a radius and a height, as in the case of a cylindrical sampling domain. Thus, Ω_S can be positioned anywhere within Ω_I as long as $\Omega_S \subset \Omega_I$. In the following test definitions, R_G is the radius of Ω_G and **c** is the center of both Ω_G and Ω_S with respect to the image reference frame.

The general computational procedure begins with a specification of Ω_S, from which Ω_G is defined. The three types of sampling domains are a sphere, a cylinder, and a prism. A boolean point inclusion test must be specified to determine if a discrete point along a test line is inside or on the surface of Ω_S. The test also provides array bounds checking in the actual code implementation. In pseudo-code, a test is symbolically written as: $\mathbf{p} \in \Omega_S$, asserting whether or not the point $\mathbf{p}$ is on Γ_S or within Ω_S, returning a boolean response. For a spherical domain of radius R and center $\mathbf{c}$, the test is

$$\mathbf{p} \in \Omega_S \quad \rightarrow \quad \|\mathbf{p} - \mathbf{c}\| \leq R \tag{3.1}$$

The point inclusion test for Ω_G is performed in the same manner since the center of Ω_G is also $\mathbf{c}$ and its radius is $R_G = R$. For a cylindrical sampling domain with radius R, and central axis aligned between two points, $\mathbf{a}$ and $\mathbf{b}$, the following intermediate properties are required:

$$\mathbf{h} = \mathbf{b} - \mathbf{a} \quad ; \quad H = \|\mathbf{h}\| \quad ; \quad \hat{\mathbf{h}} = \mathbf{h}/H \tag{3.2a}$$

Then, given a test point, $\mathbf{p}$, and the additional vectors:

$$\mathbf{u}_1 = \mathbf{p} - \mathbf{a} \quad ; \quad \mathbf{u}_2 = (\mathbf{u}_1 \cdot \hat{\mathbf{h}})\hat{\mathbf{h}} \quad ; \quad \mathbf{u}_3 = \mathbf{u}_1 - \mathbf{u}_2 \tag{3.2b}$$

the inclusion test is

$$\mathbf{p} \in \Omega_S \quad \rightarrow \quad 0 \leq \|\mathbf{u}_3\| \leq R \quad \wedge \quad 0 \leq \|\mathbf{u}_2\| \leq H \quad \wedge \quad \mathbf{u}_2 \cdot \hat{\mathbf{h}} > 0 \tag{3.3}$$

Ω_G is defined by $\mathbf{c} = 1/2(\mathbf{a} + \mathbf{b})$ with radius $R_G = \sqrt{R^2 + H^2/4}$. A prismatic domain is defined by two corner vectors $\mathbf{a}$ and $\mathbf{b}$ such that $\mathbf{a}$ is closest to the image origin while $\mathbf{b}$ is farthest from it. The inclusion test is

$$\mathbf{p} \in \Omega_S \quad \rightarrow \quad a_i \leq p_i \leq b_i \quad ; \quad i = \{1, 2, 3\} \tag{3.4}$$

Ω_G is defined by $\mathbf{c} = 1/2(\mathbf{a} + \mathbf{b})$ with radius $R_G = \|\mathbf{c} - \mathbf{a}\|$. In the remaining sections of this chapter, the definitions of Ω_G, Ω_S, R_G, $\mathbf{c}$, and the point inclusion tests are assumed to be globally defined.

3.3 Line Array Algorithms

In this section, component algorithms and transformation equations are presented for detecting intercepts between the phase of interest in a binary 3D image and a set of parallel test line segments, aligned with an arbitrary sampling orientation, $\hat{\mathbf{v}}$. The goal of this section is to define two master algorithms that compute the three basic quantities: $N(\hat{\mathbf{v}})$, $\sum I(\hat{\mathbf{v}})$, and $L(\hat{\mathbf{v}})$, from which various descriptor measurements are calculated. The first master algorithm is based on an isotropic line array definition and generates VF (eq. 2.9), MIL (eq. 2.12), SLD (eq. 2.14), and SVD (eq. 2.17) measurements. The second master algorithm is based on a non-uniform line array specification and provides APS (eq. 2.20) and AP (eq. 2.22) measurements.

The basic procedure in both cases begins with a specification of Ω_S and, hence, Ω_G. Then, a set of points are defined on a hemispherical surface, Γ_G. For each sampling orientation a set of parallel test lines passing through the points in the direction of $\hat{\mathbf{v}}$ are defined. The line segments arising from the intersections of the test lines with Ω_S are scanned in a discrete manner to derive the basic descriptor quantities.

3.3.1 A Uniform Line Array Algorithm

A rectilinear, isotropic grid of points with voxel spacing, δ, is defined over the equatorial plane of Ω_G. The number of grid points along the local sampling frame of reference axes is N_δ such that

$$(N_\delta - 1)\delta < 2R_G \tag{3.5}$$

The strictly less than specification ensures that degenerate test line segments having zero length are not defined. The geometry of the grid is shown in figure 3.2 with $N_\delta = 7$.

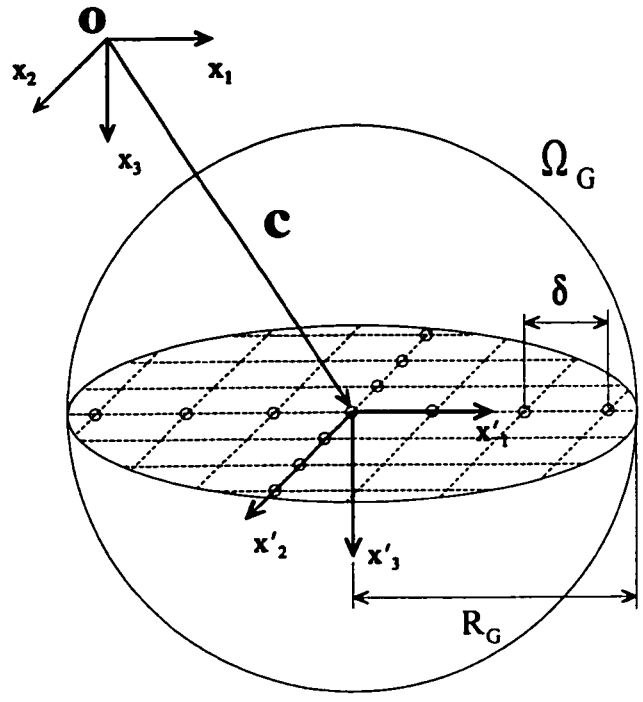

Figure 3.2: Uniform grid spacing defined on the equatorial plane of Ω_G.

N_δ is computed with the algorithm presented in figure 3.3. The algorithm increments along an arbitrary radial direction away from the center of Ω_G in steps of δ until its boundary is crossed. The step counter, N_δ, is then adjusted to reflect the total number of discrete positions along one of the axes of Ω_G.

```
N_δ ← 0
d ← 0;
do
   d ← d + δ;
   N_δ ← N_δ + 1;
while(d < R_G)
N_δ ← 2N_δ - 1;
```

Figure 3.3: Grid sizing algorithm; $N_\delta \leftarrow$ *GetGridSize*(δ).

Having established N_δ, a point set, X, is generated from those grid points which project onto the northern hemisphere of Ω_G according to the algorithm in figure 3.4.

```
X ← ∅;
x'_1^0 ← -δ/2(N_δ + 1);
x'_2^0 ← -δ/2(N_δ + 1);
for(i = 1,2,...,N_δ)do
   for(j = 1,2,...,N_δ)do
      x ← [x'_1^0 + iδ, x'_2^0 + jδ, 0];
      r ← R_G^2 - x·x;
      if(r > 0)then
         X ← X ∪ {[x_1, x_2, -√r]};
      end if
   end do
end do
```

Figure 3.4: Projected grid points algorithm; $X \leftarrow$ *GetUniformLineArray*(δ, N_δ).

At this stage, the vector elements of X define the origins of a set of parallel test line segments, having direction $\hat{\mathbf{k}}$. For an arbitrary orientation of test lines, $\hat{\mathbf{v}}$, the local frame of reference is transformed so that the x'_3-axis coincides with the direction $\hat{\mathbf{v}}$. In this case, the position vectors, $\mathbf{p}^0{}_i$, locating the grid points on the northern hemisphere relative to **o**, are evaluated as:

$$\mathbf{p}^0{}_i = \mathbf{A}\mathbf{x}_i + \mathbf{c} \tag{3.6}$$

where the column vectors of the transformation matrix, **A**, are defined from the spherical angles θ and φ:

$$\begin{aligned} \mathbf{A}(\theta,\varphi) &= [\hat{\boldsymbol{\eta}} \quad \hat{\boldsymbol{\mu}} \quad \hat{\mathbf{v}}] \\ \hat{\boldsymbol{\eta}} &= [\cos(\theta)\cos(\varphi), \cos(\theta)\sin(\varphi), -\sin(\theta)]^T \\ \hat{\boldsymbol{\mu}} &= [-\sin(\varphi), \cos(\varphi), 0]^T \\ \hat{\mathbf{v}} &= [\sin(\theta)\cos(\varphi), \sin(\theta)\sin(\varphi), \cos(\theta)]^T \end{aligned} \tag{3.7}$$

The sampling direction may be recovered from **A** with $\hat{\mathbf{v}} = \mathbf{A}\hat{\mathbf{k}}$. To increment voxel by voxel along a test line, a normalized vector, **v**, is generated from $\hat{\mathbf{v}}$:

$$\mathbf{v}(\hat{\mathbf{v}}) = \hat{\mathbf{v}}/v^* \quad ; \quad v^* = \max(\{|\hat{\mathbf{v}}\cdot\hat{\mathbf{i}}|, |\hat{\mathbf{v}}\cdot\hat{\mathbf{j}}|, |\hat{\mathbf{v}}\cdot\hat{\mathbf{k}}|\}) \tag{3.8}$$

The i^{th} voxel location from the beginning of the k^{th} test line segment in the image frame of reference is obtained parametrically with

$$\mathbf{p}_i = \mathbf{p}^0{}_k + i\mathbf{v} \quad ; \quad \mathbf{p}_i \in \Omega_G \quad ; \quad i \in \mathbb{I} \tag{3.9}$$

Voxel coordinates are derived by rounding the components of $\mathbf{p}_i$ to integer values.

For certain sampling orientations, some test lines will fail to intersect with Ω_S, depending on its geometry (e.g., cubic or cylindrical domain). Therefore, a reduced set of

starting points, P, is generated by transforming the members of X via equation (3.6) and then incrementing along the test lines while checking for intersections with Ω_S, as described in figure 3.5.

```
P ← ∅;
for (i = 1, 2, ..., N_X) do
   p ← Ax_i + c;
   while(p ∉ Ω_G) p ← p + v;
   while(p ∈ Ω_G ∧ p ∉ Ω_S) p ← p + v;
   if(p ∈ Ω_G ∧ p ∈ Ω_S) then
      P ← P ∪ {p};
   end if
end do
```

Figure 3.5: Algorithm for refining a set of transformed grid points;
P ← *GetProjectedLineArray*(X, A, v).

A frequently required task in all of the master algorithms described in this chapter, is to accurately locate the intersection between test line segments and the boundary of the sampling domain. A bisection search method was developed which avoids the use of analytical solutions for determining intersection points between the test lines and Γ_S. Given a pair of points on a test line, $\mathbf{p}_1$ and $\mathbf{p}_2$, which straddle the boundary and a tolerance parameter, the bisection search algorithm in figure 3.6 efficiently locates the intersection point, **t**. Within the algorithm, two temporary vectors, **a** and **b**, are repeatedly updated so that **a** is outside of Γ_S and **b** is inside of Γ_S. The number of steps is controlled by a scaling parameter; δ_b (e.g., $\delta_b = 10^{-10}$). By setting $\delta_b = \|\mathbf{v}\|^{-1}$, the return vector is calculated as the midpoint between $\mathbf{p}_1$ and $\mathbf{p}_2$.

```
t ← a ← p_1;
b ← p_2;
d ← b − a;
δ ← δ_b ‖d‖;
do
   t ← a + d/2;
   if(t ∈ Ω_S) then
      b ← t;
   else
      a ← t;
   end if
   d ← b − a;
while(‖d‖ > δ)
```

Figure 3.6: Bisection search algorithm for locating a test line intersection with Γ_S; $\mathbf{t} \leftarrow$ *GetBoundaryPoint*$(\mathbf{p}_1, \mathbf{p}_2, \delta_b)$.

The set of beginning and end points of test line segments, T, is formed from the set of test line origins, P, according to the algorithm in figure 3.7. Point pairs comprising T are located with the bisection search algorithm. Within the main loop, a point one increment before the current $\mathbf{p}_i$ is located outside Γ_S. Then, the first intercept of the test line segment with the boundary, $\mathbf{t}_1$, is located with the bisection search algorithm, as illustrated schematically in figure 3.8. Here, the points are shown as discrete locations along a test line, while the nearest voxels and their centroids are indicated by an outlined box and a pair of crossing dashed lines. Finally, the terminus of the line segment, $\mathbf{t}_2$, is located by projecting to the nearest discrete location at the far boundary interface and then obtaining the precise position by bisection.

```
T ← ∅;
for (i = 1, 2, ..., N_p) do
    p ← p_i − v;
    t_1 ← GetBoundaryPoint(p, p_i, δ_b);
    t_2 ← p_i;
    while(t_2 ∈ Ω_S) t_2 ← t_2 + v;
    p ← t_2 − v;
    t_2 ← GetBoundaryPoint(t_2, p, δ_b);
    T ← T ∪ {t_1, t_2};
end do
```

Figure 3.7: Algorithm to locate test line end points on Γ_S;
$T \leftarrow$ *GetTestLineSegments*$(P, \mathbf{v}, \delta_b)$.

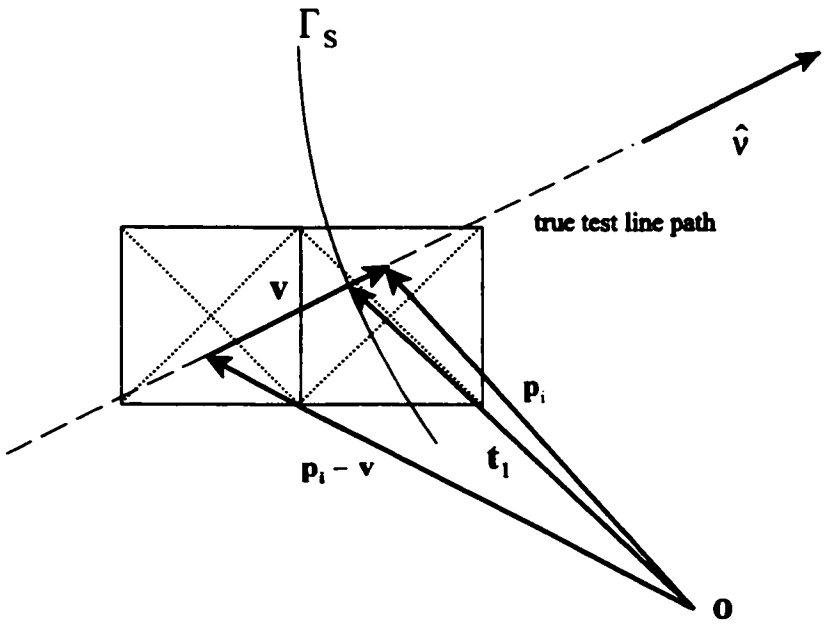

Figure 3.8: Location of a test line intersection, t_1, with Γ_S via the bisection algorithm.

To account for discretization artifacts, examples of which can be found in Kuo and Carter (1991), a two stage heuristic procedure is presented. The first stage is to generate a set of voxels lying along a line segment initiated by a member of the point set P. The second stage of the procedure consists of a pattern matching algorithm that discards isolated voxels and joins aggregate voxel patterns for subsequently determining intercept length quantities.

Recall that a voxel has in addition to its Cartesian coordinates, a binary value that classifies its membership in terms of the phase of interest, or sample 'color,' represented henceforth by C_S. For illustration purposes, let C_S have the binary value 1, and let the conjugate phase have the value 0 (i.e., $\neg C_S$). Then the set of unique voxels through which a test line segment passes, Q, corresponds to a set of four element quantities comprised of three integer coordinates: x, y, and z, defined relative to the image frame of reference, and a binary classification value: either C_S or $\neg C_S$. Four additional voxels along the test line are added to set Q: two at the beginning and two at the end, and contain the conjugate color. The motivation for this step is described further in the description of the pattern matching algorithm.

The basic line scanning algorithm in figure 3.9 consists of incrementing away from an initial point **p**, along a given sampling direction while appending set Q with discrete voxels and their associated phase values until Γ_S is crossed. The operator; <·>, returns the phase value at a discrete location within Ω_I by rounding the components of a given vector argument to the nearest integer tuple. A 2D schematic of the discrete test line, Q, is shown in figure 3.10 along with the image frame of reference, a spherical sampling domain boundary, and the starting location, **p**. Here, point **p** is shown positioned at the centroid of a voxel, rather than on the true test line path, for illustrative purposes. Phase of interest regions having voxels identified by a phase value of C_S are shown in grey.

```
Q ← ∅;
q ← p;
q_1 ← [q - 2v, ¬C_S];
q_2 ← [q - v, ¬C_S];
Q ← Q ∪ {q_1, q_2};
k ← 3;
do
   q_k ← [q, Ω_1<q>];
   Q ← Q ∪ {q_k};
   q ← q + v;
   k ← k + 1;
while(q ∈ Ω_S)
q_{k+1} ← [q, ¬C_S];
q_{k+2} ← [q + v, ¬C_S];
Q ← Q ∪ {q_{k+1}, q_{k+2}};
```

Figure 3.9: Single line pattern filling algorithm; $Q \leftarrow$ *GetLinePattern*$(\mathbf{p}, \mathbf{v}, C_S)$.

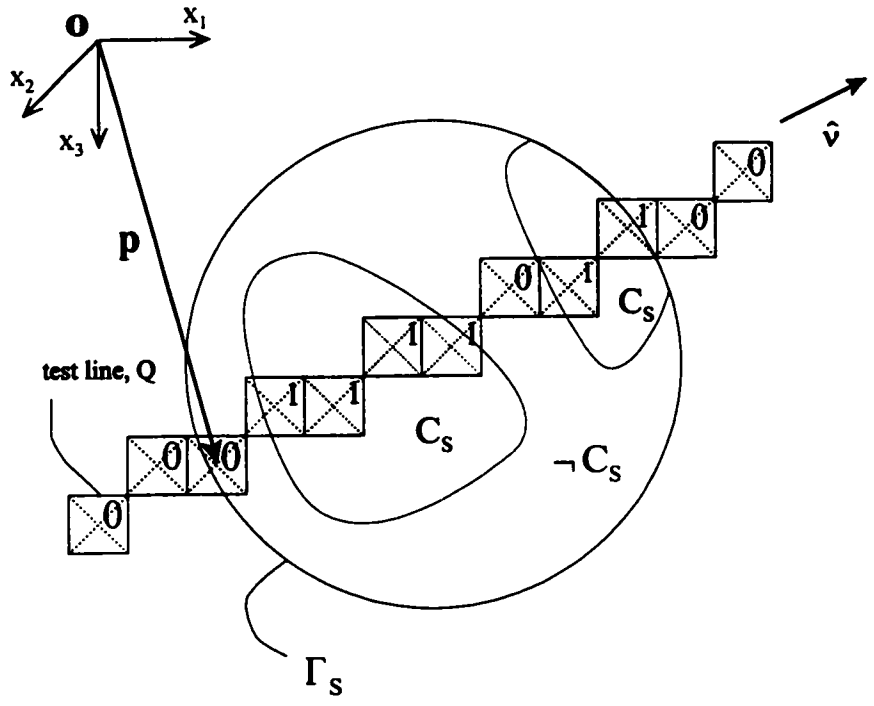

Figure 3.10: Example of a digitized test line, Q, passing through two phase of interest regions.

Set Q, representing the current scan line, is processed by a pattern matching algorithm to extract a set of intercept lengths, I. The goal of the algorithm is to remove intercepts corresponding to intersections with spurs or isolated voxels, and to correct false intercept counts introduced by discretization artifacts. The algorithm in figure 3.11 begins with the specification of a starting and an ending binary color pattern. The beginning of an intercept is identified as a match with the binary pattern; {0,0,1} while its end corresponds to a match with the pattern; {1,0,0}. Thus, the pattern {0,0,1,0,0} signifies a spur or an isolated voxel while a pattern of {0,0,1,1,1,0,0}, for example, is an intercept pattern comprised of three contiguous voxels. The additional two leading and two trailing conjugate colored voxels of set Q simplify the specification of logic handling for cases wherein an intercept is initiated or terminated at the boundary of the sampling domain. The algorithm proceeds by shifting a three element kernel along set Q, until a match with the 'start' pattern is found. A logical state variable is flagged and an index into Q is recorded. The kernel is again shifted until either a 'finish' pattern is found or the kernel has reached the end of set Q. The Cartesian coordinates and sampling color of a voxel are recovered from a given vector element of Q as a product with the matrix operators; ξ and ζ respectively, defined as

$$\xi = \begin{bmatrix} 1 & 0 & 0 & 0 \\ 0 & 1 & 0 & 0 \\ 0 & 0 & 1 & 0 \end{bmatrix} \quad ; \quad \zeta = [\,0\ 0\ 0\ 1\,] \tag{3.10}$$

Within the algorithm, ζ is used to build the comparison kernel while ξ extracts voxel coordinates, when necessary, for determining intercept lengths. The vector origin of an intercept, **a**, is identified as either the intersection of the test line segment with Γ_S (i.e., $\mathbf{t}_1$), or as the midpoint estimate of the phase of interest boundary. The terminus of an intercept, **b**, is found in a similar fashion. An intercept length is calculated as the length of the vector from **a** to **b**, along the sampling direction, $\hat{\mathbf{v}}$.

```
I ← ∅;
start ← {¬C_S, ¬C_S, C_S};
finish ← {C_S, ¬C_S, ¬C_S};
j ← 1;
started ← false;
for(k = 1,2,...,N_Q - 2)do
   pattern ← {ζq_k, ζq_k+1, ζq_k+2};
   if((pattern = start) ∧ ¬started)then
      started ← true;
      j ← k + 1;
   else if((pattern = finish) ∧ started)
      started ← false;
      if(k > j)then
         if(j = 2)then
            a ← t_1;
         else
            a ← 1/2(ξq_j + ξq_j+1);
         end if
         if(k = (N_Q - 2))then
            b ← t_2;
         else
            b ← 1/2(ξq_k + ξq_k+1);
         end if
         I ← I ∪ {(b - a)·v̂};
      end if
   end if
end do
```

Figure 3.11: Intercept detection algorithm incorporating pattern matching; $I \leftarrow$ *GetInterceptLengths*$(Q, \mathbf{t}_1, \mathbf{t}_2, \hat{\mathbf{v}}, C_S)$.

Figure 3.12 shows an instance wherein an intercept is terminated at Γ_S. Within Ω_S, the midpoint between two voxels, identified in the figure as point **a**, provides the estimated intersection point of a test line with the phase of interest boundary, since its precise location is not known. Note that the qualifying intercept pattern in this example is {0,0,1,1,0,0}. Figure 3.13 shows an example of an intercept calculated from two midpoint locations; **a**, **b**.

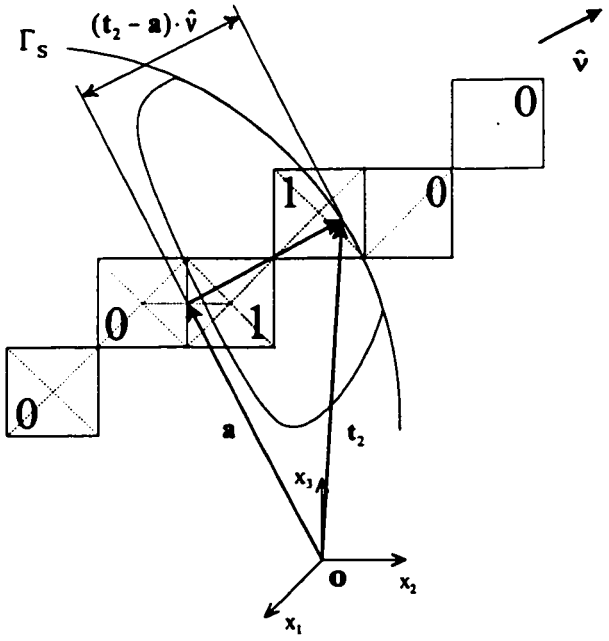

Figure 3.12: Example of an intercept that terminates at the boundary; Γ_S.

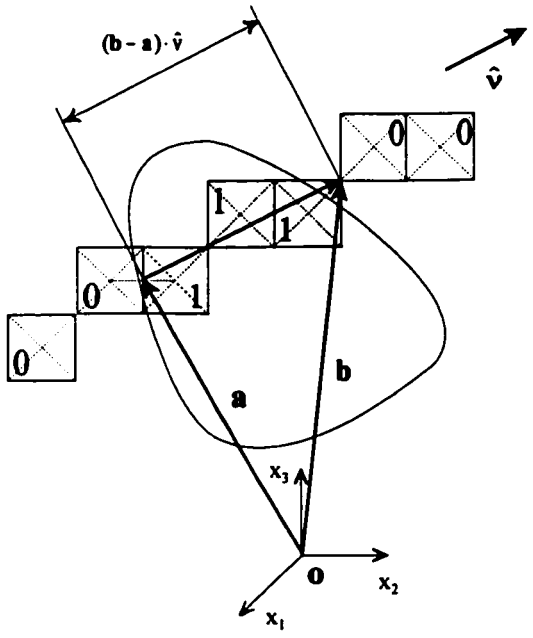

Figure 3.13: Example of an intercept within Ω_S defined using mid-point locations.

From the preceding set building algorithms, more complex procedures are generated for deriving the various fabric descriptors. For example, the descriptor component, $L(\hat{v})$, can be found using the sample algorithm shown in figure 3.14.

```
L ← 0;
for(i = 1, 2, ..., N_T/2) do
   L ← L + (t_2i - t_2i-1)·v̂;
end do
```

Figure 3.14: Sample algorithm for finding the sum of test line lengths;
$L \leftarrow$ *GetLengthOfTestLines*$(T, \hat{v})$.

A voxel counting algorithm, shown in figure 3.15, extracts the number of phase of interest voxels, N^P, as well as the total number of sampling domain voxels, N^T. The algorithm simply loops over the image data indices, checks for geometric inclusion within the sampling domain and then performs a phase membership classification according to the given voxel comparison value, C_S.

```
N^T ← N^P ← 0;
for(k = 0, 1, ..., d - 1)do
   for(j = 0, 1, ..., h - 1)do
      for(i = 0, 1, ..., w - 1)do
         x ← [i, j, k];
         if(x ∈ Ω_S)then
            N^T ← N^T + 1;
            if(Ω_I<x> = C_S)then
               N^P ← N^P + 1;
            end if
         end if
      end do
   end do
end do
```

Figure 3.15: A voxel counting algorithm; $\{N^T, N^P\} \leftarrow$ *GetVoxelCounts*(C_S).

The ratio of N^P to N^T provides a direct VF measurement. It will be demonstrated in chapter 4 that VF defined in this manner is important for the selection of grid spacing, δ, and for algorithm verification purposes.

The master algorithm for determining VF from test line segments, and for building the measurement sets; MIL, SLD, SVD, from an arbitrary set of orientations; Θ and Φ, is presented in figure 3.16. The transformation matrix, **A**, and the incremental vector, **v**, are defined as in equations (3.7) and (3.8), respectively. For each sampling orientation, test line origins are redefined relative to the image frame of reference and projected one voxel inside of Ω_S. Test line end points are then located on the boundary with the bisection search algorithm. Each line segment is scanned and from it a set of intercept lengths; I, are generated. The sum of intercept lengths is compared against the current test line length and set I is adjusted accordingly. Sums of powers of intercept lengths are calculated and added to the grand totals; s_i. After all test lines have been processed, descriptor measurements are constructed from s_i and archived for post-processing.

$N_\delta \leftarrow$ *GetGridSize*(δ);
$X \leftarrow$ *GetUniformLineArray*(δ, N_δ);
$VF \leftarrow MIL \leftarrow SLD \leftarrow SVD \leftarrow \varnothing$;
for$(i = 1, 2, \ldots, N_\Theta)$**do**
  $\mathbf{A} \leftarrow \mathbf{A}(\theta_i, \varphi_i)$;
  $\hat{\mathbf{v}} \leftarrow \mathbf{A}\hat{\mathbf{k}}$;
  $\mathbf{v} \leftarrow \hat{\mathbf{v}}/\max(\{|\hat{\mathbf{v}}\cdot\hat{\mathbf{i}}|, |\hat{\mathbf{v}}\cdot\hat{\mathbf{j}}|, |\hat{\mathbf{v}}\cdot\hat{\mathbf{k}}|\})$;
  $P \leftarrow$ *GetProjectedLineArray*$(X, \mathbf{A}, \mathbf{v})$;
  $T \leftarrow$ *GetTestLineSegments*$(P, \mathbf{v}, \delta_b)$;
  $s_5 \leftarrow s_4 \leftarrow s_3 \leftarrow s_2 \leftarrow s_1 \leftarrow 0$;
  for$(j = 1, 2, \ldots, N_P)$**do**
    $Q \leftarrow$ *GetLinePattern*$(\mathbf{p}_j, \mathbf{v}, C_S)$;
    $I \leftarrow$ *GetInterceptLengths*$(Q, \mathbf{t}_{2j-1}, \mathbf{t}_{2j}, \hat{\mathbf{v}}, C_S)$;
    $dL \leftarrow (\mathbf{t}_{2j} - \mathbf{t}_{2j-1})\cdot\hat{\mathbf{v}}$;
    if$(\sum I > dL)$**then**
      $I \leftarrow \varnothing \cup \{dL\}$;
    end if
    $s_1 \leftarrow s_1 + \sum I$;
    $s_2 \leftarrow s_2 + \sum I^2$;
    $s_3 \leftarrow s_3 + \sum I^4$;
    $s_4 \leftarrow s_4 + N_I$;
    $s_5 \leftarrow s_5 + dL$;
  end do
  $MIL \leftarrow MIL \cup \{s_1/s_4\}$;
  $SLD \leftarrow SLD \cup \{s_2/s_1\}$;
  $SVD \leftarrow SVD \cup \{\frac{\pi}{3}s_3/s_1\}$;
  $VF \leftarrow VF \cup \{s_1/s_5\}$;
end do
$VF \leftarrow \varnothing \cup \{\sum VF/N_{VF}\}$;

Figure 3.16: Algorithm for determining VF, MIL, SLD, and SVD measurements; $\{VF, MIL, SLD, SVD\} \leftarrow$ *ScanUniformLineArray*$(\Theta, \Phi, \delta, \delta_b, C_S)$.

3.3.2 A Non-Uniform Line Array Algorithm

Some modifications must be made to the general framework of the algorithm in figure 3.16 in order to attain uniform in-plane line densities for obtaining APS measurements. The algorithm presented in figure 3.17 maintains the same number of test lines, N_δ, appearing on the equatorial plane of Ω_G for all other planes separated by a distance δ along the x'_2-axis. Thus, the line spacing in any plane perpendicular to the x'_2-axis decreases with increasing distance from the center of Ω_G. Since an APS measurement is based on an average of in-plane measurements, the set of projected test line origins must be generated and stored in individual sets on a plane by plane basis. Thus, X now signifies a vector of sets with elements addressed in superscript notation (i.e., $X^{(j)} \subset X$).

```
X ← ∅;
x'_2^0 ← -δ/2(N_δ + 1);
for(j = 1,2,...,N_δ)do
   X^(j) ← ∅;
   x'_2 ← x'_2^0 + jδ;
   d ← 2√(R_G^2 - (x'_2)^2);
   δ̄ ← max(round(d/N_δ), 1);
   x'_1^0 ← -δ̄/2(N_δ + 1);
   for(i = 1,2,...,N_δ)do
      x ← [x'_1^0 + iδ̄, x'_2, 0];
      r ← R_G^2 - x·x;
      if(r > 0)then
         X^(j) ← X^(j) ∪ {[x_1, x_2, -√r]};
      end if
   end do
   X ← X ∪ {X^(j)};
end do
```

Figure 3.17: Non-uniform projected grid points algorithm;
$X \leftarrow$ *GetNonUniformLineArray*(δ, N_δ).

An APS measurement set is constructed via the master algorithm shown in figure 3.18. Test lines in the direction $\hat{\mathbf{u}}$, equation (2.18), are generated by introducing a transformation matrix, **B**, defined as:

$$\begin{aligned} \mathbf{B} &= [\hat{\zeta} \;\; \hat{\mathbf{v}} \;\; \hat{\mathbf{u}}] \\ \hat{\zeta} &= \mathbf{A}\,[\cos(\psi_k), \sin(\psi_k), 0]^T = \hat{\mathbf{v}} \times \hat{\mathbf{u}} \\ \hat{\mathbf{u}} &= \mathbf{A}\,[-\sin(\psi_k), \cos(\psi_k), 0]^T \end{aligned} \tag{3.11}$$

where ψ_k is the k^{th} in-plane rotation angle around a pole directed along the sampling direction, $\hat{\mathbf{v}}$. The number of in-plane rotations is specified (e.g., $N_\psi = 9, 18, 36$ etc.) so that

$$\psi_k = (k-1)\frac{\pi}{N_\psi} \quad ; \quad k = 1, 2, \ldots, N_\psi \tag{3.12}$$

The transformation of the test line origins follows equation (3.6) with the exception that **A** is replaced with **B**. The APS measurements are similar to MIL with the exception that mean values are stored plane by plane and then subsequently averaged along the main sampling direction.

Although an AP measurement can be obtained with the algorithm in figure 3.18 by adding a few additional constructs, for clarity, a dedicated algorithm is provided in figure 3.19. Again, the AP measurement corresponds to the mean sum of intercept lengths divided by the sum of test line lengths taken in the equatorial plane; i.e., equation (2.22) with $M = N_\psi$. The set of test line origins lying on the equator of Ω_S corresponds to the middle line array set of X.

```
N_δ ← GetGridSize(δ);
X ← GetNonUniformLineArray(δ, N_δ);
APS ← ∅;
for(i = 1,2,...,N_Θ)do
   A ← A(θ_i, φ_i);
   v̂ ← Ak̂;
   S ← ∅;
   for(k = 1,2,...,N_X)do
      s ← 0;
      for(j = 1,2,...,N_ψ)do
         ψ ← (j - 1)π/N_ψ;
         ξ̂ ← A[cos(ψ), sin(ψ), 0]^T;
         û ← ξ̂ × v̂;
         B ← [ξ̂ v̂ û];
         v ← û/max({|û·î|, |û·ĵ|, |û·k̂|});
         P ← GetProjectedLineArray(X^(k), B, v, c);
         T ← GetTestLineSegments(P, v, δ_b);
         for(m = 1,2,...,N_P)do
            Q ← GetLinePattern(p_m, v, C_S);
            I ← GetInterceptLengths(Q, t_2m-1, t_2m, û, C_S);
            dL ← (t_2m - t_2m-1)·û;
            if(∑I > dL)then
               I ← ∅ ∪ {dL};
            end if
            if(N_I > 0)then
               s ← s + ∑I/N_I;
            end if
         end do
      end do
      if(s > 0)then
         S ← S ∪ {s/N_ψ};
      end if
   end do
   APS ← APS ∪ {∑S/N_S};
end do
```

Figure 3.18: Algorithm for determining APS measurements;
{APS} ← *ScanNonUniformLineArray*$(\Theta, \Phi, N_\psi, \delta, \delta_b, C_S)$.

```
N_δ ← GetGridSize(δ);
X ← GetNonUniformLineArray(δ, N_δ);
AP ← ∅;
k ← (N_X - 1)/2;
for(i = 1,2,...,N_Θ)do
   A ← A(θ_i, φ_i);
   v̂ ← Ak̂;
   s_1 ← 0;
   for(j = 1,2,...,N_ψ)do
      ψ ← (j - 1)π/N_ψ;
      ξ̂ ← A[cos(ψ), sin(ψ), 0]^T;
      υ̂ ← ξ̂ × v̂;
      B ← [ξ̂ v̂ υ̂];
      v ← υ̂/max({|υ̂·î|, |υ̂·ĵ|, |υ̂·k̂|});
      P ← GetProjectedLineArray(X^(k), B, v, c);
      T ← GetTestLineSegments(P, v, δ_b);
      s_3 ← s_2 ← 0;
      for(m = 1,2,...,N_P)do
         Q ← GetLinePattern(p_m, v, C_S);
         I ← GetInterceptLengths(Q, t_2m-1, t_2m, υ̂, C_S);
         dL ← (t_2m - t_2m-1)·υ̂;
         if(∑I > dL)then
            I ← ∅ ∪ {dL};
         end if
         s_2 ← s_2 + ∑I;
         s_3 ← s_3 + dL;
      end do
      s_1 ← s_1 + s_2/s_3;
   end do
   AP ← AP ∪ {s_1/N_ψ};
end do
```

Figure 3.19: Algorithm for determining AP measurements;
{AP} ← *ScanEquatorialLineArray*$(\Theta, \Phi, N_\psi, \delta, \delta_b, C_S)$.

3.4 Point Grid Algorithms

In this section, an algorithm based on point grid sampling is presented for generating SLD and SVD measurements. Here, a 3D isotropic grid of test points, X, is generated such that the members of X satisfy the following criteria:

$$\Omega_I\langle \mathbf{x} \rangle = C_S \quad \wedge \quad \mathbf{x} \in \Omega_S \tag{3.13}$$

The algorithm for building set X is presented in figure 3.20.

```
X ← ∅;
x1^0 ← c1 - δ/2(Nδ + 1);
x2^0 ← c2 - δ/2(Nδ + 1);
x3^0 ← c3 - δ/2(Nδ + 1);
for(i = 1,2,...,Nδ)do
   x1 ← x1^0 + iδ;
   for(j = 1,2,...,Nδ)do
      x2 ← x2^0 + jδ;
      for(k = 1,2,...,Nδ)do
         x ← [x1, x2, x3^0 + kδ];
         if(x ∈ ΩS)then
            if(ΩI<x> = CS)then
               X ← X ∪ {x};
            end if
         end if
      end do
   end do
end do
```

Figure 3.20: Algorithm for generating regularly spaced grid points;
$X \leftarrow \mathit{GetPointGrid}(\delta, N_\delta, C_S)$.

The point grid is defined relative to the image frame of reference. With minor modifications to the algorithm, the points can be defined relative to the center of Ω_G; i.e.,

the sampling frame of reference, so that random sampling methods such as those described by Odgaard et al.(1997) can be implemented. Following such a randomization procedure, candidate points can then be identified for inclusion within the set X via equation (3.13).

Once the grid points are formed and the set of sampling orientations is defined, intercepts are generated in the following manner. The beginning and end points, **a** and **b**, of an intercept passing through a grid point, **x**, are determined by repeated application of the algorithm in figure 3.21. The intercept origin, **a**, is found by incrementing away from **x** in the direction of $-\hat{\mathbf{v}}$ until either the sampling location falls outside of Ω_S or a change in phase occurs. In the former condition, the intercept origin is located with the bisection algorithm in figure 3.6 while in the latter a simple midpoint rule is applied. The terminus of the intercept, **b**, is found similarly with the exception that the sampling direction is reversed. A procedure for identifying false end points, such as the pattern matching algorithm described in section 3.3.1, has not been developed.

```
p ← x;
started ← true;
do
   p ← p + v;
   started ← (Ω_I<p> = C_S);
while(p ∈ Ω_S ∧ started)
if(started)then
   p ← GetBoundaryPoint(p, p - v, δ_b);
else
   p ← p - 1/2v;
end if
```

Figure 3.21: Algorithm for finding the end of an intercept;
$\mathbf{p} \leftarrow$ *GetEndOfIntercept*$(\mathbf{x}, \mathbf{v}, \delta_b, C_S)$.

SLD and SVD measurements are obtained with the master algorithm presented in figure 3.22. For each orientation, the set of intercepts, I, is initialized to the null set and then re-built with intercepts generated at each sampling point. The SVD and SLD measurement sets are then appended with values obtained via equations (2.15) and (2.16) respectively.

$N_\delta \leftarrow$ *GetGridSize*(δ);
$X \leftarrow$ *GetPointGrid*(δ, N_δ);
SLD $\leftarrow$ SVD $\leftarrow \varnothing$;
for$(i = 1, 2, \ldots, N_\Theta)$**do**
  $\mathbf{A} \leftarrow \mathbf{A}(\theta_i, \varphi_i)$;
  $\hat{\mathbf{v}} \leftarrow \mathbf{A} \cdot \hat{\mathbf{k}}$;
  $\mathbf{v} \leftarrow \hat{\mathbf{v}} / \max(\{|\hat{\mathbf{v}} \cdot \hat{\mathbf{i}}|, |\hat{\mathbf{v}} \cdot \hat{\mathbf{j}}|, |\hat{\mathbf{v}} \cdot \hat{\mathbf{k}}|\})$;
  $I \leftarrow \varnothing$;
  for$(j = 1, 2, \ldots, N_X)$**do**
    $\mathbf{a} \leftarrow$ *GetEndOfIntercept*$(\mathbf{x}_j, -\mathbf{v}, \delta_b, C_S)$;
    $\mathbf{b} \leftarrow$ *GetEndOfIntercept*$(\mathbf{x}_j, \mathbf{v}, \delta_b, C_S)$;
    $I \leftarrow I \cup \{(\mathbf{b} - \mathbf{a}) \cdot \hat{\mathbf{v}}\}$;
  end do
  SLD $\leftarrow$ SLD $\cup \{\sum I / N_I\}$;
  SVD $\leftarrow$ SVD $\cup \{\frac{\pi}{3} \sum I^3 / N_I\}$;
end do

Figure 3.22: Algorithm for determining SLD and SVD measurements using a point grid; $\{SLD, SVD\} \leftarrow$ *ScanPointGrid*$(\Theta, \Phi, \delta, \delta_b, C_S)$.

3.5 Sampling Orientations

Since we are interested in the distribution of quantities being measured, or in quantities derived from them, the sampling orientations themselves are of no particular interest and should not influence the results. However, a uniform distribution of sampling directions is

required for obtaining a set of descriptor measurements that will be subjected to application of the least squares procedure discussed in chapter 5. Generating a sequence of uniformly distributed directions in 3D, or points on a unit sphere, is non-trivial and in general, problem specific. The notion of uniformity can be realized, for example, by sampling with a 'large' number of random orientations. However, we desire a computationally efficient and reproducible scheme, as in the manner of certain quadrature formulae, yet without restriction on the number of sample points. Such approaches exist and have been discussed by Saff and Kuijlaars (1997).

In this thesis, a simple, explicit construction scheme known as the 'generalized spiral points method' has been adopted. The method is straightforward to implement and places no restriction on the number of points. The reader is referred to Rakhmanov et al. (1994) for theoretical details. Using the spherical coordinates (θ, φ); $0 \le \theta \le \pi, 0 \le \varphi \le 2\pi$, for N points (Saff and Kuijlaars, 1997):

$$h_k = -1 + 2(k-1)/(N-1), \quad 1 \le k \le N; \quad \theta_k = \cos^{-1}(h_k) \tag{3.14a}$$

$$\varphi_k = \left(\varphi_{k-1} + \frac{C}{\sqrt{N}} \frac{1}{\sqrt{1 - h_k^2}} \right) \bmod(2\pi), \quad 2 \le k \le N-1, \quad \varphi_1 = \varphi_N = 0 \tag{3.14b}$$

where 'mod' is the modulo function. Saff and Kuijlaars (1997) suggest that the optimal theoretical value for C is $(8\pi/\sqrt{3})^{1/2} \approx 3.809$, which was adopted for this study. However, the value of C can be adjusted, depending on the application. A small modification to the preceding specification is incorporated into the algorithm shown in figure 3.23 to account for the fact that the last orientation can be omitted since $f(\hat{\mathbf{v}}) = f(\hat{\mathbf{v}} + \pi)$.

```
α ← (√(8π/√3))/√N;
H ← ∅;
Θ ← ∅;
for(k = 1,2,...,N - 1)do
   h ← -1 + 2(k - 1)/(N - 1);
   Θ ← Θ ∪ {cos⁻¹(h)};
   H ← H ∪ {h};
end do
φ ← 0;
Φ ← Φ ∪ {φ};
for(k = 2,3,...,N_H)do
   φ ← (φ_{k-1} + α/√(1 - h_k²))mod(2π);
   Φ ← Φ ∪ {φ};
end do
```

Figure 3.23: The generalized spiral points algorithm; $\{\Theta, \Phi\} \leftarrow$ *GetSpiralPoints*(N).

The 3D spatial arrangement of 100 spiral points on a sphere (e.g., Ω_G) is presented in figure 3.24. Figure 3.25 shows the spatial uniformity of 100 spiral points in the range $0 \le \theta \le \pi/2$, $0 \le \varphi \le 2\pi$ projected onto the x_1'-x_2' equatorial plane of Ω_G.

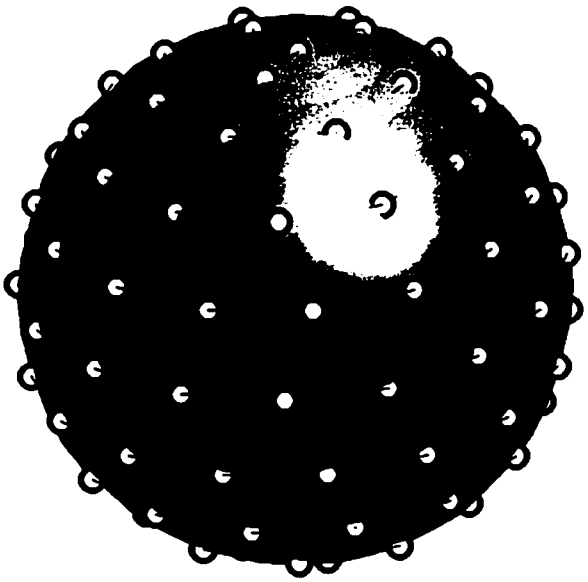

Figure 3.24: 100 spiral points on a sphere.

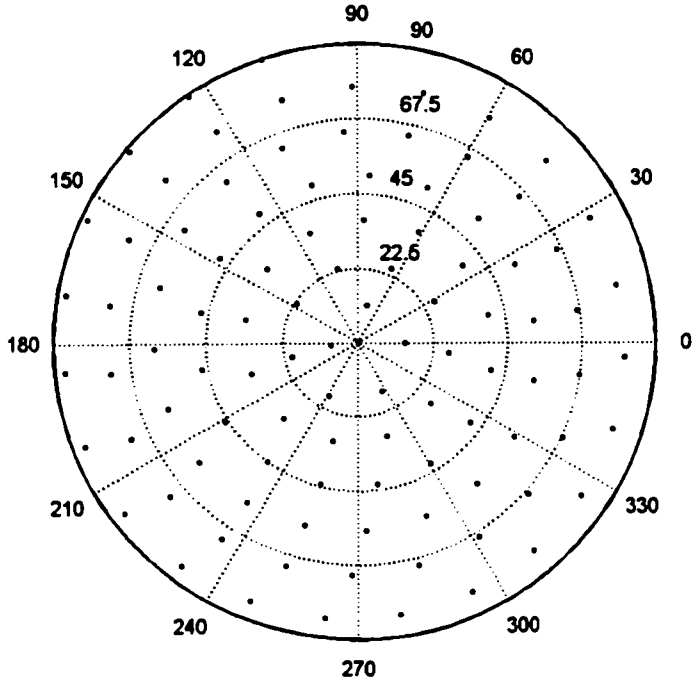

Figure 3.25: 100 spiral points projected onto an equatorial plane.

CHAPTER 4 Algorithm Verification

In section 4.1, exact solutions are developed for the AP, APS, MIL, SLD, and SVD descriptors using two simple geometric entities; the sphere and the ellipsoid. A brief introduction on the use of 3D binary images for the verification tests is presented in section 4.2. The remaining sections of this chapter focus on parametric studies of the algorithms presented in chapter 3. Measurements of a binary image of a spherical inclusion will be compared with exact descriptor values to demonstrate the influence of algorithm parameters on the results. More specifically, section 4.3 demonstrates the accuracy of boundary detection via the bisection algorithm. The efficacy of the pattern matching algorithm is shown in section 4.4 while the influence of grid spacing on both line array and point grid algorithms is outlined in section 4.5. In section 4.6, descriptor measurements of an ellipsoidal inclusion image are used to illustrate and verify the detection of an orientation triad. The chapter concludes with a discussion of algorithm efficiency and some general recommendations on the selection of scanning parameters based on VF measurements.

4.1 Analytical Solutions

In this section, exact solutions for a spherical and an ellipsoidal inclusion geocentric within a larger spherical sampling domain of radius 'R' are presented for each of the fabric descriptors defined in section 2.5. For a spherical inclusion of radius 'r,' no distinction is made with regard to measurement orientation. Directionally dependent solutions are derived for an ellipsoid with semi-axes of lengths a, b, and c along the x, y and z axes, respectively.

Without resorting to integral forms, the volume fraction of a spherical inclusion within a larger spherical sampling domain is simply the ratio of their cubed radii:

$$VF = \frac{4/3\pi r^3}{4/3\pi R^3} = \frac{r^3}{R^3} \tag{4.1}$$

while for an ellipsoidal inclusion within the spherical sampling domain there is

$$VF = \frac{4/3\pi abc}{4/3\pi R^3} = \frac{abc}{R^3} \tag{4.2}$$

To define the areal porosity AP, one may consider an arbitrary plane passing through the origin of the spherical sampling domain. The intersection of the plane with the sampling domain is a disc with radius R. Similarly, the intersection of the plane with the spherical void is a disc with radius r. Therefore, AP for a spherical inclusion is simply

$$AP = \frac{\pi r^2}{\pi R^2} = \frac{r^2}{R^2} \tag{4.3}$$

For an ellipsoid, there are three orientation dependent values:

$$AP(\hat{\mathbf{i}}) = \frac{bc}{R^2} \quad ; \quad AP(\hat{\mathbf{j}}) = \frac{ac}{R^2} \quad ; \quad AP(\hat{\mathbf{k}}) = \frac{ab}{R^2} \tag{4.4}$$

The closed-form solution for a general off-axis orientation involves a complex integral equation which must be evaluated by numerical means and will not be developed further.

With reference to figure 4.1, the intersection of a test line passing through 'A' and directed along the z-axis with a spherical domain produces an intercept of length 2z. The projected area of the sphere is πr^2. This result is proportional to the number of intersections obtained in the limiting case when the test line spacing approaches zero.

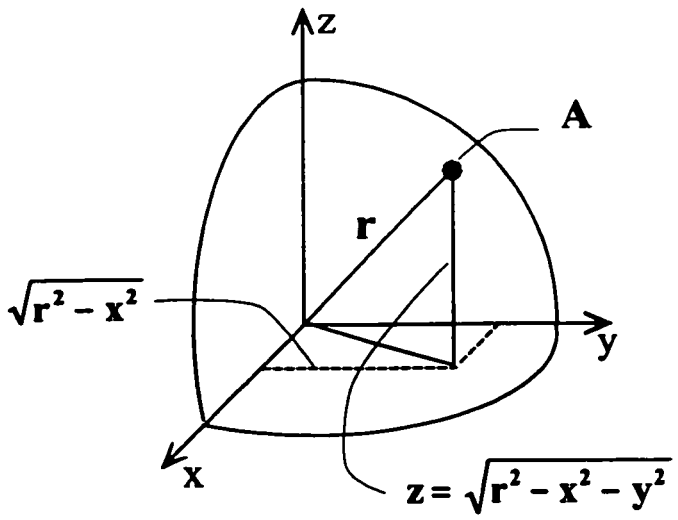

Figure 4.1: An intercept segment, z, within a quarter hemisphere of radius r.

The integral solutions for MIL, SLD, and SVD are given by:

$$\text{MIL} = \frac{\int_x\int_y 2z\,dy\,dx}{\pi r^2} = \frac{4\int_0^r\int_0^{\sqrt{r^2-x^2}} 2\sqrt{r^2 - x^2 - y^2}\,dy\,dx}{\pi r^2} = \frac{4/3\pi r^3}{\pi r^2} = \frac{4}{3}r \quad (4.5a)$$

$$\text{SLD} = \frac{\int_x\int_y (2z)^2\,dy\,dx}{\int_x\int_y 2z\,dy\,dx} = \frac{16\int_0^r\int_0^{\sqrt{r^2-x^2}} r^2 - x^2 - y^2\,dy\,dx}{4/3\pi r^3} = \frac{2\pi r^4}{4/3\pi r^3} = \frac{3}{2}r \quad (4.5b)$$

$$\text{SVD} = \frac{\pi}{3}\frac{\int_x\int_y (2z)^4\,dy\,dx}{\int_x\int_y 2z\,dy\,dx} = \frac{\pi}{3}\frac{16/3\pi r^6}{4/3\pi r^3} = \frac{4}{3}\pi r^3 \quad (4.5c)$$

Using similar integral forms, the solutions for an ellipsoid along the z-axis are

$$MIL(\hat{k}) = 4/3c \quad ; \quad SLD(\hat{k}) = 3/2c \quad ; \quad SVD(\hat{k}) = 4/3\pi c^3 \tag{4.6}$$

The solutions for the $\hat{i}$ and $\hat{j}$ directions are obtained by substituting b and a for c, respectively.

To define the APS descriptor for a sphere, one may consider a cutting plane with unit normal $\hat{k}$ positioned along the z-axis. The radius of the disc generated by the cutting plane is

$$r_z = \sqrt{r^2 - z^2} \tag{4.7}$$

Since the in-plane measurement, ρ_A, is the same for all orientations around the z-axis, the direction of the y-axis is chosen to define a single intercept length:

$$2y = 2\sqrt{r_z^2 - x^2} \tag{4.8}$$

The projected boundary of the disc is $2r_z$. Integrating in-plane along the x-axis gives the mean pore size:

$$\rho_A = \frac{1}{2r_z}\int_{-r_z}^{r_z} 2\sqrt{r_z^2 - y^2}dx = \frac{\pi r_z^2}{2r_z} = \frac{\pi}{2}r_z \tag{4.9}$$

which is the ratio of the area of the disc to its projected boundary. Finally, the orientation average along the z-axis is

$$APS(\hat{k}) = \frac{1}{2R}\int_{-R}^{R}\frac{\pi}{2}r_z dz = \frac{\pi}{4r}\int_{-r}^{r}\sqrt{r^2 - z^2}dz = \frac{\pi^2 r}{8} \tag{4.10}$$

An ellipsoid cut with a plane having unit normal $\hat{k}$ generates an ellipse when $a \neq b$. The projected boundary of the ellipse, normal to an arbitrarily chosen direction, ω, is given by

$$L(\omega) = 2\sqrt{a^2\sin^2(\omega) + b^2\cos^2(\omega)} \tag{4.11}$$

The mean in-plane pore size is the ratio of the area of the ellipse to its average projected boundary:

$$\rho_A(\hat{k}) = \frac{\pi a b}{\frac{1}{\pi}\int_0^{\pi} L(\omega)d\omega} \tag{4.12}$$

When a and b are functions of z which define the in-plane ellipse semi-axes, the integral expression for the average pore size along the z-axis is found to be:

$$\begin{aligned} APS(\hat{k}) &= \frac{1}{2c}\int_{-c}^{c} \rho_A dz \quad ; \quad a \leftarrow a\sqrt{1 - (z/c)^2} \quad ; \quad b \leftarrow b\sqrt{1 - (z/c)^2} \\ &= \frac{\pi^3 a b}{8\int_0^{\pi}\sqrt{a^2\cos^2(\omega) + b^2\sin^2(\omega)}d\omega} \end{aligned} \tag{4.13}$$

and must be evaluated by numerical means. The solutions for the $\hat{i}$ and $\hat{j}$ directions are obtained by substituting a with c and b with c, respectively.

4.2 Test Images

The descriptor measurements are controlled by a number of parameters including grid spacing, use of the pattern matching algorithm, and precise location of the sampling domain boundary by the bisection algorithm. Verification and performance assessment of the algorithms consisted of a series of parametric studies of two different images. The first image is one of a spherical inclusion, since the closed-form solution for a sphere is available

for all descriptors over all sampling orientations. The accuracy of the algorithms was verified by comparing the analytical solutions with the measurement values.

The second image is that of an ellipsoid. The ellipsoid is an oriented object which can simulate transversely isotropic and orthotropic symmetries by varying the lengths of the semi-axes. The ellipsoid was therefore chosen for verification of the orientation detection capabilities of the various descriptors and to assess the influence of the algorithm parameters on measurement accuracy.

4.3 Effect of Boundary Detection

The goal of the bisection algorithm (i.e., figure 3.6) is to locate the intersection points between a test line and the sampling domain with a high degree of precision. For comparison purposes, the search procedure within the algorithm can be turned on or off with a tolerance parameter, as described in section 3.3.1. For a spherical domain, the true length of test lines, L, is obtained from the following equation:

$$L = 2\sum_{i=1}^{N_X} |\mathbf{x}_i \cdot \hat{\mathbf{k}}| \tag{4.14}$$

The test image of a sphere with a radius of $R_G = 40$ voxels, a test line spacing of $\delta = 5$ voxels, and a precision tolerance of $\delta_b = 10^{-10}$. Measurements were obtained for orientations orthogonal to the z-axis of the image frame of reference (i.e., $\theta = \pi/2, 0 \le \varphi \le 2\pi$) in 5 degree increments. A measure of the accuracy of the bisection algorithm is the relative absolute percent error, calculated as

$$\mathrm{err}(\hat{\mathbf{v}}) = \frac{|L - L(\hat{\mathbf{v}})|}{L} \times 100\% \tag{4.15}$$

The plot in figure 4.2 shows the relative absolute percent error with and without boundary detection.

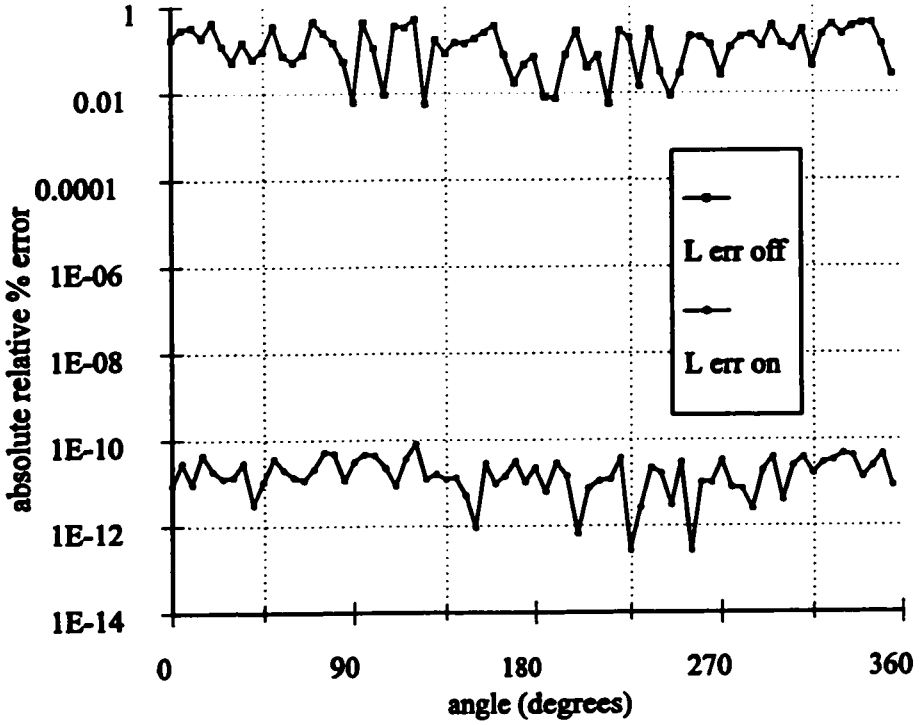

Figure 4.2: Sampling orientation versus error in sum of test line lengths, L; boundary detection on and off: sphere image.

The bisection algorithm improves the accuracy of the measured test line length by several orders of magnitude. With smaller fluctuations in test line lengths and, presumably, intercept lengths, it would seem reasonable to expect that the descriptor measurements themselves should exhibit a smoother behaviour. This improvement will only occur when large portions of the phase of interest intersect Γ_S and when δ is small relative to the dimensions of the sampling domain. For most trabecular bone images, the improvements are not appreciable, and the computational expense of searching can be avoided in favour of speeding up the scanning process.

4.4 Effect of Pattern Matching

The pattern matching algorithm is designed to filter out erroneous intercepts introduced by aliasing artifacts. These errors arise from the combined effect of representing both the true boundary of the phase of interest and the test lines in discrete form. The effect of such errors will be pronounced in binary images containing approximations of curved boundaries. In the case of a sphere, the number of intercepts will ideally remain constant for any orientation. It is expected however, that the sum of intercept lengths will vary with test line orientation and spacing, since the surface of the sphere is discretized. In order to illustrate the improvement in intercept measurements, the sphere image was scanned with two test line spacings. The first test line spacing was set at $\delta = 5$ voxels so that for each orientation, a number of test lines would be tangent to the sphere, thereby generating a significant challenge for the algorithm. The second test line spacing, $\delta = 6$ voxels, was chosen to present a less severe computational load.

Figures 4.3 a, b, and c are measurement plots corresponding to the number, sum of intercepts, and their ratio (i.e., N, $\sum$ I, MIL) taken in increments around the z-axis. The closed-form solution obtained with equation (4.5a) gives a MIL of 60 voxels. The periodic nature of the number of intercepts plot shows the influence of surface aliasing and the correction introduced by the pattern matching algorithm. The sum of intercept lengths plot in figure 4.3b shows a periodic fluctuation, which is the combined result of erroneous intercept counts and the variation in length due to the discrete approximation of the sphere boundary. In this case, the effectiveness of the algorithm is not apparent and indicates that pattern matching does not significantly improve intercept length measurements. Figure 4.3c is a plot of MIL; the ratio of intercept counts to lengths, with and without pattern matching. The reduction in measurement fluctuation illustrates the beneficial effect of pattern matching in this case.

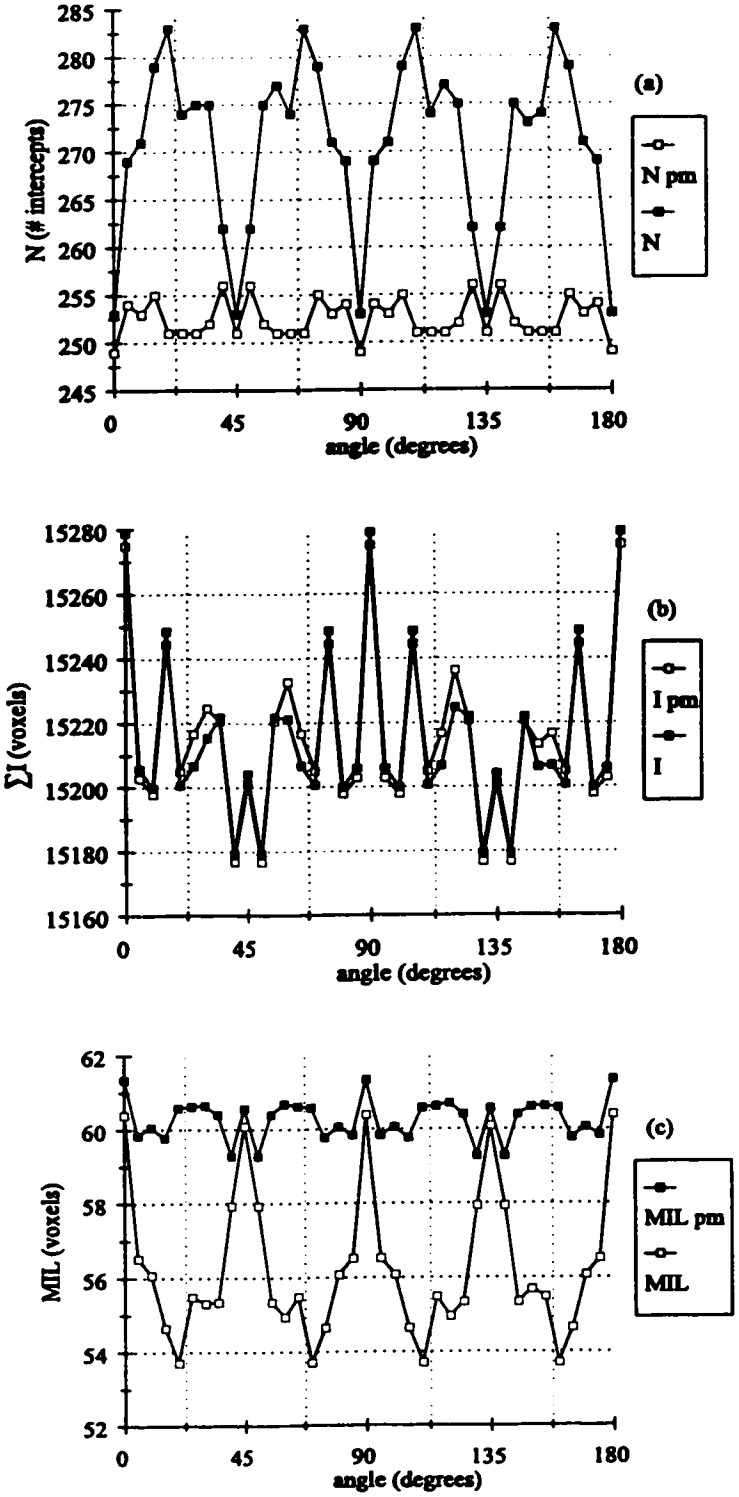

Figure 4.3: Sampling orientation versus (a) N, (b) $\sum I$, and (c) MIL; $\delta = 5$ voxels, pattern matching on ('pm') and off: sphere image.

The same improvement trend can be shown for other values of δ. In particular, for $\delta = 6$ voxels, aliasing along the discretized surface of the sphere is substantially reduced, although, as shown in figure 4.4a, false intercept counts still occur and are corrected by the pattern matching algorithm. Figure 4.4b shows similar intercept length results as were obtained with $\delta = 5$ voxels in figure 4.3b. Figure 4.4c shows a smoother distribution of MIL measurements over those in figure 4.3c due to pattern matching and the selection of test line spacing.

The sum of intercept plots for the two presented test line spacings; figures 4.3b and 4.4b, indicate that for line array based descriptors, which do not directly depend on intercept counts, such as VF, SLD and SVD, the improvement in measurement error is not appreciable. Therefore, the pattern matching algorithm can be bypassed when calculating VF, SLD or SVD in favour of increased computational speed. However, the pattern matching algorithm improves the accuracy of line array based descriptor measurements which depend on intercept counts, such as MIL, APS, and AP.

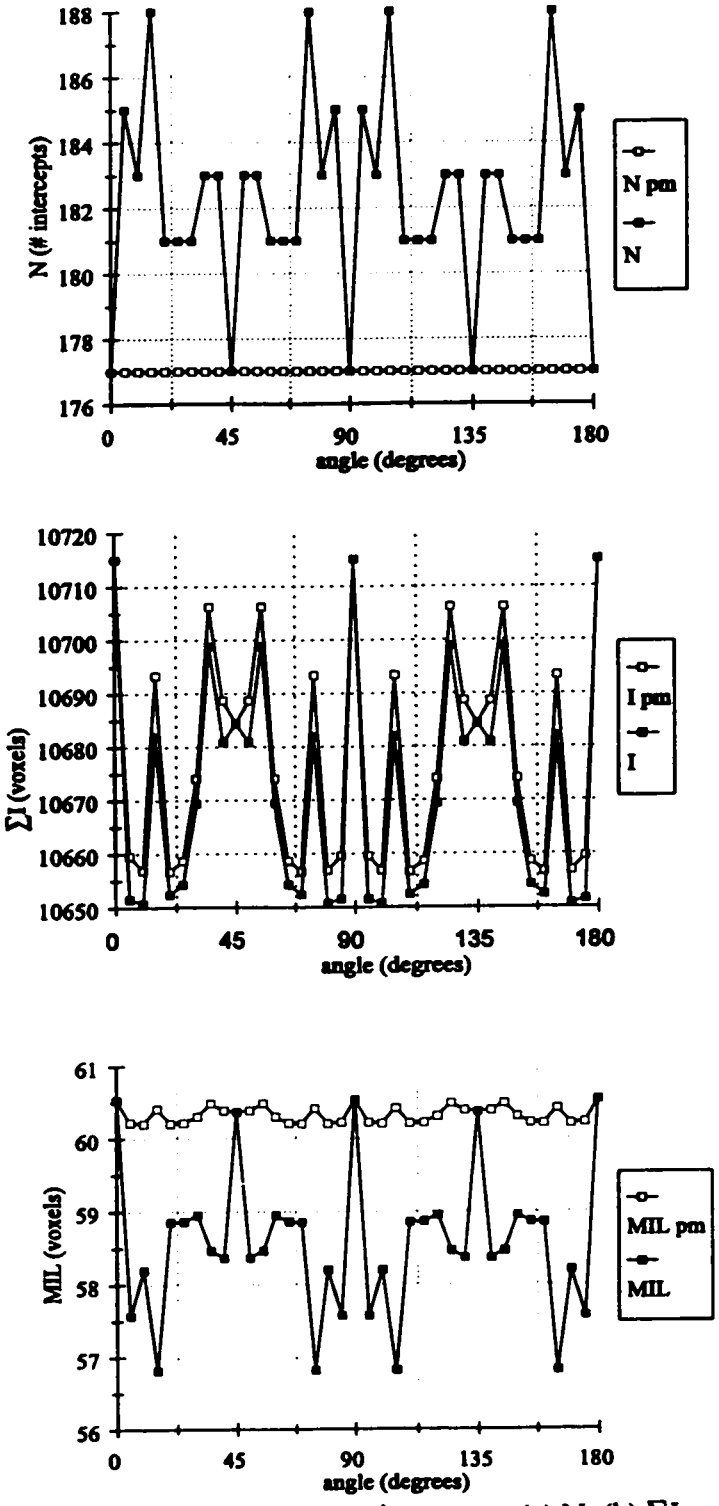

Figure 4.4: Sampling orientation versus (a) N, (b) $\sum I$, and (c) MIL; $\delta = 6$ voxels, pattern matching on ('pm') and off: sphere image.

4.5 Effect of Grid Spacing

Grid spacing is the most influential control parameter that affects the accuracy of both line array and point grid based descriptors. In this section, the influence of δ on the line array and point grid detection methods is demonstrated for the sphere test image. Grid spacing was varied from 1 to 10 voxels in 1 voxel increments. Results for the line array algorithms are presented in section 4.5.1, while those for the point grid algorithms are given in section 4.5.2.

4.5.1 Line Array Algorithms

Based on the discussions in sections 4.3 and 4.4, pattern matching and precision boundary detection algorithms were employed for measuring both MIL and SLD. Measurements were obtained for 36 orientations orthogonal to the x_3-axis (i.e., $\theta = \pi/2, 0 \leq \varphi \leq 2\pi$) in 5 degree increments. The absolute relative percent error between the theoretical and measured descriptor value was calculated for each spacing and orientation configuration. The average error was then determined over all orientations for each spacing value. Figure 4.5 shows a plot of test line spacing versus mean relative percent error in MIL and SLD. Both series indicate that a decrease in measurement error is generally attained with a decrease in test line spacing.

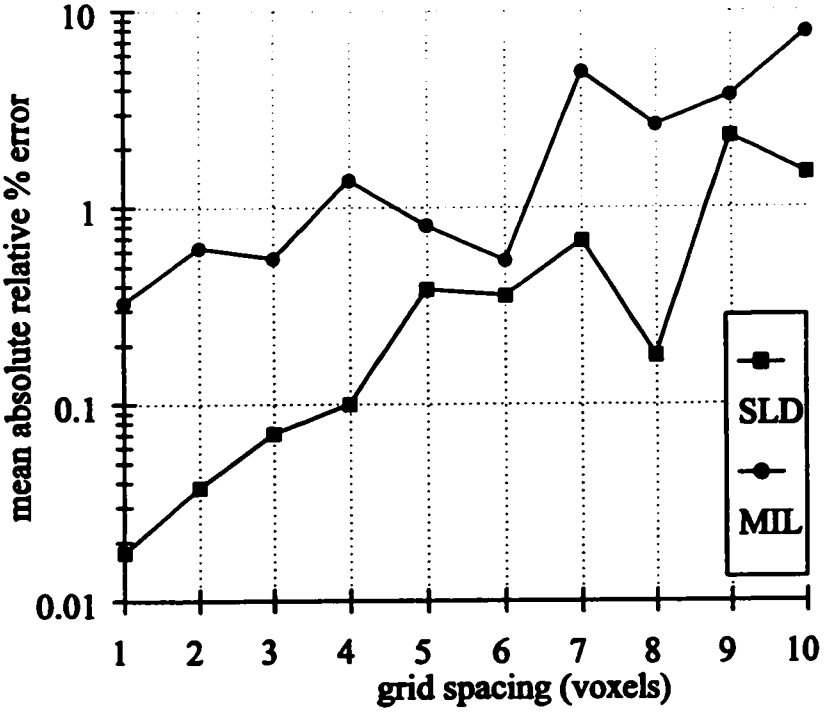

Figure 4.5: Grid spacing versus error in MIL and SLD (line array algorithm): sphere image.

4.5.2 Point Grid Algorithms

The approach here is similar to that of section 4.5.1. In this case, however, a uniform distribution of sampling directions, generated by the spiral points method, was applied at each grid point. Orientation results for SLD and SVD were averaged and the mean absolute relative percent error was determined for the range of grid spacings, as shown in figure 4.6. The significance is that the point grid approach provides comparable or better results, in terms of measurement accuracy, to those obtained with the line array algorithm, as presented in figure 4.5. As with the line array algorithm, measurement accuracy generally improves with decreasing grid spacing.

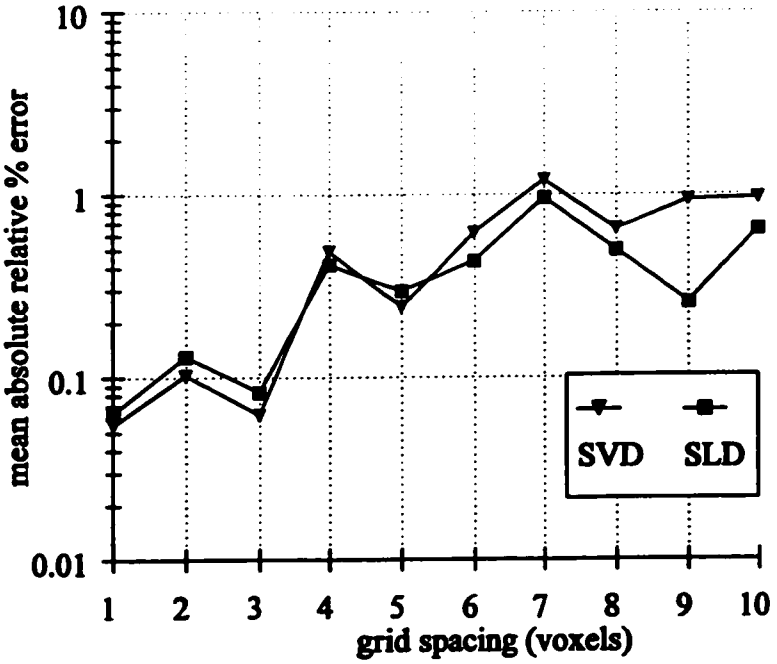

Figure 4.6: Grid spacing versus error in SVD and SLD; point grid algorithm: sphere image.

4.6 Detection of Fabric Orientation

The test image of an ellipsoid with semi-axes of lengths a = 30, b = 50, and c = 70 voxels was generated and then rotated such that its local axes were aligned with the basis defined by equation (3.7) with $\theta = \varphi = \pi/4$. To measure the orientation triad, the coefficients D_{ij} in equation (2.8) were determined by a data fitting procedure. The details of the procedure are provided in chapter 5, and are not in themselves a pre-requisite for assessing the orientation detection capabilities of the various descriptors. A uniform distribution of 50 sampling directions was generated via the spiral points method for use in the line array and point grid algorithms. A second order fit of the data was obtained and the eigenvectors of D_{ij} were determined. The measurement error was quantitatively assessed as the mean angular deviation of the eigenvectors, $\hat{\mathbf{e}}$, from the known orientation triad with the

equation:

$$\bar{\alpha} = \frac{180}{3\pi} \sum_{i=1}^{3} \min(\cos^{-1} | \hat{\omega}_i \cdot \hat{e}_n |) \tag{4.16}$$

where $\bar{\alpha}$ is the mean angular deviation and $\hat{\omega}_i$ are the orientations of the ellipsoid semi-axes relative to the image frame of reference.

Figure 4.7 shows the error results for all of the line array based descriptors. With the exception of APS, all fabric descriptors give good results over a range of test line spacings. The implication is that for isolated voids or solid particles, the detection of orientation is not significantly affected by (reasonable) selection of grid spacing. Therefore, for orientation detection measurements, the criterion for descriptor selection may be that of computational efficiency.

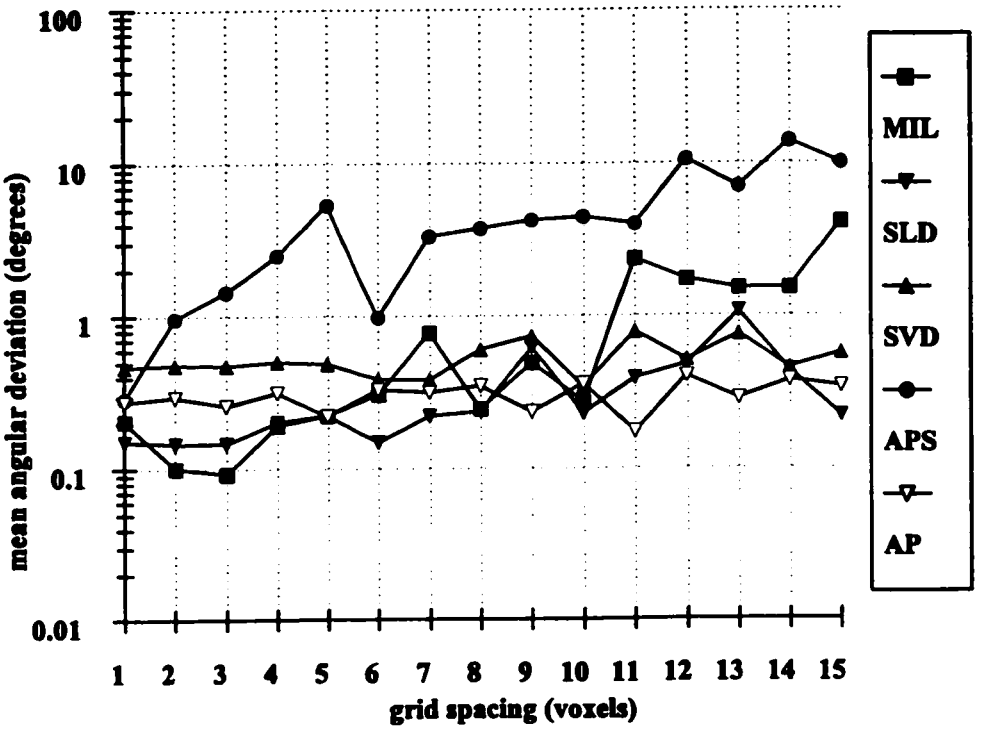

Figure 4.7: Grid spacing versus mean angular deviation of detected basis from known basis directions; line array descriptors: ellipsoid image.

Figure 4.8 provides a comparison between line and point grid based algorithms for SLD and SVD in terms of the dependence of orientation detection accuracy on grid spacing. Point grid measurements are identified with a suffix 'II' to distinguish them from the corresponding line array measurements (i.e., SLD vs. SLDII). The results are similar for both algorithm types with SLD generally achieving greater accuracy than that of SVD over a wide range of grid spacings. This is not unexpected, since with SVD, measurement errors associated with individual intercept lengths will be magnified by a power of two over those obtained by SLD.

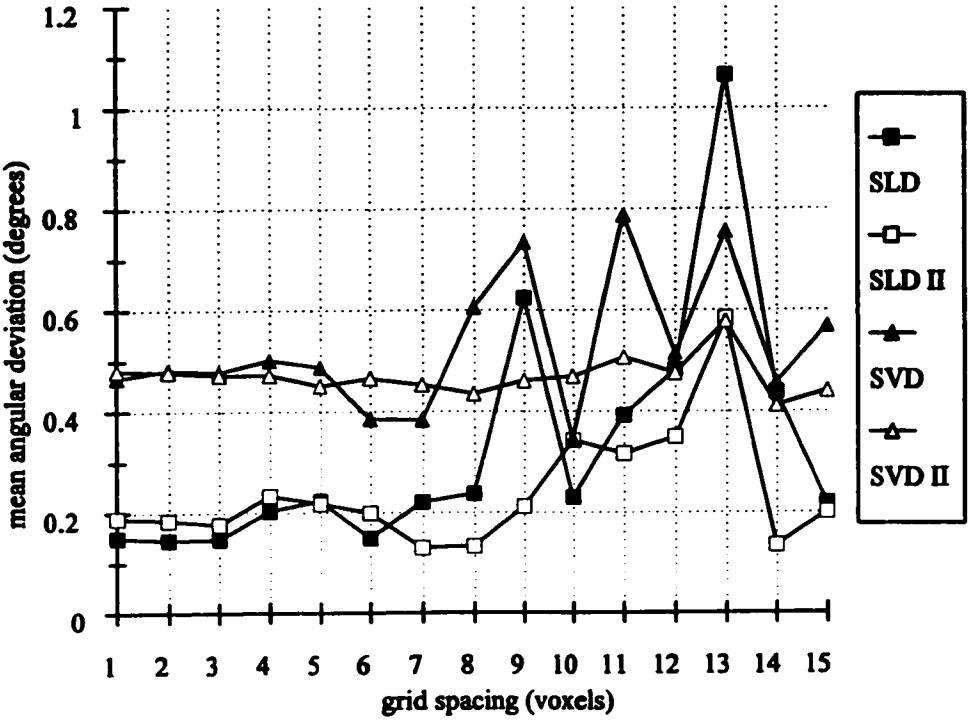

Figure 4.8: Grid spacing versus mean angular deviation of detected basis from known basis directions; comparison of line array and point grid descriptors, SLD and SVD: ellipsoid image.

4.7 Algorithm Efficiency

To assess the efficiency of algorithms for different fabric descriptors, a batch program was written to loop over the various detector algorithms, scanning the ellipse test image, each with grid spacings from 1 to 10 voxels and a set of 50 spiral points. In addition, the use of boundary detection and pattern matching was retained. Run times were logged on an Intel Celeron 466 MHz CPU, with 128 Mb SDRAM under Windows 98 operating system. The algorithms were coded in the object oriented C++ language and compiled under Borland C++ Builder version 4 with the compiler settings optimized for speed.

The algorithms for obtaining APS and AP measurements (i.e., figures 3.18, 3.19, section 3.3.2) were employed with the number of in-plane rotations, N_ψ, set at 18. No attempt was made at separating the algorithms presented in figures 3.16 and 3.22, since the additional computational overhead in calculating a sum of powers was considered to be insignificant in comparison with the main looping structures. Figure 4.9 is a plot of the execution time versus grid spacing for the four algorithms applied to the ellipse image. The APS algorithm requires the most processing time, due to the additional in-plane averaging around the sampling direction. As indicated by data series "APS/N_ψ", if the measured execution time is reduced by N_ψ, the speed is comparable to that of the uniform line array algorithm (i.e., figure 3.16). The difference in this case arises from the fact that the number of test lines, with the exception of a grid spacing of 1, is always larger for the APS algorithm. The AP algorithm is generally faster than the other algorithms up to a certain grid spacing, where the effect of additional in-plane rotations becomes apparent. The range of times shown correspond to a maximum of approximately 120 minutes for the APS algorithm at $\delta = 1$ voxel to a minimum of 3.6 seconds for the point grid algorithm at $\delta = 10$ voxels.

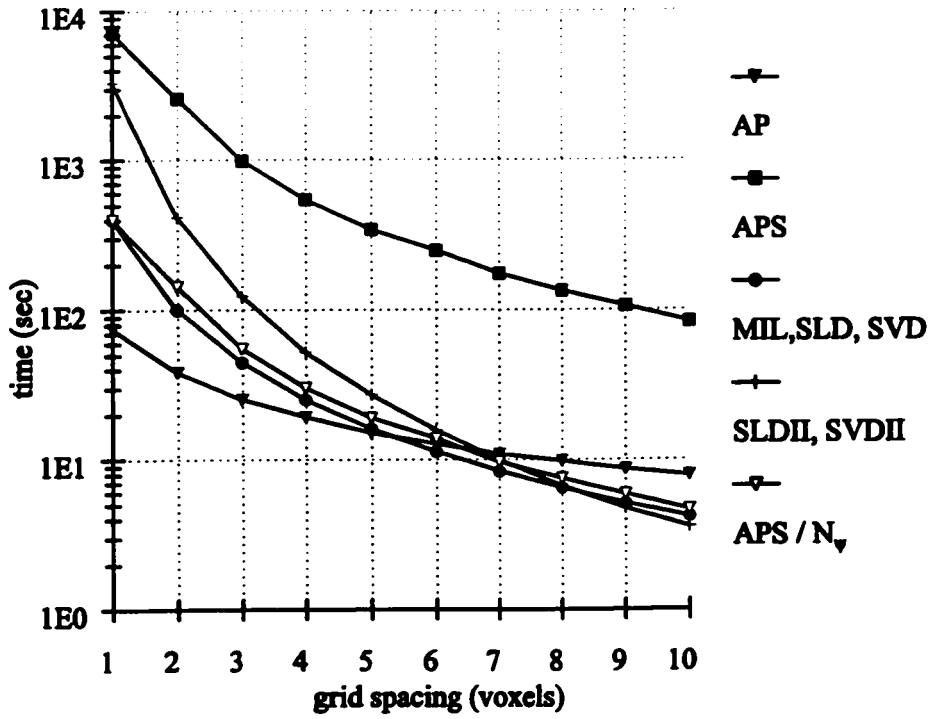

Figure 4.9: Grid spacing versus execution time for different algorithms: ellipse image.

Figure 4.10 shows the number of sampling elements; grid points or test lines, plotted against grid spacing. In comparison with figure 4.9, it is evident that the speed of execution is directly related to the number of sampling elements for all algorithms. Note that for line array algorithms, the additional computational overhead of pattern matching is evident when the trends are compared with those in figure 4.9.

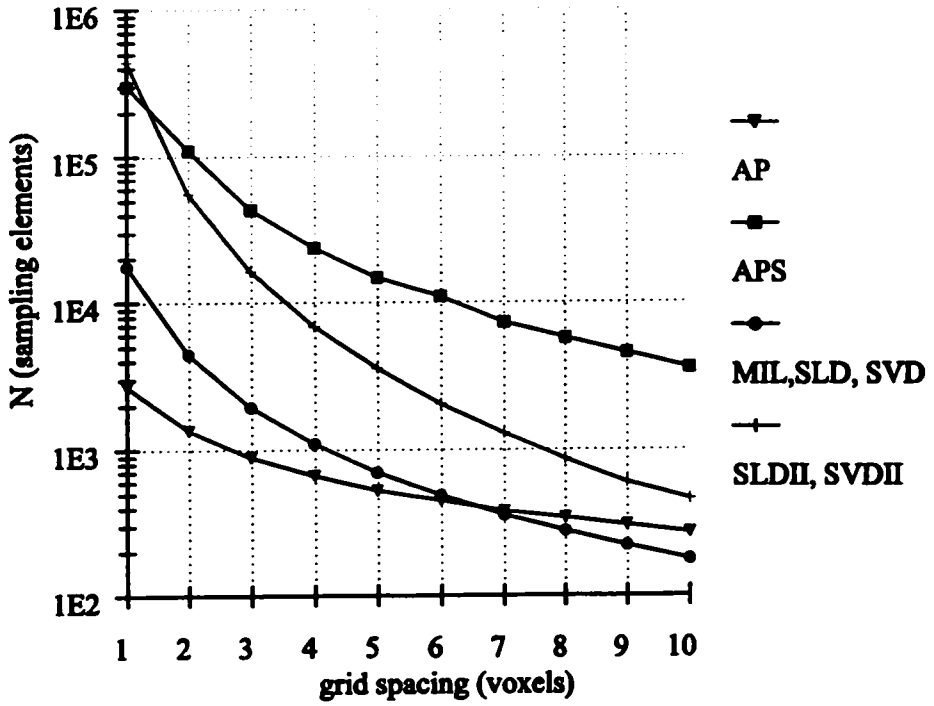

Figure 4.10: Grid spacing versus number of sampling elements for different algorithms: ellipse image.

4.8 Final Remarks

The preceding parametric studies demonstrate that the algorithms perform correctly and that computer generated images of objects having known orientation and analytical descriptor solutions are measurable with parameter dependent accuracy and speed. In general, measurement errors depend in a complex manner on the topology of the object being measured, sampling orientation, and grid spacing. They are therefore difficult to minimize in a precise and consistent manner. However, a decrease in grid spacing generally results in an improvement in accuracy for both line array and point grid algorithms, but at the cost of

an increase in execution time. Additional improvement in measurement accuracy can be attained via the pattern matching algorithm for the line array descriptors; MIL, APS, and AP, which are sensitive to false intercept counts. When combined with the data fitting procedure outlined next, in chapter 5, most of the descriptors provide orientation detection capability with accurate results over a wide range of grid spacings.

As with many discrete numerical procedures, the choice of sample spacing is subject to considerable latitude and is left to the discretion of the analyst. Clearly, a grid spacing of 1 voxel provides the assurance of obtaining accurate measurements regardless of the choice of descriptor or the topology of the object being scanned. However, this approach is inefficient and in some applications may be prohibitively time consuming. One way of assessing the sensitivity to grid spacing is to measure VF over a range of grid spacings and compare the results to the true value obtained by counting voxels directly. As an example, figure 4.11 shows a plot of grid spacing versus mean VF error, obtained from 50 spiral points sampling orientations applied to the sphere image, with pattern matching off. The interpretation is that accurate results (i.e., < 0.3 % error) are generated up to a grid spacing of 6 voxels. This is in agreement with the results presented earlier in figures 4.5 and 4.6 for several conceptually different descriptors.

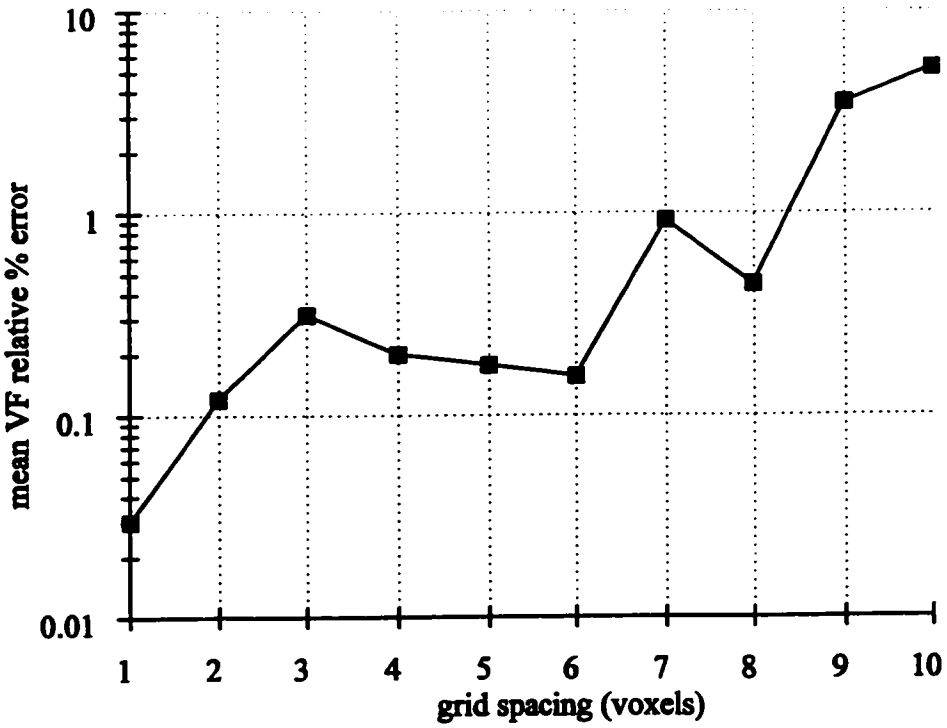

Figure 4.11: Grid spacing versus mean VF relative % error: sphere image.

CHAPTER 5 Least Squares Procedures

In this chapter, a descriptor measurement fitting algorithm is developed based on the least squares approach, introduced in section 5.1. Owing to the nature of the data acquisition algorithms developed in chapter 3, the assumption of homogeneous error variance is violated and the basic least squares model must be augmented. The problems associated with a lack of homogeneous error variance, discussed in section 5.2, are resolved by implementing an iteratively re-weighted least squares (IRWLS) procedure, presented in section 5.3. Higher order approximations to the data, wherein the coefficients in equation (2.8) are themselves nonlinear, are obtained by a combined IRWLS and Levenberg-Marquardt optimization strategy, described in detail in section 5.4.

5.1 General Least Squares

In the least squares approach, the representation of a linear function is

$$f(\mathbf{x}) = \beta_1 x_1 + \beta_2 x_2 + \ldots + \beta_p x_p \tag{5.1}$$

The general least squares model for estimating the coefficients in equation (5.1) is

$$\mathbf{y} = \mathbf{X}\boldsymbol{\beta} + \boldsymbol{\varepsilon} \tag{5.2}$$

$\mathbf{y}$ is an m×1 column vector of measurement data, $\mathbf{X}$ is an m×p matrix of regressor variables, and $\boldsymbol{\beta}$ is a p×1 column vector of regression coefficients. $\boldsymbol{\varepsilon}$ is an m×1 column vector of approximation errors, or residuals, which describe the random disturbance not accounted for

by the coefficients under the assumption of homogeneous error variance (i.e., $\mathrm{Var}(\varepsilon) = \sigma^2 \mathbf{I}$). An estimate of β is given by the ordinary least squares estimator:

$$\mathbf{b} = [\mathbf{X}^T \mathbf{X}]^{-1} \mathbf{X}^T \mathbf{y} \tag{5.3}$$

Then the approximation of the k^{th} observation is:

$$\hat{y}_k = \mathbf{b}^T \cdot \mathbf{x}_k = b_1 x_{1_k} + b_2 x_{2_k} + \ldots + b_p x_{p_k} \tag{5.4}$$

With the standard linear procedure, given m fabric measurements, $y_k(\hat{\mathbf{v}}_k)$; $k = 1, 2, \ldots, m$, one may solve for C and D_{ij} using equation (5.3). Specifically, with respect to the coefficients in equation (2.3), their correspondence with b_i, and the definitions of the regressors, x_i, are as follows:

$$\begin{aligned}
&C = b_1, \; x_1 = 1 ; && D_{11} = \frac{b_2}{b_1}, \; x_2 = \hat{v}_1^2 - \hat{v}_3^2 \\
&D_{22} = \frac{b_3}{b_1}, \; x_3 = \hat{v}_2^2 - \hat{v}_3^2 ; && D_{12} = \frac{b_4}{2b_1}, \; x_4 = \hat{v}_1 \hat{v}_2 \\
&D_{13} = \frac{b_5}{2b_1}, \; x_5 = \hat{v}_1 \hat{v}_3 ; && D_{23} = \frac{b_6}{2b_1}, \; x_6 = \hat{v}_2 \hat{v}_3
\end{aligned} \tag{5.5}$$

With regard to the alternative formulation; i.e. equation (2.4), the relations between C, A_{ij}, the regressors and the coefficients are:

$$\begin{aligned}
&C = \frac{b_3}{3}, \; x_1 = \hat{v}_1^2 - \hat{v}_3^2 ; && A_{11} = \frac{b_1}{b_3}, \; x_2 = \hat{v}_2^2 - \hat{v}_3^2 \\
&A_{22} = \frac{b_2}{b_3}, \; x_3 = \hat{v}_3^2 ; && A_{12} = \frac{b_4}{2b_3}, \; x_4 = \hat{v}_1 \hat{v}_2 \\
&A_{13} = \frac{b_5}{2b_3}, \; x_5 = \hat{v}_1 \hat{v}_3 ; && A_{23} = \frac{b_6}{2b_3}, \; x_6 = \hat{v}_2 \hat{v}_3
\end{aligned} \tag{5.6}$$

5.2 Problems with Least Squares Estimates

The results of the verification experiments of sections 4.3 and 4.4 demonstrate the absence of homogeneous error variance. A more generalized approach which may account for heterogeneous error variance assumes there is a positive definite matrix, **V**, for which

$$\mathrm{Var}(\boldsymbol{\varepsilon}) = \mathbf{V} \quad ; \quad \mathbf{V} = \mathbf{I}[\sigma_1^2, \sigma_2^2, ..., \sigma_m^2]^T \tag{5.7}$$

Thus, the observations are now weighted by the reciprocal of the error standard deviation (i.e., $w_k = 1/\sigma_k^2$) and the weighted least squares estimator, **a**, is given by

$$\mathbf{a} = [\mathbf{X}^T\mathbf{W}\mathbf{X}]^{-1}\mathbf{X}^T\mathbf{W}\mathbf{y} \quad ; \quad \mathbf{W} = \mathbf{V}^{-1} \tag{5.8}$$

The implication is that observations with large error variances should have less influence. It is important to note that a priori information about the error standard deviation is assumed to be available. In typical situations, estimates of σ_k can be obtained by repeated measurements with the regressors held constant. This is not applicable in the computational procedures discussed previously in chapter 3, since for repeated observations at a given $\hat{\mathbf{v}}_k$, the corresponding measurement values are the same. A general procedure which is resistant to the non-ideal condition and which 'weights down' the influence of variant data points is described by Myers (1990). In terms of the preceding definitions, the vector of residuals, $\hat{\boldsymbol{\varepsilon}}$, is given by

$$\hat{\boldsymbol{\varepsilon}} = \mathbf{y} - \hat{\mathbf{y}} = \mathbf{y} - \mathbf{X}\mathbf{a} \tag{5.9}$$

Then the least squares estimation problem can be viewed as a special case of the solution to:

$$\sum_k \Psi(\hat{\varepsilon}_k/\sigma)\mathbf{x}_k = \mathbf{0} \tag{5.10}$$

where $\Psi(\cdot)$ is an 'influence function.' Equation (5.10) illustrates that the influence exerted by the k^{th} data point is proportional to its residual when $\Psi(\cdot)$ is linear in $\hat{\varepsilon}_k$. The influence function can be formulated to reduce the influence of data points containing large errors of fit. Huber's influence function (Myers, 1990) for obtaining weights, such that $w_k \in (0, 1]$, is defined as

$$\begin{aligned} \Psi(\hat{\varepsilon}_k^*) &= 1 \quad ; \quad |\hat{\varepsilon}_k^*| \le r \\ &= r/\hat{\varepsilon}_k^* \quad ; \quad \hat{\varepsilon}_k^* > r \\ &= -r/\hat{\varepsilon}_k^* \quad ; \quad \hat{\varepsilon}_k^* < -r \end{aligned} \tag{5.11}$$

where $\hat{\varepsilon}_k^* = \hat{\varepsilon}_k / \sigma$ and $r = 1$. Thus, residuals that exceed σ exert no more influence than a residual of σ. Since σ is unknown, it is estimated with $\hat{\sigma}$ obtained in some robust sense. Myers (1990) recommends scaling the median residual error to estimate σ: $\hat{\sigma} = 1.5 \text{ med}|\hat{\varepsilon}_k|$.

5.3 The IRWLS Algorithm

Figure 5.1 outlines the IRWLS algorithm employed in this thesis, using the pseudocode specification of section 3.1. The initial set of weights is set to unity and then updated with Huber's influence function for the remaining iterations. Convergence is achieved when the difference in sums of absolute residual errors between iterations is less than a specified tolerance (e.g., $\delta_e = 10^{-6}$).

$\mathbf{W} \leftarrow \mathbf{I}$;
$e_{prev} \leftarrow \Delta_e \leftarrow 2\delta_e$;
do
  $\mathbf{a} \leftarrow [\mathbf{X}^T\mathbf{W}\mathbf{X}]^{-1}\mathbf{X}^T\mathbf{W}\mathbf{y}$;
  $\hat{\varepsilon} \leftarrow \mathbf{y} - \mathbf{X}\mathbf{a}$;
  $\hat{\sigma} \leftarrow 1.5\,\mathrm{med}|\hat{\varepsilon}|$;
  $\hat{\varepsilon}^* \leftarrow \hat{\varepsilon}/\hat{\sigma}$;
  $\mathbf{W} \leftarrow \mathbf{I}\Psi(\hat{\varepsilon}^*)$;
  $e_{curr} \leftarrow \sum |\hat{\varepsilon}_k|$;
  $\Delta_e \leftarrow e_{prev} - e_{curr}$;
  $e_{prev} \leftarrow e_{curr}$;
while$(\Delta_e > \delta_e)$

Figure 5.1: Iteratively re-weighted least squares algorithm; $\mathbf{a} \leftarrow IRWLS(\mathbf{X},\mathbf{y},\delta_e)$.

As an illustration of the effectiveness of the procedure, SVD measurements of a trabecular bone sample were obtained in the x'_1-x'_3 plane ($\varphi = 0, 0 \le \theta \le \pi/2$) via the algorithm shown in figure 3.16. For demonstration purposes, the data were fit to a 2D distribution function of the form

$$f(\hat{\mathbf{v}}, n) = C_1(1 + \hat{\mathbf{v}}^T\mathbf{D}\hat{\mathbf{v}} + \sum_{i=2}^{n} C_i(\hat{\mathbf{v}}^T\mathbf{D}\hat{\mathbf{v}})^i) \tag{5.12a}$$

$$\mathbf{D} = \begin{bmatrix} D_{11} & D_{12} \\ D_{12} & D_{22} \end{bmatrix} \quad ; \quad \hat{\mathbf{v}} = [\cos(\theta), \sin(\theta)]^T \tag{5.12b}$$

with n = 1. The plot in figure 5.2 shows the fit obtained with equation (5.3) and the fit obtained via the IRWLS algorithm. The influence of outliers (i.e., $w_k < 1$) in the raw measurement data is clearly apparent.

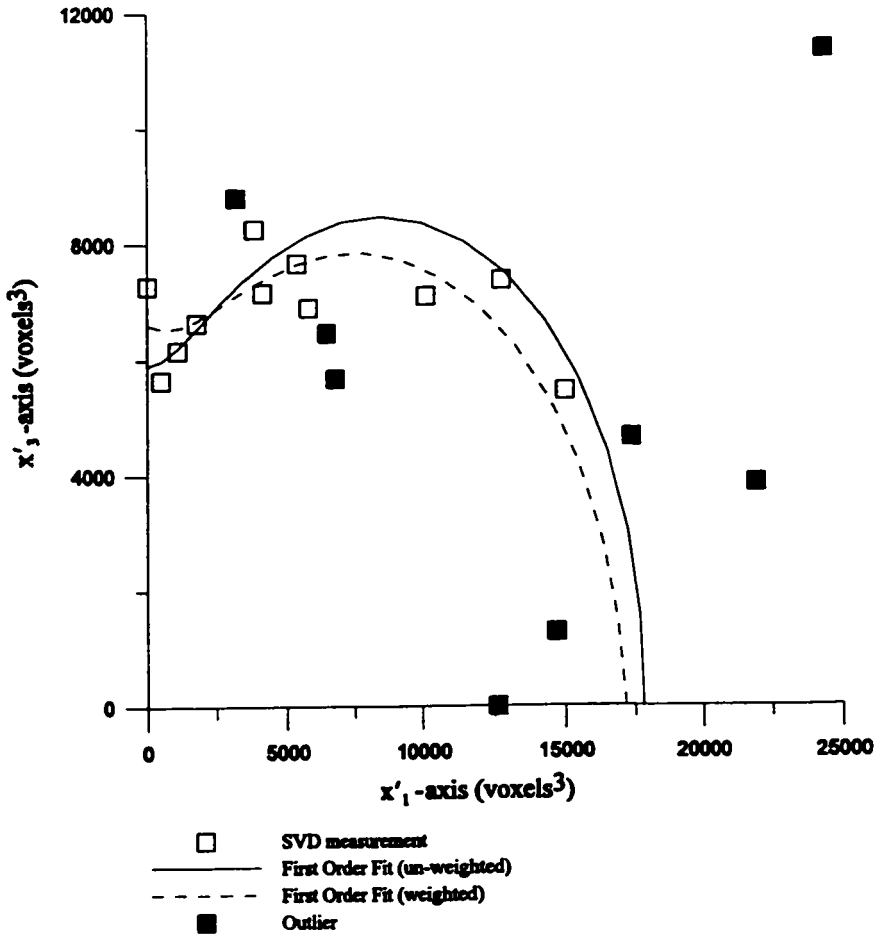

Figure 5.2: SVD measured in the x'_1-x'_3 plane with standard and IRWLS fits.

5.4 A Non-Linear IRWLS Algorithm

A modified algorithm is necessary for fitting higher order distribution functions (e.g., equation (2.8) or equation (5.12) with n > 1) wherein the coefficients of D_{ij} become nonlinear and the linear estimator fails. The same iteratively re-weighted procedure and

influence function are used to determine the weights, except that an unconstrained optimization algorithm must be employed to establish the parameters. The details of the mathematical derivations of a Levenberg-Marquardt optimization strategy, which includes the weighting terms, are presented next.

An estimate of the n^{th} order distribution function (i.e., equation (2.8)) evaluated at the k^{th} data point is written $F(\hat{\mathbf{v}}_k, \mathbf{a})$, where $\mathbf{a}$ is a vector of parameter estimates such that

$$\begin{aligned} \mathbf{a}_{1\ldots5} &= \{D_{11}, D_{12}, D_{13}, D_{23}, D_{22}\} \\ \mathbf{a}_{6\ldots n+5} &= \{C_1, C_2, \ldots, C_n\} \end{aligned} \tag{5.13}$$

The problem at each iteration is to minimize the sum of weighted squared residuals:

$$S(\mathbf{a}) = \hat{\boldsymbol{\varepsilon}}^T \mathbf{W} \hat{\boldsymbol{\varepsilon}} \tag{5.14}$$

where the residuals are functions of F:

$$\hat{\varepsilon}_k = y_k - F(\hat{\mathbf{v}}_k, \mathbf{a}) \equiv y_k - F_k \quad ; \quad k = 1, 2, \ldots, m \tag{5.15}$$

The first and second order derivatives of S, in terms of the residuals and their weights, are given by

$$\begin{aligned} \nabla S &= -2\mathbf{J}\mathbf{W}\hat{\boldsymbol{\varepsilon}} \quad ; \quad J_{rs} = \frac{\partial F_s}{\partial a_r} \\ \nabla^2 S &= 2\mathbf{J}\mathbf{W}\mathbf{J}^T - 2\mathbf{H} \quad ; \quad H_{qr} = \sum_{k=1}^{m} \frac{\partial^2 F_k}{\partial a_q \partial a_r} w_k \hat{\varepsilon}_k \end{aligned} \tag{5.16}$$

where $\mathbf{J}$ is a p×m Jacobian matrix and $\mathbf{H}$ is a p×p matrix of second order derivatives (p = n + 5). According to Press et al. (1992), the higher order terms of the Hessian matrix can be neglected so that

$$\nabla^2 S \approx 2\mathbf{J}\mathbf{W}\mathbf{J}^T \tag{5.17}$$

Near some current estimate, $\mathbf{a}_i$, a Taylor's series expansion up to second order gives

$$S(\mathbf{a}) = S(\mathbf{a}_i) + (\mathbf{a} - \mathbf{a}_i)^T \nabla S(\mathbf{a}_i) + \frac{1}{2}(\mathbf{a} - \mathbf{a}_i)^T \nabla^2 S(\mathbf{a}_i)(\mathbf{a} - \mathbf{a}_i) \qquad (5.18)$$

Setting $\Delta S = 0$ determines the increment used to obtain the next iteration point:

$$\delta\mathbf{a} = \mathbf{a} - \mathbf{a}_i = -[\nabla^2 S(\mathbf{a}_i)]^{-1} \nabla S(\mathbf{a}_i) \qquad (5.19)$$

A related equation is obtained by replacing the inverse of the Hessian with a constant, as in

$$\delta\mathbf{a} = \alpha \nabla S(\mathbf{a}_i) \qquad (5.20)$$

Here α controls the step size along the direction of steepest descent defined by the gradient of S. The Levenberg-Marquardt method uses a trust-region approach, also known as ridge regression or regularization, to shrink the step sizes to ensure a reduction in S at each iteration. The increment in terms of $\mathbf{J}$, $\mathbf{W}$ and $\hat{\boldsymbol{\varepsilon}}$ is given by

$$\delta\mathbf{a} = [\mathbf{J}\mathbf{W}\mathbf{J}^T + \lambda\mathbf{G}]^{-1}\mathbf{J}\mathbf{W}\hat{\boldsymbol{\varepsilon}} \qquad (5.21)$$

where $\lambda\mathbf{G}$ is a diagonal matrix which acts as a damping term. Levenberg (1944) originally proposed that $\mathbf{G} = \mathbf{I}$, while Marquardt (1963) suggested $\mathbf{G} = \text{diag}(\mathbf{J}\mathbf{W}\mathbf{J}^T)$ to account for the fact that the diagonal elements of the Hessian can be of vastly different magnitude. When λ is large, equation (5.21) is essentially in effect. Conversely, as λ approaches zero equation (5.20) is in effect.

The Levenberg-Marquardt algorithm, shown in figure 5.3, is initialized with a set of weights, initial guesses of the parameters, and a number of control parameters (e.g., $\lambda_0 = 10^{-4}$, $\delta_\lambda = 10$, $\delta_s = 10^{-3}$, N = 1000). For brevity, the expressions $\hat{\boldsymbol{\varepsilon}}(\cdot)$, $\mathbf{J}(\cdot)$, and $\mathbf{G}(\cdot)$ represent functions which return the associated vector or matrix evaluated at the specified vector argument. A sub-iteration procedure is used to determine λ which minimizes S based on the current estimate of $\mathbf{a}$. The algorithm terminates either when significant reduction in S is no longer observed, or the maximum number of iterations, N, is reached.

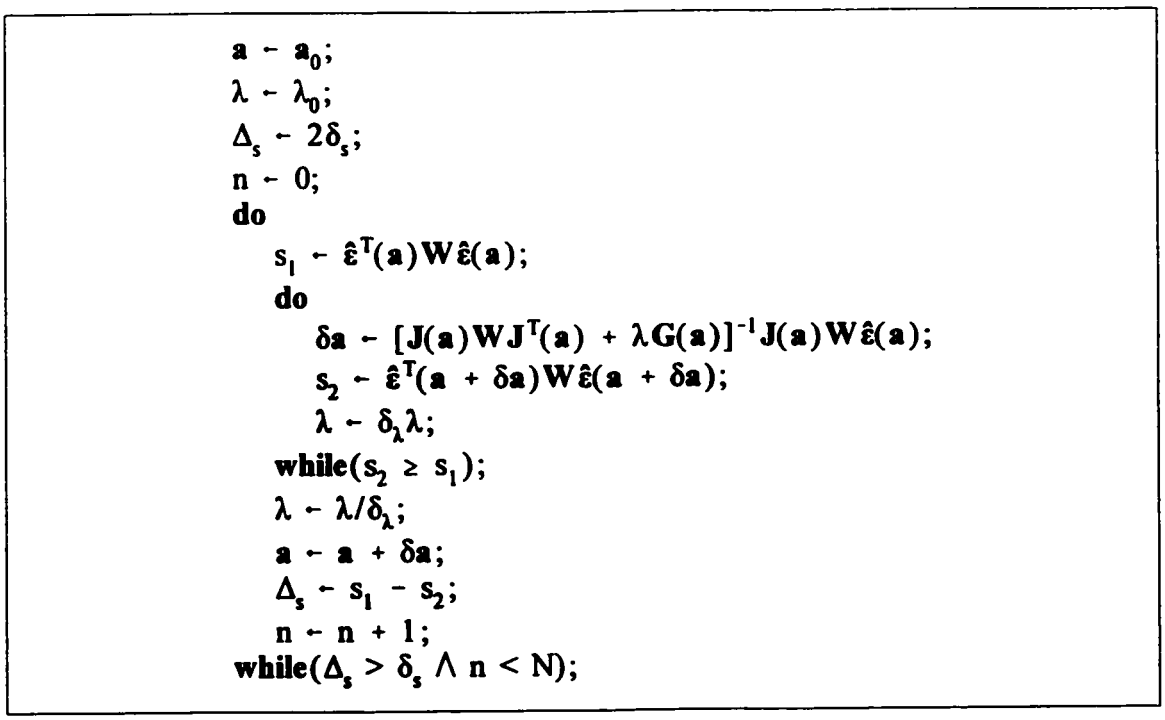

$\mathbf{a} \leftarrow \mathbf{a}_0$;
$\lambda \leftarrow \lambda_0$;
$\Delta_s \leftarrow 2\delta_s$;
$n \leftarrow 0$;
do
  $s_1 \leftarrow \hat{\varepsilon}^T(\mathbf{a})\mathbf{W}\hat{\varepsilon}(\mathbf{a})$;
  do
    $\delta\mathbf{a} \leftarrow [\mathbf{J}(\mathbf{a})\mathbf{W}\mathbf{J}^T(\mathbf{a}) + \lambda\mathbf{G}(\mathbf{a})]^{-1}\mathbf{J}(\mathbf{a})\mathbf{W}\hat{\varepsilon}(\mathbf{a})$;
    $s_2 \leftarrow \hat{\varepsilon}^T(\mathbf{a} + \delta\mathbf{a})\mathbf{W}\hat{\varepsilon}(\mathbf{a} + \delta\mathbf{a})$;
    $\lambda \leftarrow \delta_\lambda\lambda$;
  while$(s_2 \geq s_1)$;
  $\lambda \leftarrow \lambda/\delta_\lambda$;
  $\mathbf{a} \leftarrow \mathbf{a} + \delta\mathbf{a}$;
  $\Delta_s \leftarrow s_1 - s_2$;
  $n \leftarrow n + 1$;
while$(\Delta_s > \delta_s \wedge n < N)$;

Figure 5.3: The Levenberg-Marquardt algorithm;
$\{\mathbf{a}, \hat{\varepsilon}, n\} \leftarrow$ *LevenbergMarquardt*$(\mathbf{W}, \mathbf{a}_0, \lambda_0, \delta_\lambda, \delta_s, N)$.

A few minor changes to the algorithm in figure 5.1 produces the iteratively re-weighted nonlinear least squares (IRWNLLS) procedure shown in figure 5.4. The algorithm begins with an initial guess obtained by estimating the first order coefficients of equation (2.8) with equation (5.3). The remaining components of **a** corresponding to C_2, C_3, ... , C_n are set to zero. Within the re-weighting loop, the current parameter estimates and the residual vector are obtained via the Levenberg-Marquardt algorithm. The weights are calculated as in figure 5.1. Finally, the termination condition has been modified to reflect the convergence criteria in figure 5.3.

$\mathbf{W} \leftarrow \mathbf{I}$;
$e_{prev} \leftarrow \Delta_e \leftarrow 2\delta_e$;
$\mathbf{a} \leftarrow [\mathbf{X}^T\mathbf{X}]^{-1}\mathbf{X}^T\mathbf{y}$;
$n \leftarrow 0$;
do
  $\{\mathbf{a}, \hat{\varepsilon}, n\} \leftarrow$ *LevenbergMarquardt*$(\mathbf{W}, \mathbf{a}, \lambda_0, \delta_\lambda, \lambda_s, N)$;
  $\hat{\sigma} \leftarrow 1.5\,\mathrm{med}|\hat{\varepsilon}|$;
  $\hat{\varepsilon}^* \leftarrow \hat{\varepsilon}/\hat{\sigma}$;
  $\mathbf{W} \leftarrow \mathbf{I}\Psi(\hat{\varepsilon}^*)$;
  $e_{curr} \leftarrow \sum |\hat{\varepsilon}_k|$;
  $\Delta_e \leftarrow e_{prev} - e_{curr}$;
  $e_{prev} \leftarrow e_{curr}$;
while$(\Delta_e > \delta_e \wedge n < N)$

Figure 5.4: Iteratively re-weighted, non-linear least squares algorithm; $\{\mathbf{a}, n\} \leftarrow$ *IRWNLLS*$(\mathbf{X}, \mathbf{y}, \delta_e, \lambda_0, \delta_\lambda, \delta_s, N)$.

Figure 5.5 demonstrates the effect of increasing the order of fit to the SVD data sampled in the x'_1-x'_3 plane. The third order, un-weighted fit is strongly influenced by the indicated outliers. The weighted third order fit provides a noticeable improvement over both first order and un-weighted third order fits.

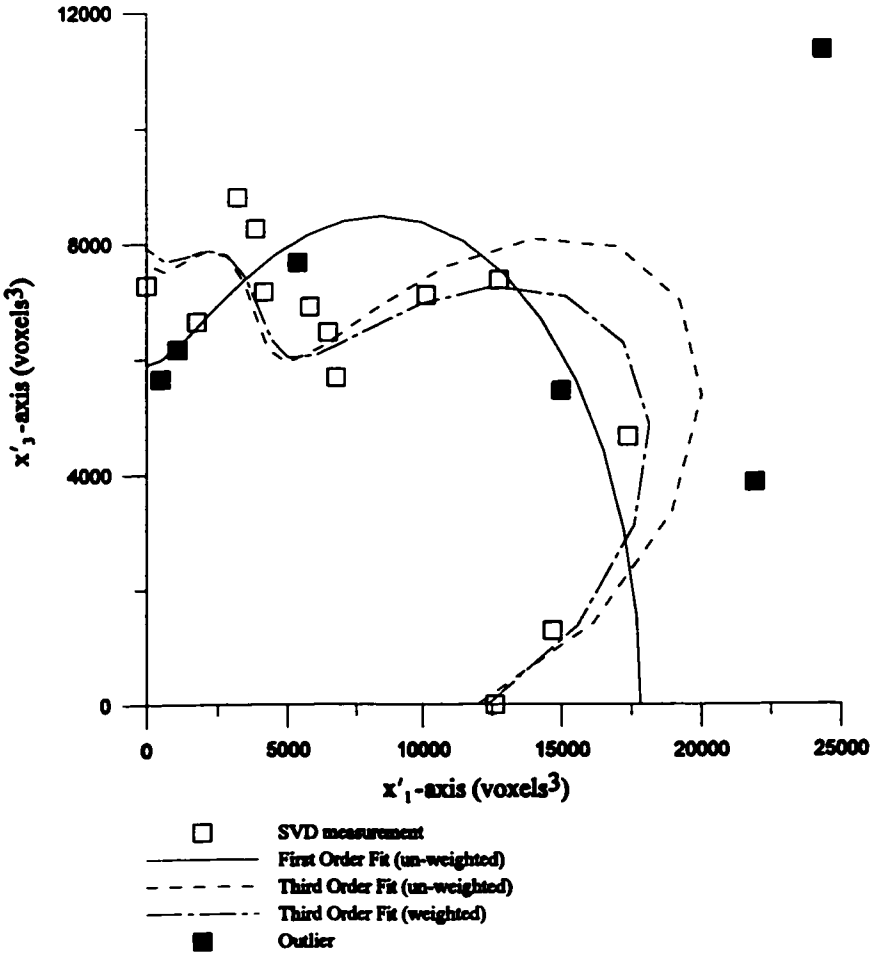

Figure 5.5: SVD measurements and fitting with the IRWNLLS algorithm.

In some instances, the relative improvement in fit may not be immediately apparent. This is particularly true for measurements of predominately isotropic structures. The effectiveness of the fit can be assessed by calculating the weighted sum of squared residuals, more commonly known as the chi-squared merit function (χ^2):

$$\chi^2(\mathbf{a}) = \sum_k w_k(y_k - \hat{y}_k(\mathbf{a}))^2 \equiv S(\mathbf{a}) \tag{5.22}$$

Figure 5.6 shows the results for increasing orders of fit normalized to that of χ^2 evaluated for a first order, non-weighted fit. As expected, in both series, increasing the order of fit also leads to a marked improvement in fit. The inclusion of weights calculated with Huber's influence function demonstrates, in general, a significant improvement in χ^2 for all orders of fit over that obtained without weights.

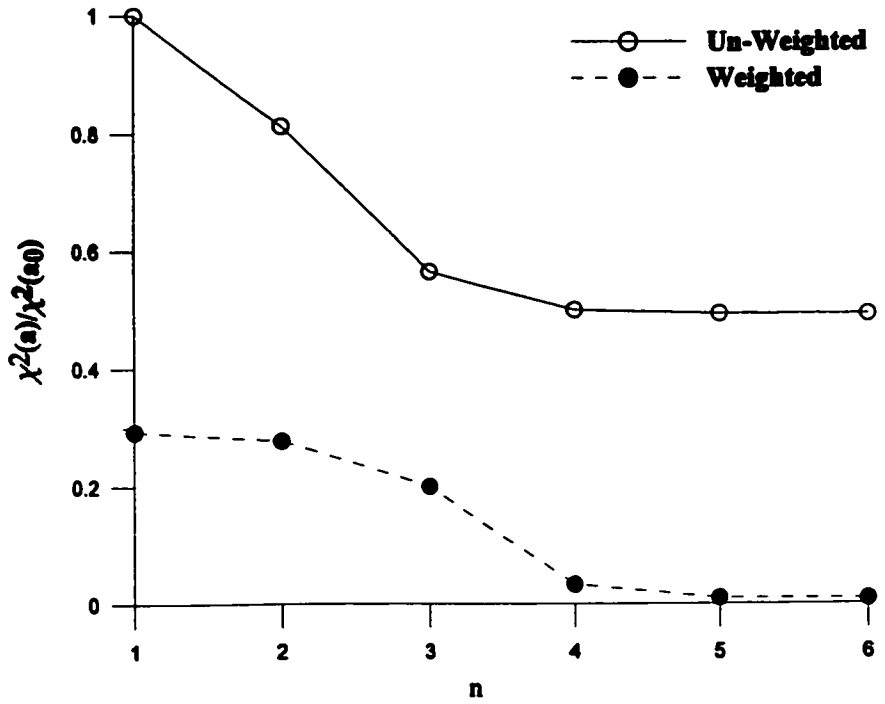

Figure 5.6: Order of fit, n, versus normalized χ^2: weighted and un-weighted IRWNLLS fits.

CHAPTER 6 Fabric Analysis of Trabecular Bone Images

In this chapter, fabric analyses of two micro-CT images of trabecular bone biopsies are conducted. The cadaveric samples, taken from the femoral neck, have similar porosity values but different micro-structural arrangements. Prior to the numerical analyses, section 6.1 provides a discussion on graphical presentation techniques for characterizing and identifying material symmetry information. The characteristics of the images are briefly outlined in section 6.2. Several computer generated renderings of the samples are presented and the positioning of the spherical volume of interest (VOI) adopted for the analyses is also graphically shown. Next, in section 6.3, the algorithms developed and verified in the preceding sections are applied to the images. A suitable grid spacing is established by comparing line array estimates with direct voxel counting measurements of volume fraction (VF). A brief investigation into the influence of sampling domain size and position is carried out in section 6.4. The chapter concludes in section 6.5 with some final remarks concerning fabric analysis of trabecular bone images.

6.1 Geometric Interpretation and Visualization

In general, plotting a distribution function directly as a radius from the origin along the direction of measure, as in

$$\mathbf{F}(\hat{\mathbf{v}}) = f(\hat{\mathbf{v}})(\hat{v}_1\,\hat{\mathbf{i}} + \hat{v}_2\,\hat{\mathbf{j}} + \hat{v}_3\,\hat{\mathbf{k}}) \tag{6.1}$$

produces an ellipsoid. The second order distribution function is defined, relative to the principal material triad, by the mean, C, and the three principal values of D_{ij} (i.e., $\lambda_1, \lambda_2, \lambda_3$). Expanding equation (2.3) or, equivalently, equation (2.8) with n = 1, gives

$$f(\hat{\mathbf{v}}) = C(1 + \lambda_1)\hat{v}_1^2 + C(1 + \lambda_2)\hat{v}_2^2 + C(1 + \lambda_3)\hat{v}_3^2 \tag{6.2}$$

The squared norm of the position vector for an ellipsoid is

$$\|\mathbf{r}(\hat{\mathbf{v}})\|^2 = a^2\hat{v}_1^2 + b^2\hat{v}_2^2 + c^2\hat{v}_3^2 \tag{6.3}$$

The following comparisons are evident:

$$\begin{aligned} C(1 + \lambda_1) &\equiv a^2 \\ C(1 + \lambda_2) &\equiv b^2 \\ C(1 + \lambda_3) &\equiv c^2 \end{aligned} \tag{6.4}$$

The traceless condition imposed in the definition of equation (2.3) implies that one of the semi-axes of the ellipsoid depends on the other two, i.e.:

$$\sum \lambda_k = 0 \rightarrow a^2 + b^2 + c^2 = 3C \tag{6.5}$$

An ellipsoid with semi-axes having lengths equal in magnitude to the eigenvalues of D_{ij} can be plotted in principal space with

$$\mathbf{F}'(\hat{\mathbf{v}}) = \sqrt{|f(\hat{\mathbf{e}}_1)|}\,\hat{v}_1\,\hat{\mathbf{e}}_1 + \sqrt{|f(\hat{\mathbf{e}}_2)|}\,\hat{v}_2\,\hat{\mathbf{e}}_2 + \sqrt{|f(\hat{\mathbf{e}}_3)|}\,\hat{v}_3\,\hat{\mathbf{e}}_3 \tag{6.6}$$

However, this representation is somewhat misleading in that the actual spatial distribution of data is not accurately reproduced. Furthermore, under certain viewing conditions, an ellipsoid viewed face-on appears like a sphere and therefore fails to present the anisotropy information unambiguously.

An alternative to visualizing symmetric second order tensors is to use an object which

is seen as a combination of a line, a disk, and a sphere, as advocated by Westin et al. (1999). The advantage to such an approach is that it presents not only directional information, but also qualitatively describes the degree of anisotropy. The line segment describes the major principal direction of the tensor and its length is proportional to the largest eigenvalue. The disk describes the plane spanned by the eigenvectors corresponding to the two largest eigenvalues. The sphere has a radius proportional to the smallest eigenvalue. The tensor A_{ij} (i.e., equation (2.5)) can be decomposed into a sum of components in the tensor basis $\{\mathbf{A}_l, \mathbf{A}_p, \mathbf{A}_s\}$;

$$\begin{aligned} \mathbf{A} &= \lambda_1 \hat{\mathbf{e}}_1 \hat{\mathbf{e}}_1^T + \lambda_2 \hat{\mathbf{e}}_2 \hat{\mathbf{e}}_2^T + \lambda_3 \hat{\mathbf{e}}_3 \hat{\mathbf{e}}_3^T \\ &= (\lambda_1 - \lambda_2)\mathbf{A}_l + (\lambda_2 - \lambda_3)\mathbf{A}_p + \lambda_3 \mathbf{A}_s \end{aligned} \tag{6.7}$$

where $\hat{\mathbf{e}}$'s and λ's are the eigenvectors and eigenvalues of $\mathbf{A}$ respectively, and the components of the tensor basis are defined as:

$$\begin{aligned} \mathbf{A}_l &= \hat{\mathbf{e}}_1 \hat{\mathbf{e}}_1^T \\ \mathbf{A}_p &= \hat{\mathbf{e}}_1 \hat{\mathbf{e}}_1^T + \hat{\mathbf{e}}_2 \hat{\mathbf{e}}_2^T \\ \mathbf{A}_s &= \hat{\mathbf{e}}_1 \hat{\mathbf{e}}_1^T + \hat{\mathbf{e}}_2 \hat{\mathbf{e}}_2^T + \hat{\mathbf{e}}_3 \hat{\mathbf{e}}_3^T \end{aligned} \tag{6.8}$$

The subscripts l, p, and s stand for 'line,' 'plane,' and 'sphere,' respectively.

A normalized set of tensor basis coordinates can be defined as:

$$\begin{gathered} c_l = \frac{\lambda_1 - \lambda_2}{\lambda_1} \quad ; \quad c_p = \frac{\lambda_2 - \lambda_3}{\lambda_1} \quad ; \quad c_s = \frac{\lambda_3}{\lambda_1} \\ c_l + c_p + c_s = 1 \quad \wedge \quad |\lambda_1| \geq |\lambda_2| \geq |\lambda_3| \end{gathered} \tag{6.9}$$

so that the degree of ansiotropy can be measured as the deviation from the spherical (isotropic) case:

$$DA = 1 - c_s = 1 - \frac{\lambda_3}{\lambda_1} \tag{6.10}$$

with magnitude dependent upon the descriptor. However, DA quantified in this manner is of limited value since it cannot distinguish between transversely isotropic and orthotropic symmetries. A more apt characterization of equation (6.10) would be 'departure from isotropy.' The relative magnitudes of the tensor basis coordinates can be interpreted in order to characterize an underlying structural symmetry, as summarized in table 6.1.

Symmetry Characterization	**Relative Tensor Basis Magnitudes**
isotropy	$c_s \approx 1 \wedge c_l \approx c_p \approx 0 \leftarrow \lambda_i \approx 1/3$
transverse isotropy	$c_p \approx 0 \leftarrow \lambda_1 \approx \lambda_2 > 1/3 \quad \vee$ $c_l \approx 0 \leftarrow \lambda_2 \approx \lambda_3 \leq 1/3$
orthotropy	$c_s < 1$; c_l, c_p: descriptor dependent

Table 6.1: Tensor basis characterization of symmetry.

Figure 6.1 shows a comparison between plotting SLD of the rotated ellipsoid image via equation (6.1) when $f(\hat{\mathbf{v}})$ is evaluated by equation (2.8) with n = 2, and by the composite shape on the left. The three component objects are plotted as ellipsoids with semi-axes scaled to a maximum of 1 according to the following scheme:

$$\begin{aligned} &\|\mathbf{r}_s(\hat{\mathbf{e}})\| = \lambda_3/\lambda_1 \\ &\|\mathbf{r}_p(\hat{\mathbf{e}}_{1,2})\| = \lambda_2/\lambda_1 \quad , \quad \|\mathbf{r}_p(\hat{\mathbf{e}}_3)\| = \bar{\lambda}/9 \quad , \quad \bar{\lambda} = \textstyle\sum \lambda_i/3 \\ &\|\mathbf{r}_l(\hat{\mathbf{e}}_1)\| = 1 \quad , \quad \|\mathbf{r}_l(\hat{\mathbf{e}}_{2,3})\| = \bar{\lambda}/9 \end{aligned} \tag{6.11}$$

where $\mathbf{r}_s$, $\mathbf{r}_p$, and $\mathbf{r}_l$ are the vector equations for the sphere, disk, and line objects, respectively. The value of 9 was chosen somewhat arbitrarily to produce the appearances of a line segment and a disc viz. the vector equation of an ellipsoid.

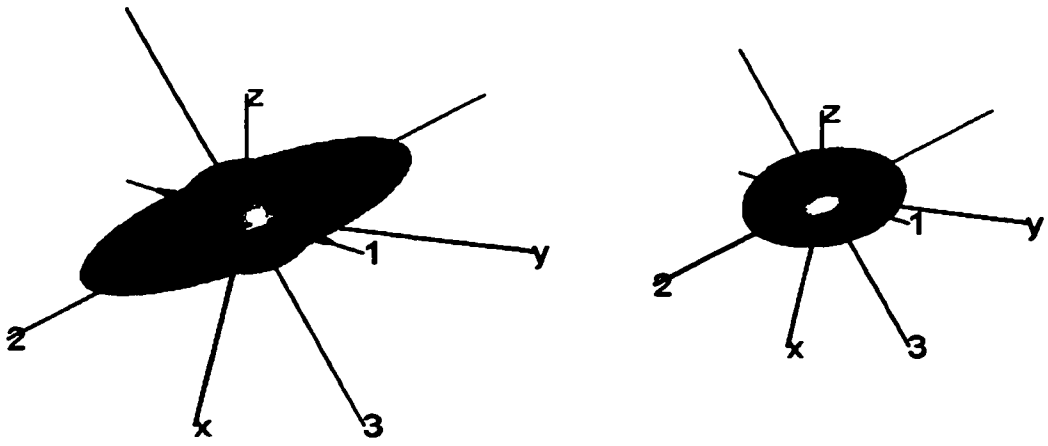

Figure 6.1: Composite shape plot of SLD and surface plotted from radial vectors: ellipsoid image.

Figure 6.2 is a composite polar plot of SLD, fit with n = 2, evaluated in the first quadrant of the three principal planes and demonstrates, that for this case, equation (6.1) does not necessarily plot as an ellipsoid. The purpose of such a plot is to give the reader a sense of the actual distribution of data. Here, $f(\hat{\mathbf{v}})$ is evaluated in the planes spanned by eigenvector pairs, $\{\hat{\mathbf{e}}_\alpha, \hat{\mathbf{e}}_\beta\}$, in the direction

$$\hat{\mathbf{v}} = [\hat{\mathbf{e}}_\alpha, \hat{\mathbf{e}}_\beta, \hat{\mathbf{e}}_\alpha \times \hat{\mathbf{e}}_\beta][\cos(\psi), \sin(\psi), 0]^T \; ; \; \psi \in [0, \pi/2] \tag{6.12}$$

wherein ψ is varied parametrically. The distribution function, obtained by the IRWNLLS fitting procedure, is plotted as a solid line while discrete points, obtained by measuring in a prescribed direction viz. equation (6.12), are shown as un-filled symbols.

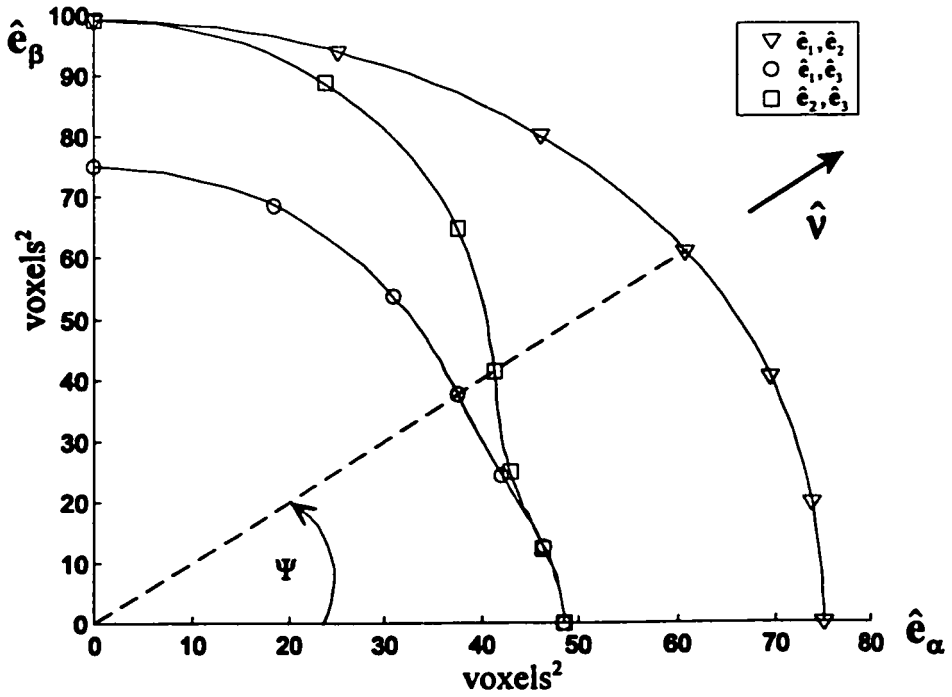

Figure 6.2: Composite radial plot of SLD evaluated in principal planes: ellipsoid image.

6.2 Trabecular Bone Samples

Two micro-CT images of cylindrical bone biopsies from the femoral neck were obtained in binarized form from Dr. Ralph Mueller (Orthopedic Biomechanics Laboratory, Beth Israel Deaconess Medical Center, Harvard Medical School). Table 6.2 summarizes the general image characteristics. The abbreviations BV/TV and DA refer to bone volume fraction and degree of anisotropy respectively. Here, DA is defined as the ratio of the maximum to minimum MIL eigenvalue, where the MIL tensor is defined as in Harrigan and Mann (1984). The details of the calculations and a Mathematica program to calculate DA are provided in Appendix B. The MIL measurements were obtained with the uniform line array algorithm (i.e., figure 3.16) with a spherical VOI; R_G = 135 voxels, $\mathbf{c}$ = {167,167,154}, a grid spacing

of 10 voxels, and without the use of the pattern matching algorithm. VF was determined via the direct voxel counting algorithm (i.e., figure 3.15) with the same spherical VOI. The results (in brackets) are in reasonable agreement with the (bone) VF and DA values provided by Dr. Mueller in both cases.

Identification	frx02_bvf-18_da-1-25.aim; femur_1	frx59_bvf-18_da-1-47.aim; femur_2
BV/TV (VF)	**18 % (17.7%)**	**18 % (17.5%)**
DA	1.25 (1.26)	1.47 (1.52)
Dimensions	336×336×310	336×336×310
Voxel size (isotropic)	28 μm	28 μm

Table 6.2: General image characteristics.

Figures 6.3 and 6.4 show the boundary projection of the spherical volume of interest overlaid on three average intensity projection images of the femur_1 and femur_2 images, respectively. The corresponding volume renderings were generated by ray casting along the plane normal direction starting at the center of the VOI. These images illustrate that for similar porosity values, the underlying structural arrangement of trabeculae can be significantly different. The femur_1 sample consists of a heterogeneous arrangement of both rod and small plate structures while the femur_2 sample exhibits larger plate structures with fewer rods.

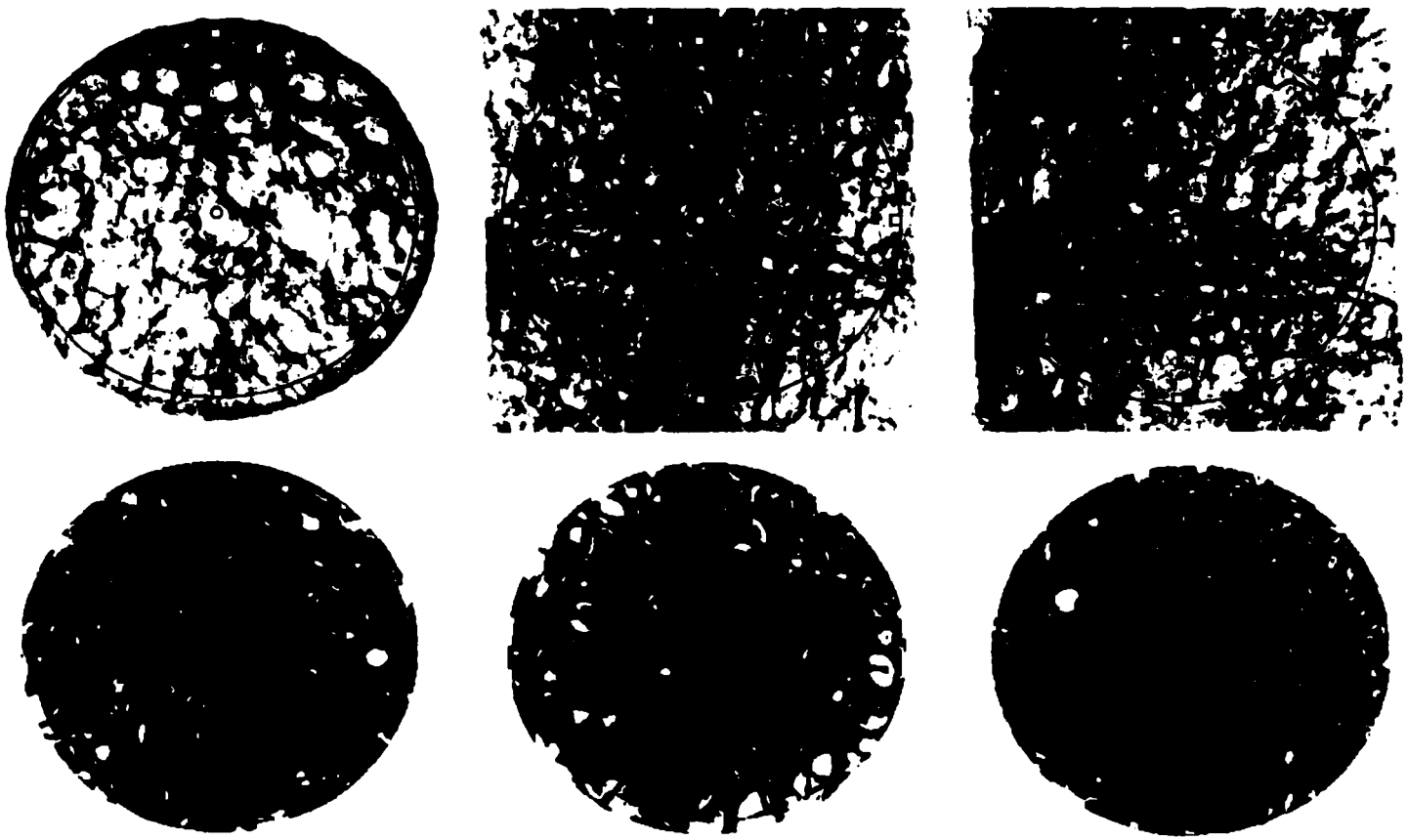

(a) x_1-x_2 (b) x_1-x_3 (c) x_2-x_3

Figure 6.3: VOI overlaid on average intensity projection images of femur_1 with volumetric rendering of VOI half space.

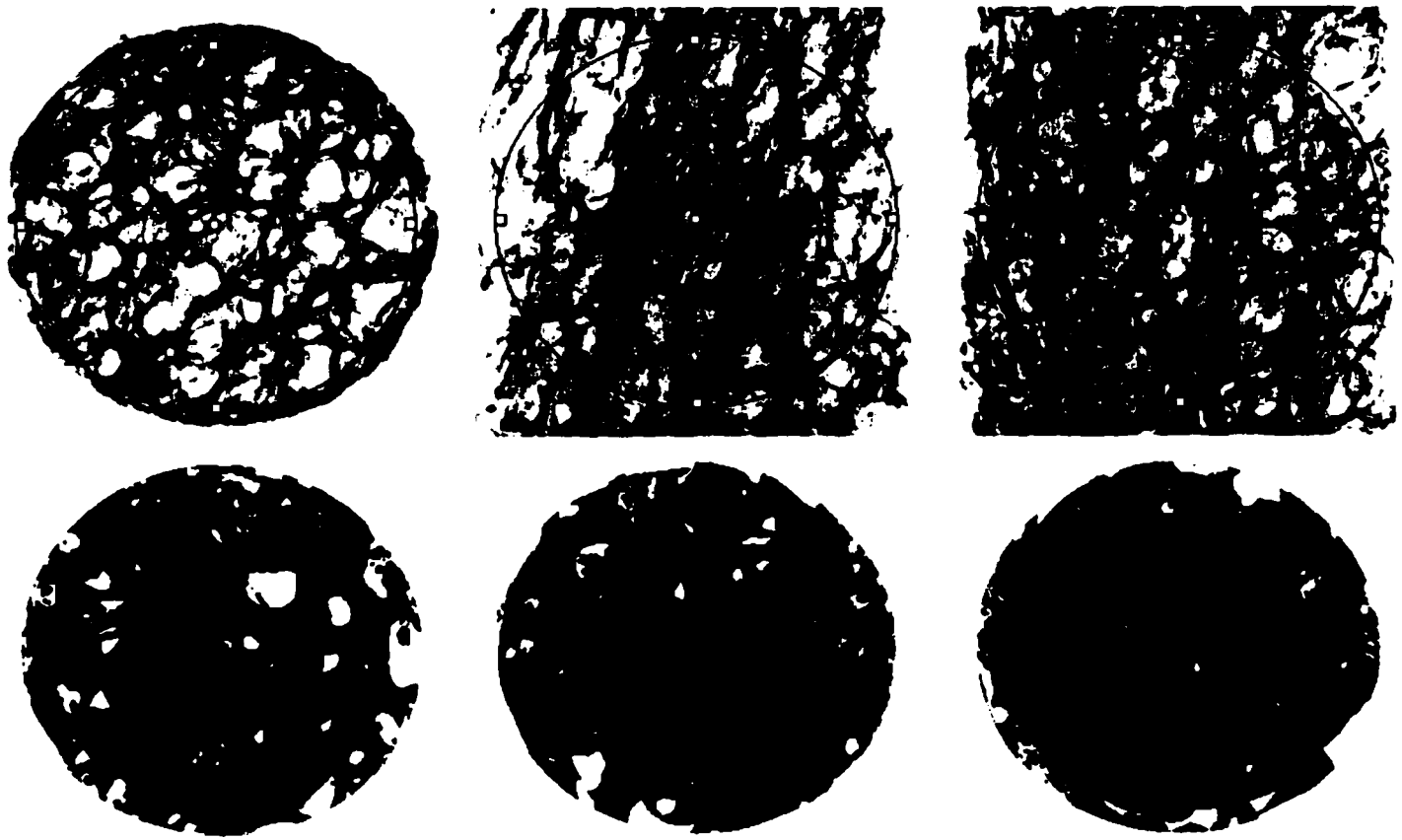

(a) x_1-x_2 (b) x_1-x_3 (c) x_2-x_3

Figure 6.4: VOI overlaid on average intensity projection images of femur_2 with volumetric rendering of VOI half space.

6.3 Fabric Analysis

Both images were subjected to a series of preliminary scans to determine the mean bone VF relative percent error over a range of grid spacings. The line grid algorithm of figure 3.11 was used to scan the images with 50 spiral points, pattern matching turned off, and grid spacings of $\delta = \{5, 10, \ldots, 30\}$ voxels. Figure 6.5 shows the mean relative percent error in VF over the range of grid spacings for both images. Based on these results, a grid spacing of 10 voxels was adopted for all of the subsequent descriptor measurements.

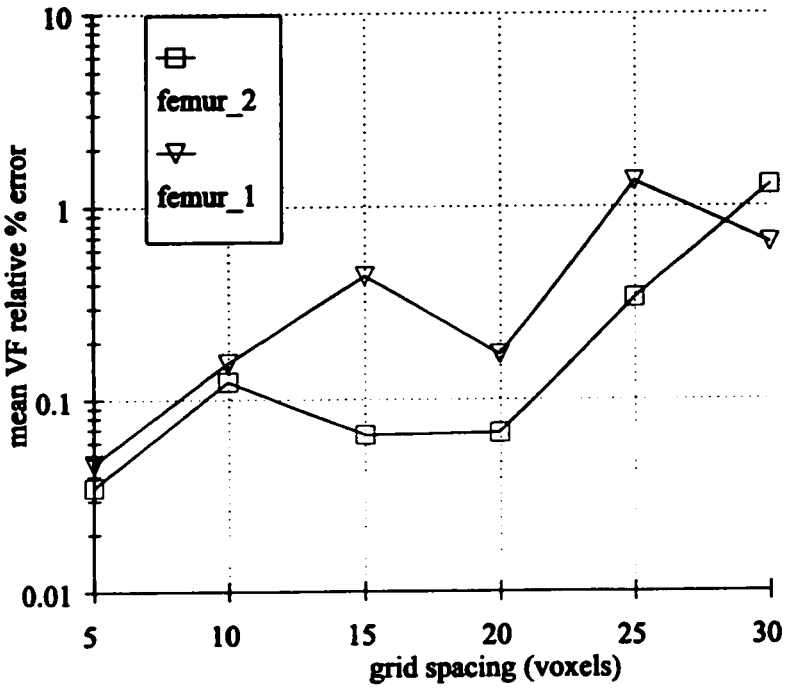

Figure 6.5: Grid spacing versus mean relative percent error in VF: femur_1 and femur_2 images.

6.3.1 Femur_1 Analysis

In this section, the femur_1 image is analyzed in detail for all descriptors. In all cases, 100 spiral points were used to scan the solid (bone) phase. The measurement data was fit to equation (2.8) with orders of fit; $n \in \{1, 2, ..., 5\}$, via the IRWNLLS algorithm. For each descriptor, the χ^2 merit function was evaluated. Values were subsequently normalized to one with the maximum χ^2 value, usually obtained with n = 1, for comparative evaluations. SLD and SVD measurement and first and second order distribution function plots are presented, which illustrate the influence of including higher order terms in equation (2.8). In addition, the form of micro-structural symmetry is assessed by the DA measure (i.e., equation (6.10)), and the tensor basis coordinates; c_l, c_p, and c_s, for all orders of fit. For the particular case of n = 2, composite shape plots are presented for line array descriptors AP, APS, MIL, SLD and SVD. It is further demonstrated that orientation detection is sensitive to order of fit, with stable results attained with most descriptors when n > 1.

Figures 6.6a to 6.6e are plots of order of fit versus normalized χ^2 for each descriptor. In the case of MIL, SLD, and SVD, additional series distinguished by 'alt' refer to the alternate calculation methods presented in section 2.4.8. Series distinguished by 'pm on' or 'pm off' refer to measurements obtained with and without pattern matching, respectively. For most descriptors, increasing the order of fit beyond two does not lead to a substantial improvement in fit. In the case of MIL, pattern matching significantly affects the measurement distribution and in turn the required order of fit to capture fluctuations in the data. On the other hand, for AP and APS descriptors, due to the averaging of measurements around the main sampling direction, pattern matching has less of an influence on the distribution of data and the improvement in fit is not significant for higher order representations.

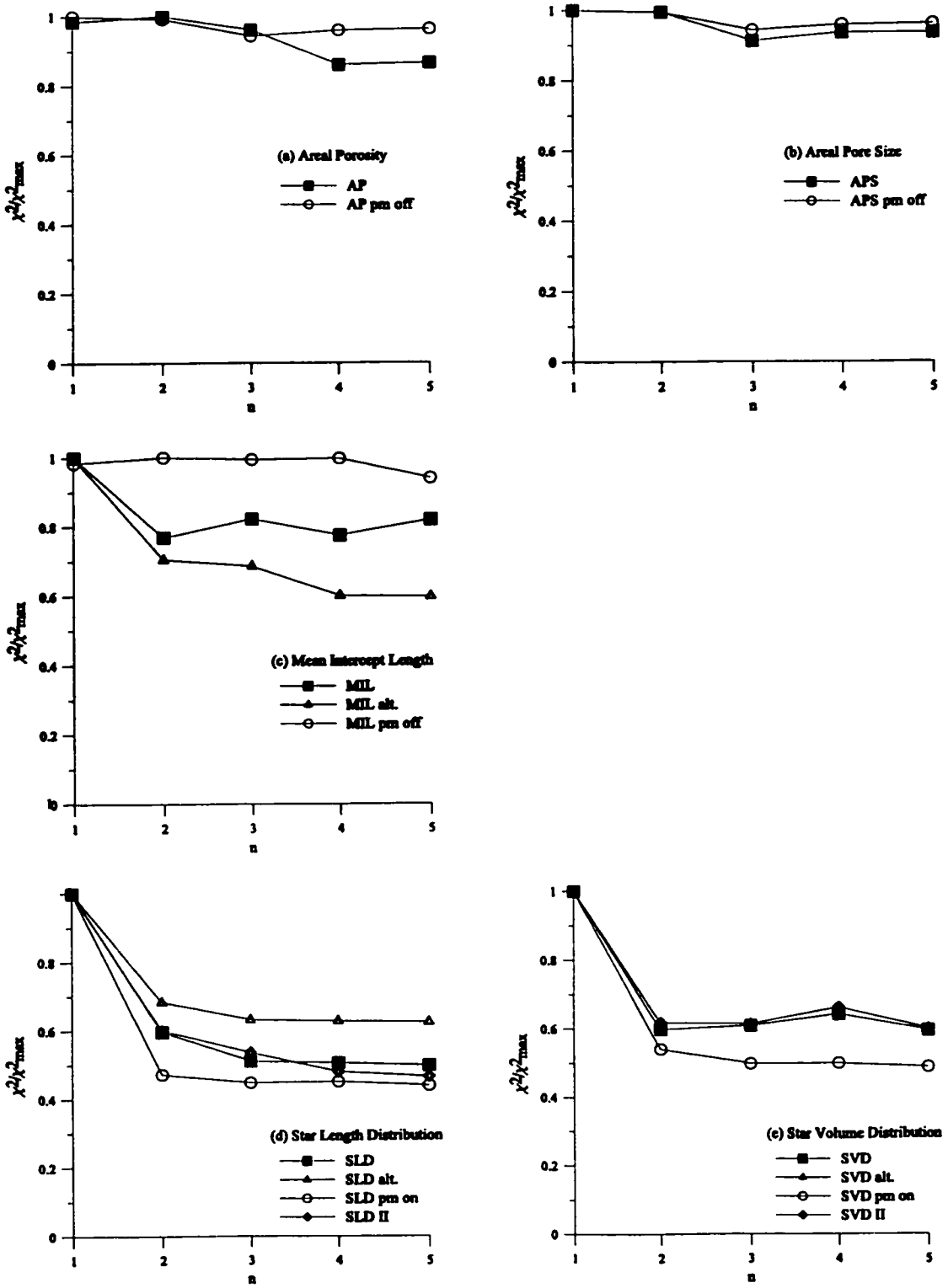

Figure 6.6: Order of fit, n, versus normalized χ^2; all descriptors: femur_1 image.

A series of best fit approximations, based on equation (2.8), versus measured values of SLD are presented in figures 6.7a to 6.7f. The first and second order distribution functions have been evaluated over 360 degrees in 10 degree increments (e.g., $\Delta\psi = 10°$ in equation (6.13)) within each of the three principal planes defined by the corresponding principal triads. These sampling directions were subsequently extracted and input into the line array code which was then run to obtain discrete SLD values for comparison with the continuous distributions. It should be noted that the orientations associated with the discrete measurement points are not the same for n =1 and n = 2, since the detected principal triad changes slightly for different orders of fit.

A noticeable improvement in fit is evident by comparing figures 6.7a with 6.7b, 6.7c with 6.7d, or 6.7e with 6.7f. Similar results are presented for the line array based SVD descriptor in figures 6.8a to 6.8f. Here, it is apparent that a second order fit is the minimum order necessary to capture the general trends in the distribution of data. However, due to the considerable amount of fluctuation in the measurements, it appears that SVD, when measured within the algorithm framework developed in this thesis, is not an adequate measure of fabric.

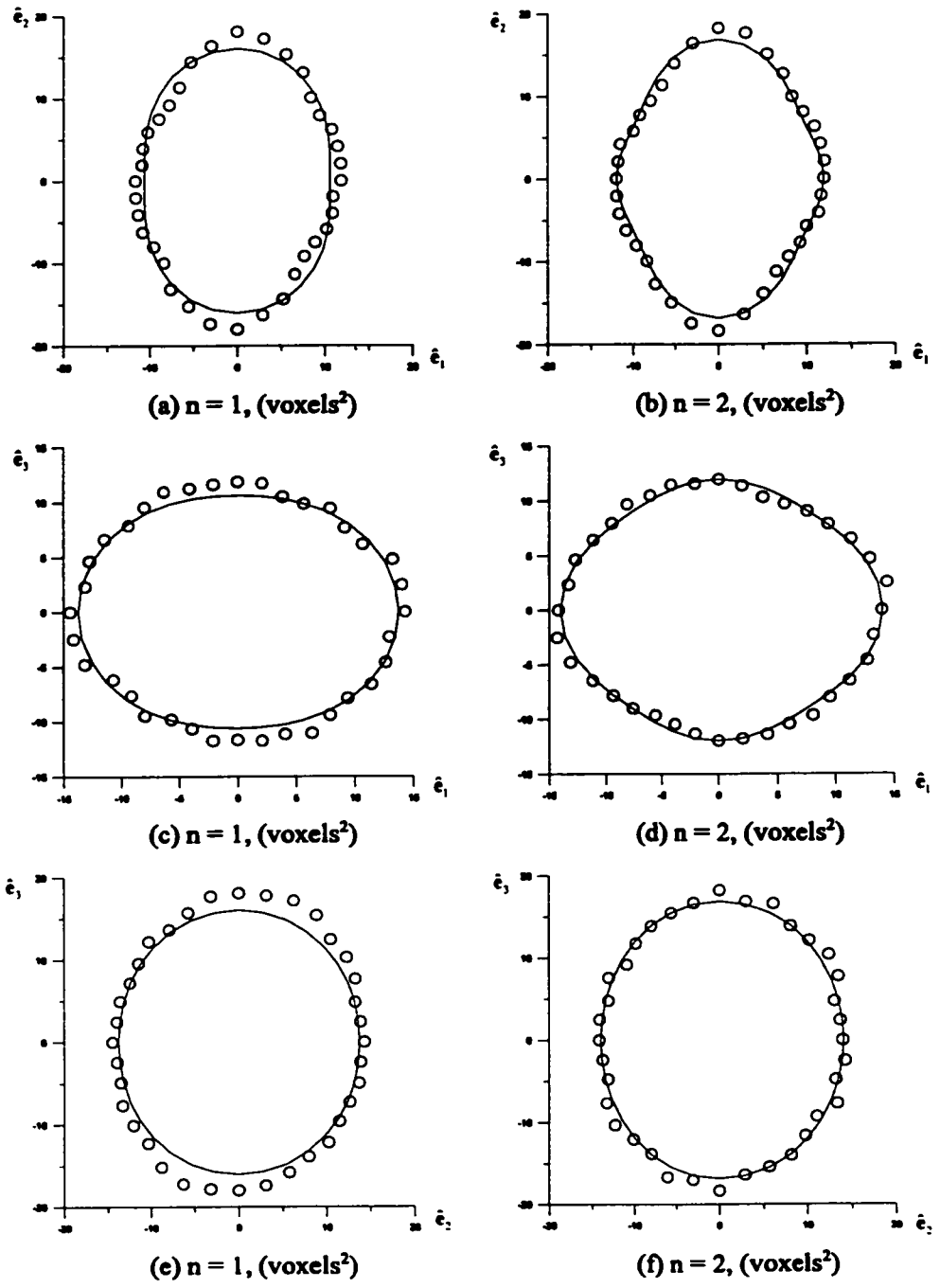

Figure 6.7: SLD evaluated in principal planes by fit '-' and raw measurements 'o'; first order (n = 1): (a), (c), (e); second order (n = 2): (b), (d), (f): femur_1 image.

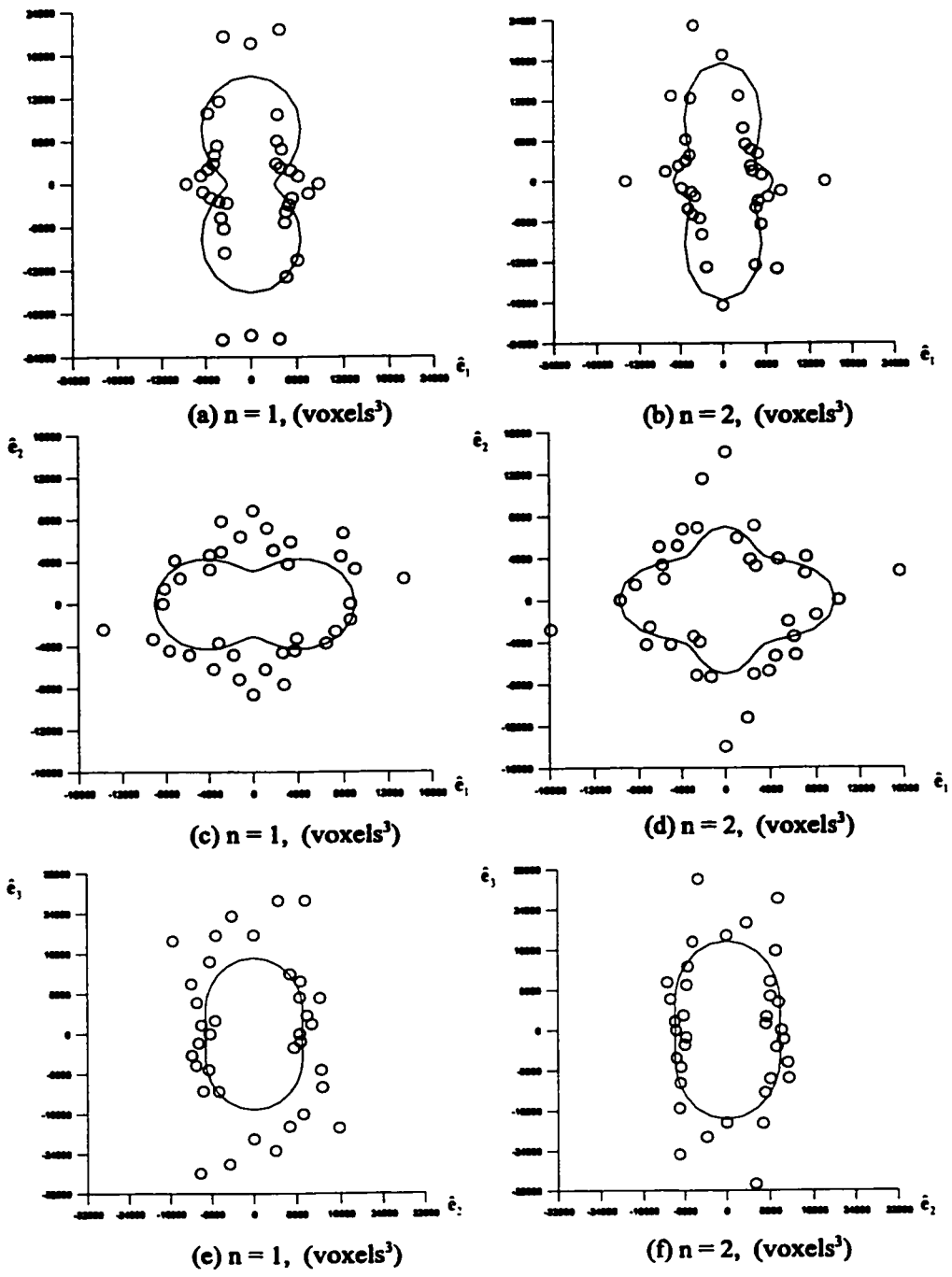

Figure 6.8: SVD evaluated in principal planes by fit '-' and raw measurements 'o'; first order (n = 1): (a), (c), (e); second order (n = 2): (b), (d), (f): femur_1 image.

Figures 6.9a to 6.9e show the influence of order of fit on DA. In general, the sensitivity to DA is descriptor dependent. In particular, and in light of similar results reported by Smit et al. (1998), the increase in sensitivity to anisotropy ranges from MIL to SVD with MIL < SLD < SVD. This result follows from the fact that intercept lengths are weighted with increasing order from MIL to SVD. It is not unexpected then that the AP and APS descriptors provide similar DA results as are obtained with MIL, since intercept lengths are also incorporated with order one. An interesting outcome is that for MIL ('pm on' and 'alt'), APS ('pm on'), SLD (all line array results), the DA response is fairly constant over different orders of fit. Conversely, the response of SVD is strongly influenced by the choice of order of fit and, after second order, the results are algorithm dependent. In the case of point grid derived measurements (i.e., 'II' series), for both SLD and SVD, decreasing the grid spacing from 10 to 5 voxels and thereby increasing the number of sampling points generates a smoother response, which approaches that obtained with the line array algorithm. Of additional interest is that line array based descriptors calculated via equations (2.24) to (2.26) are nearly identical to those obtained with the standard measurement specifications.

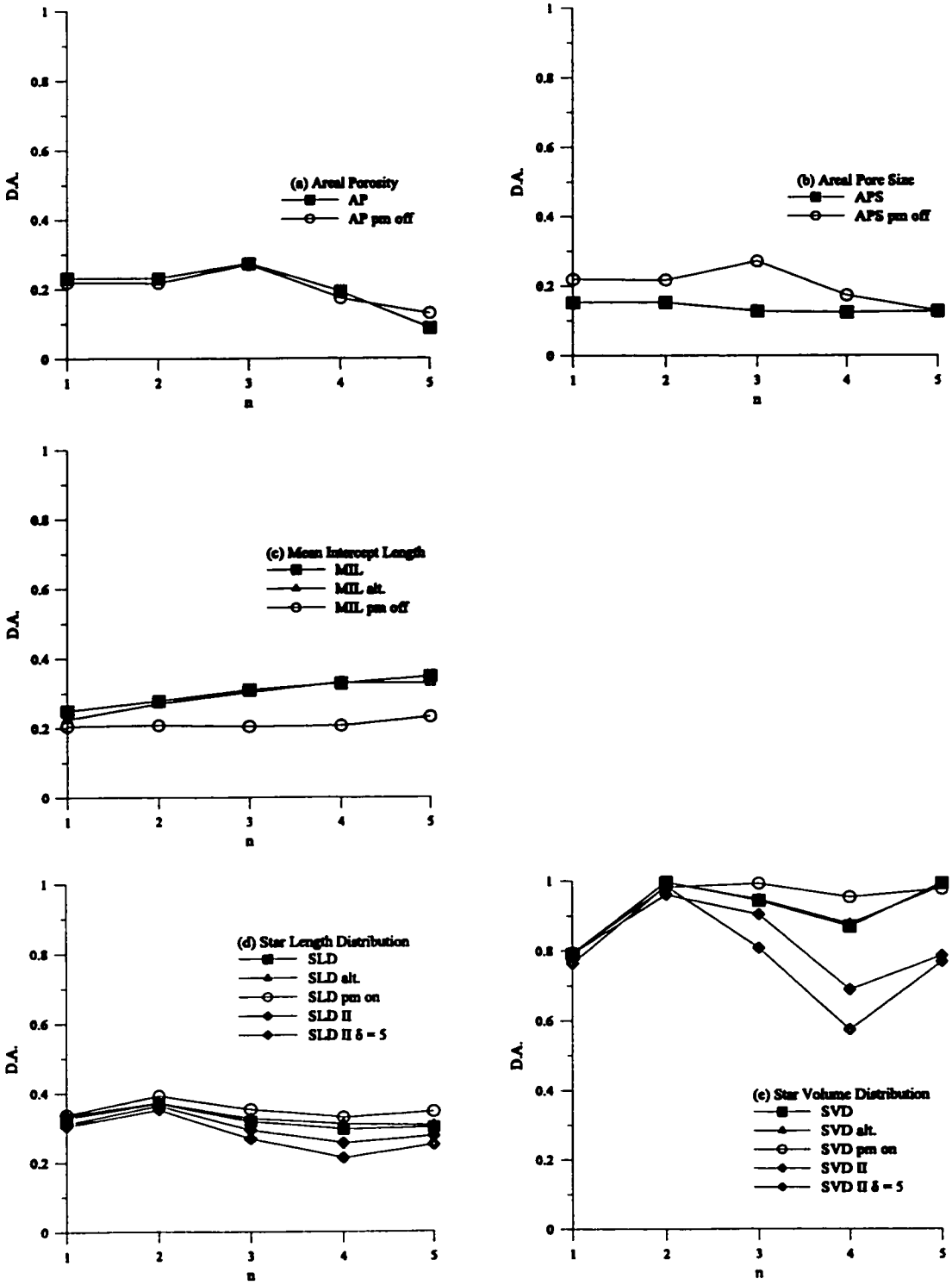

Figure 6.9: Order of fit, n, versus normalized degree of anisotropy, DA; all descriptors: femur_1 image.

A further question remains as to what the underlying structural symmetry actually is for this particular sample, since DA cannot differentiate this information. An additional series of plots of order of fit versus the tensor basis coordinates; c_s, c_p, and c_l, are presented in figures 6.10a to 6.10e for the line array descriptors evaluated with pattern matching on. For orders of fit greater than one the response is generally smooth, indicating that a second order fit sufficiently captures the anisotropy information. The sample is strongly anisotropic if evaluated by SVD, while a weaker form of anisotropy is detected by AP, APS, MIL and SLD descriptors.

It should be noted that interpretation of the anisotropy information by means of tensor basis coordinates (i.e., equation (6.9) or by DA (i.e., equation (6.10)) is only tentative in nature. The correlation with mechanical properties remains to be ascertained by a comprehensive experimental investigation, which is beyond the scope of the present research.

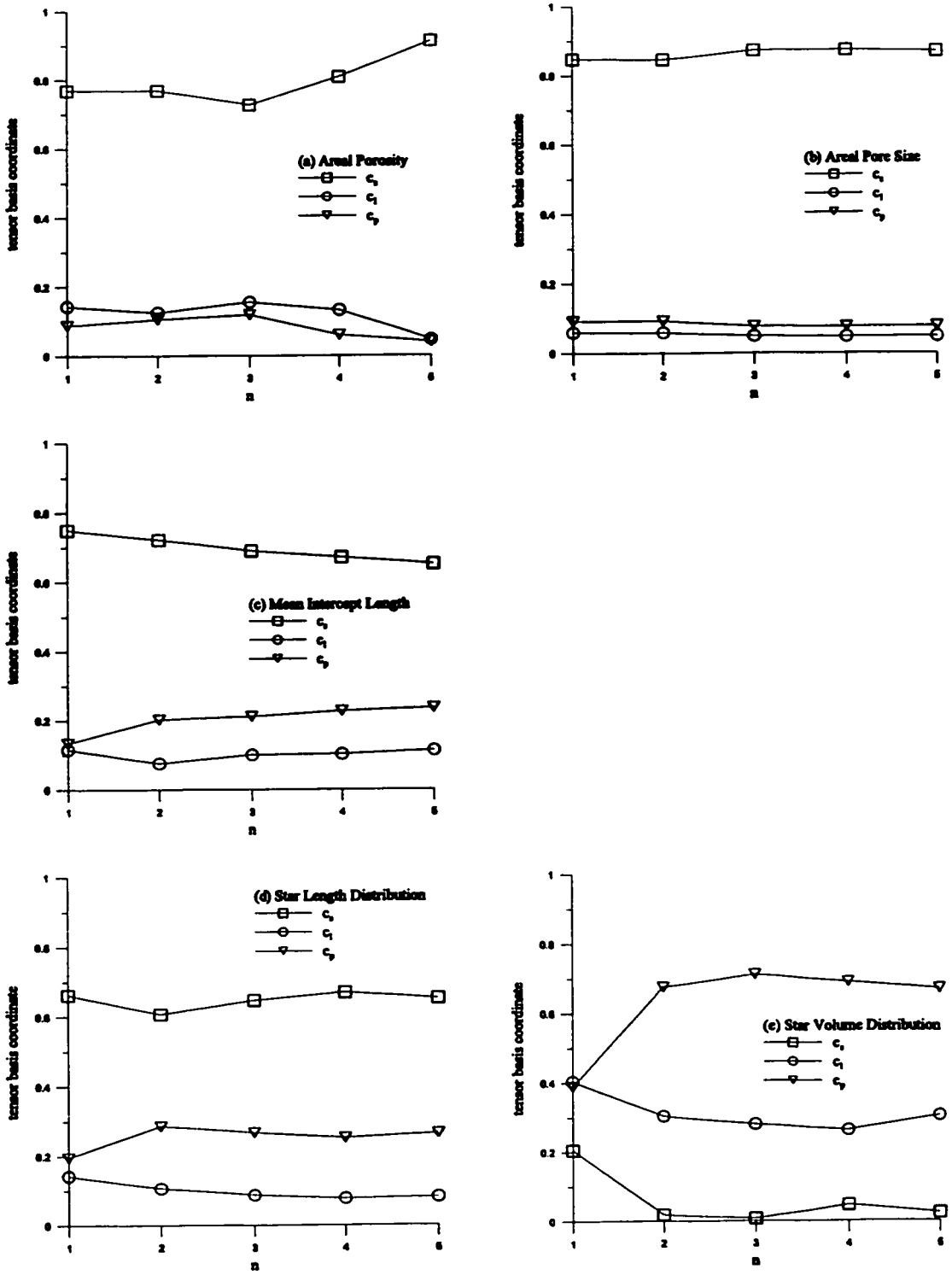

Figure 6.10: Order of fit, n, versus tensor basis coordinates; line array descriptors with pattern matching on: femur_1 image.

An alternative means of characterizing the symmetry information is presented in figures 6.11a to 6.11e using the composite plot approach discussed in section 6.1. The surfaces have been shaded to enhance the contrast between geometric entities. The composite shapes provide an immediate visual interpretation of the underlying symmetry via the relative magnitudes of the normalized principal descriptor values (i.e., equation (6.11)). Principal fabric triads and the orientation of the image frame of reference are also shown. The symmetry characterization is visually apparent with SVD displaying a strong anisotropy, as indicated by the absence of a spherical component, while the other descriptors indicate varying degrees of anisotropy. The dominant spherical component of both the AP and APS descriptors may be indicative of an isotropic sample. Verification of this will require a more in-depth statistical analysis to establish approximate standard errors and confidence regions for the tensor basis coordinates.

A comparison of the principal fabric orientations in figures 6.11a to 6.11e reveals that the AP descriptor may in fact be characterizing an isotropic symmetry, since the detected orientations differ significantly from those obtained by the other descriptors. Conversely, MIL, SLD and SVD detect approximately the same orientation configuration while APS, due to its definition, presents a similar configuration but in different order; i.e., direction 3 is the same as direction 1 identified by the other descriptors.

The sensitivity to orientation detection can be seen in figures 6.12a to 6.12c. Here, the principal fabric orientations are plotted in angular coordinates, θ and φ, for different orders of fit relative to the image frame of reference. The results for the AP descriptor are not included since the detected angles differed significantly from the other descriptors. The plots reveal that the detection of orientation is relatively stable for $n > 1$. This information may also be inferred from figures 6.10b to 6.10e since the tensor basis coordinates are defined by eigenvalues and also demonstrate numerical stability after a first order fit.

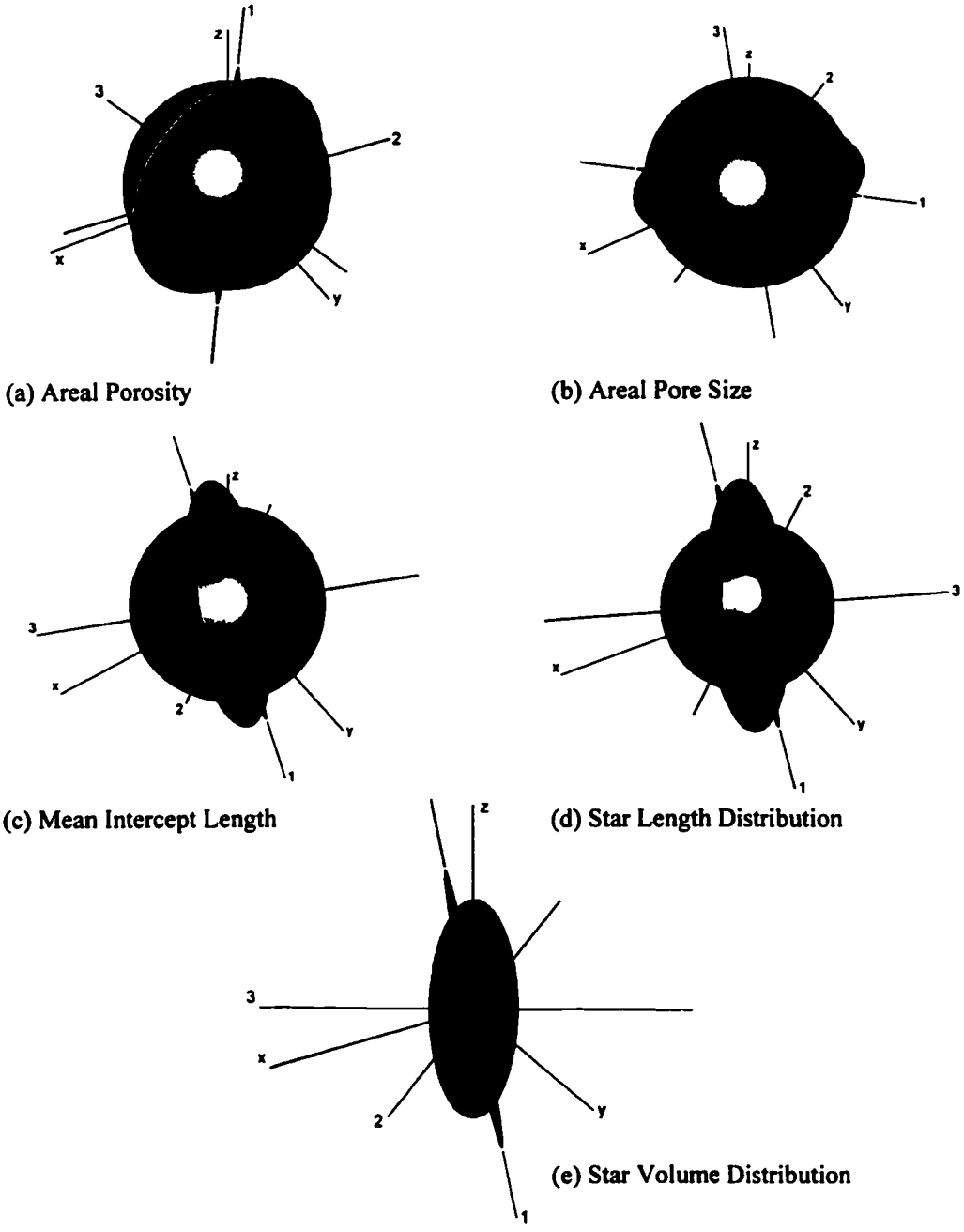

Figure 6.11: Composite shape plots with principal fabric orientations; n = 2, line array algorithms, pattern matching on: femur_1 image.

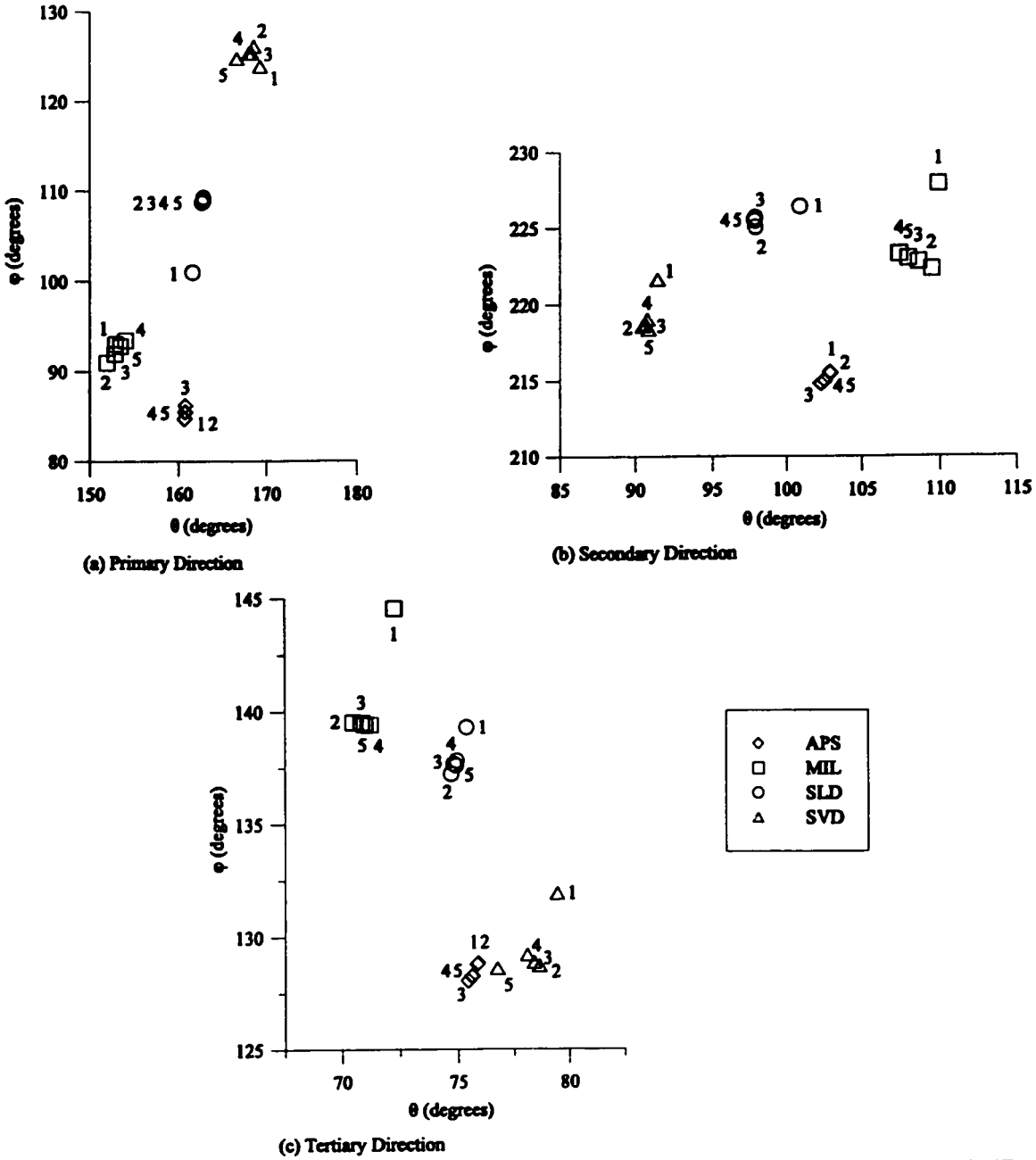

Figure 6.12: Principal fabric orientations of line array descriptors; APS, MIL, SLD, SVD for n $\in \{1, 2, \ldots, 5\}$: femur_1 image.

6.3.2 Femur_2 Analysis

In this section, the principal triad is identified and the degree of anisotropy of the femur_2 image is characterized in terms of the tensor basis coefficients. The descriptors: AP, APS, MIL, SLD, SVD were measured using the line array algorithms of section 3.3 with the following initial parameters: 100 spiral points orientations, δ = 10 voxels, pattern matching and boundary location algorithms employed. In some instances, the scanning was repeated with an increased sampling resolution.

Trends in order of fit versus normalized χ^2, shown in figure 6.13, were similar to those observed with the femur_1 image (see figure 6.6). The trend for SVD is seen to not level out after n = 2. Therefore, a second set of SVD measurements was obtained with 200 spiral points and δ = 5 voxels and the range of fit for all measures was increased so that $n \in \{1, 2, \ldots, 8\}$.

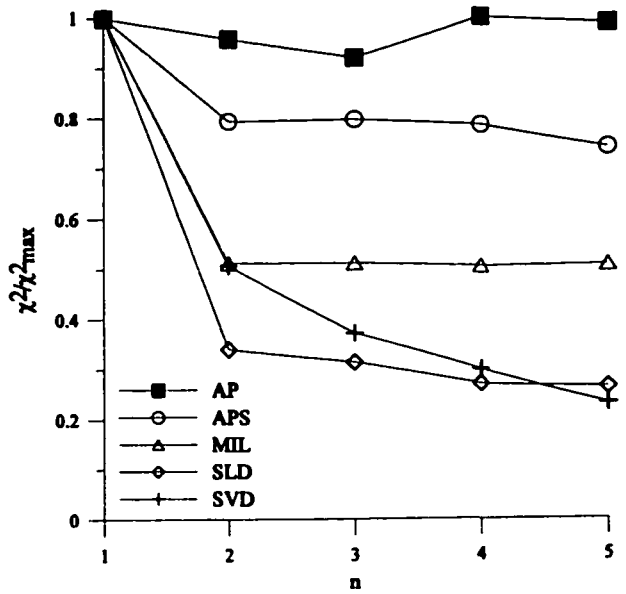

Figure 6.13: Order of fit, n, versus normalized χ^2;
line array based descriptors: femur_2 image.

Figures 6.14a to 6.14f show the tensor basis coordinates; c_l, c_p, and c_s, versus order of fit for the various descriptors. The SVD plot in figure 6.14f, distinguished by 'SVD 5 200,' corresponds to the measurements obtained with the increased sampling resolution. After a preliminary inspection of the results with $\delta = 10$ voxels it was decided that the AP measurements should also be repeated with an increased sampling resolution. The AP results in figure 6.14a were obtained with $\delta = 1$ voxel and 200 spiral point sampling orientations. A fairly smooth response is observed up to $n = 4$. On the other hand, the APS and MIL descriptors provide a smooth response for all $n > 1$, indicating that a second order fit is sufficient, as seen in figures 6.14b and 6.14c, respectively. A relatively stable response is obtained with $n > 2$ in the case of SLD in figure 6.14d, with the exception of the data corresponding to $n = 4$. The SVD results presented in figure 6.14e are erratic while those in figure 6.14f provide a reasonably stable response for $3 < n < 8$. Clearly, for this particular image and descriptor, a higher order of fit and an increase in sampling resolution were required.

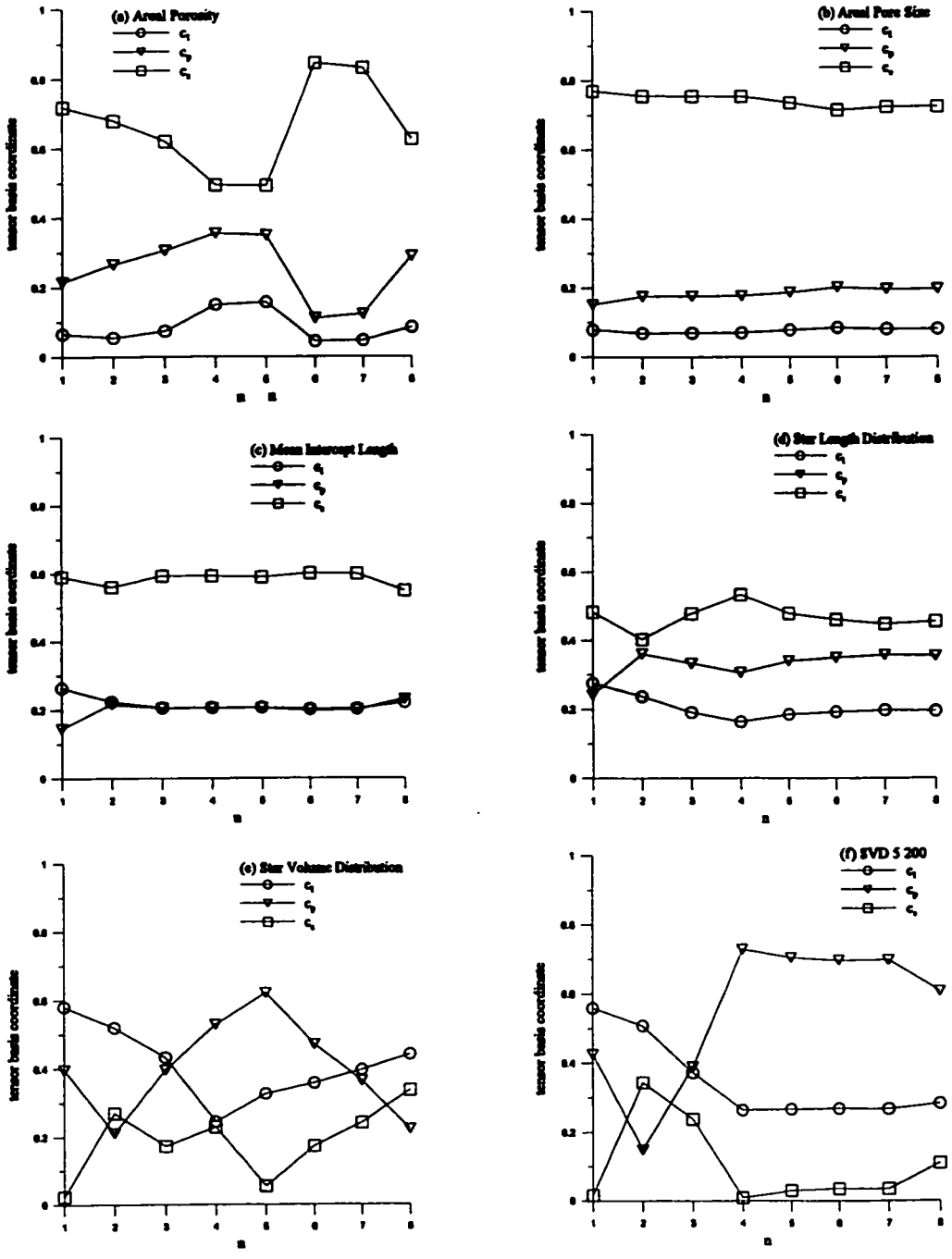

Figure 6.14: Order of fit, n, versus tensor basis coordinates: line array descriptors: femur_2 image.

The anisotropy information is presented next in a series of composite shape plots, shown in figure 6.15. The symmetry results are qualitatively similar to those obtained with the femur_1 image. In particular, the detected degree of anisotropy follows a similar trend: APS < AP < MIL < SLD < SVD. The detected principal triads are also shown and appear to be in reasonable agreement between descriptors.

Finally, the detected orientation triad is quantitatively assessed under different orders of fit for the descriptors APS, MIL, SLD, and SVD (i.e., 'SVD 5 200' series). The AP orientation results revealed a significantly different principal triad and are not presented here. Figures 6.16a to 6.16c show the principal fabric orientations plotted in angular coordinates for orders of fit . The primary and tertiary directions have been swapped in the case of APS for comparative evaluation with the other descriptors. The original SVD results were nearly identical to those obtained with the finer sampling resolution, and are therefore not shown. In the case of APS and MIL descriptors, a stable configuration is obtained after a first order fit while for SVD, good results are obtained with $n > 2$. SLD provides a reasonably stable configuration in the detected triad over the entire range of n.

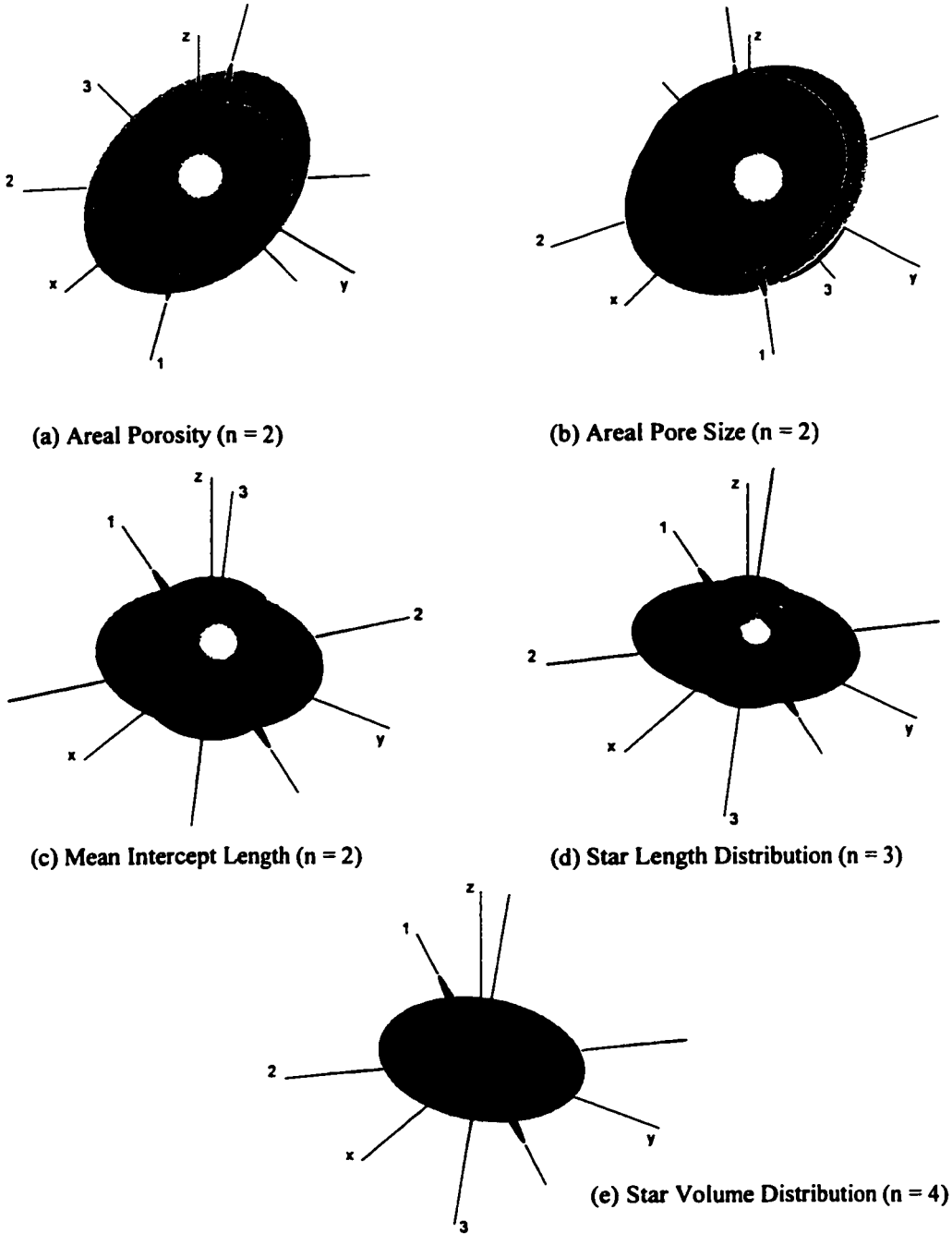

Figure 6.15: Composite shape plots with principal fabric orientations; line array algorithms: femur_2 image.

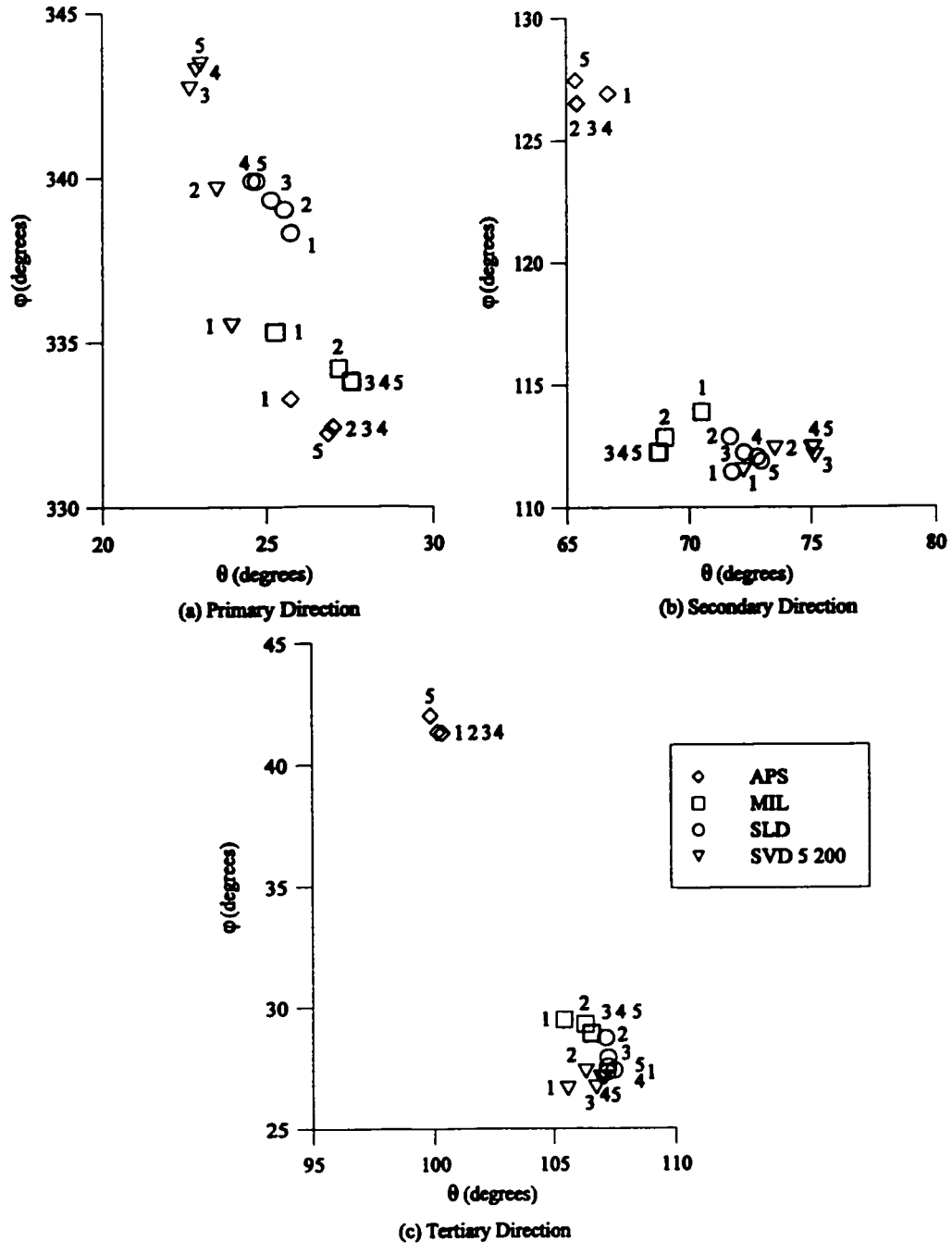

Figure 6.16: Principal fabric orientations for n ∈ {1, 2, ..., 5}, APS, MIL, SLD, SVD: femur_2 image.

6.4 Size Effect

An important aspect of bone fabric analysis is the notion of sample homogeneity. A question that immediately arises is: what influence does the size of the sampling domain have on the fabric results? To assess the impact of size effect, the APS measure was selected to analyze the two images for orientation and tensor basis characterization of anisotropy. The same original spherical VOI's were used, but with radii at 100%, 75%, and 50% of the original $R_G = 135$ voxels. The scanning parameters included a grid spacing of $\delta = 10$ voxels and use of the pattern matching and boundary detection algorithms. Equation (2.8) was fit to the measurements using the IRWNLLS algorithm for orders of fit: $n \in \{1, 2, ..., 5\}$. Eigenvalue analyses of the tensor, A_{ij}, corresponding to the different orders of fit, were performed and the principal triads and tensor basis coordinates were obtained.

The results for the femur_2 image with $R_G' = 135$, $R_G' = 101$, and $R_G' = 68$ voxels are presented in figures 6.17a, 6.17b, and 6.17c, respectively. The results do not show a significant change in the tensor basis coordinate trends, thereby indicating that, for the specific sample analyzed, the bone fabric is relatively homogeneous. Similar results were observed with the femur_1 image.

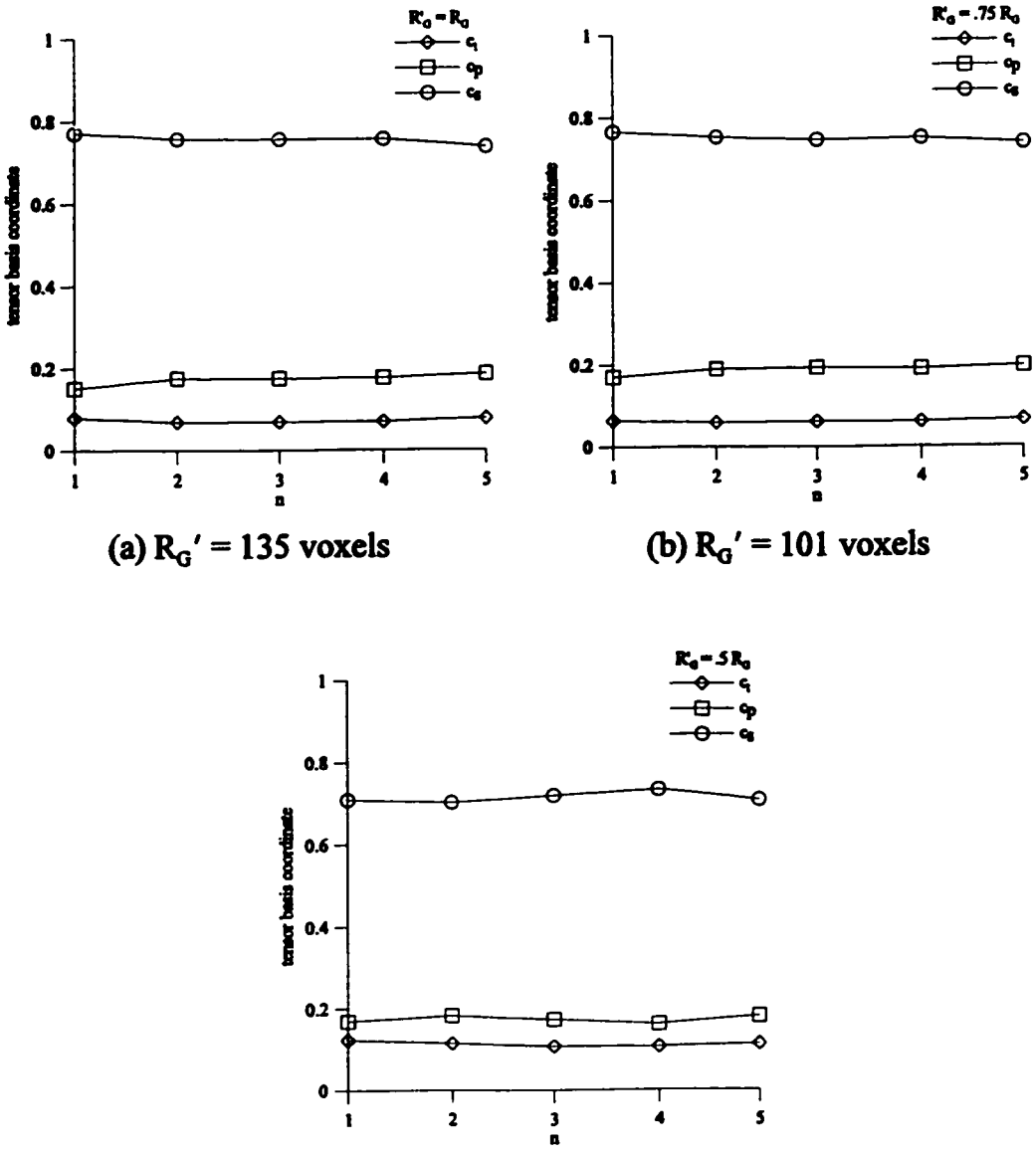

(a) $R_G' = 135$ voxels

(b) $R_G' = 101$ voxels

(c) $R_G' = 68$ voxels

Figure 6.17: Order of fit, n, versus tensor basis coordinates for femur_2 image: APS descriptor, $R_G' = 135, 101, 68$ voxels.

A further demonstration of the homogeneity of the sample is assessed by the detected principal triads for different VOI sizes and positions. Here, the spherical VOI was positioned within the image in the locations with the following centroid positions: location 'A' corresponds to the original central position, while locations 'B' and 'C' correspond to positions near the bottom and near the top of the 3D image, respectively. Table 6.3 below provides a summary of the VOI sizes, labels and centroid coordinates with respect to the image frame of reference. The series labels correspond to the data points shown next in figure 6.18, where the principal triads evaluated from a second order fit are plotted for the different VOI's in terms of the spherical angles: θ and φ.

Series Label	R_G' (voxels)	**Centroid Coordinates**
1 A	135	{167, 167, 154}
.75 A	101	
.5 A	68	
.5 B	68	{159, 96, 240}
.5 C	68	{240, 190, 72}

Table 6.3: Labeling key for figure 6.16; VOI sizes and positions: femur_2 image.

The plot shows that, for this image, the principal triad does not change significantly for different sizes of sampling domain, as seen in the 'A' series. Furthermore, the principal triad is seen to remain fairly constant for a smaller VOI scanned at different positions within the larger image volume, as seen in the '.5 A,' '.5 B,' and '.5 C' series of points.

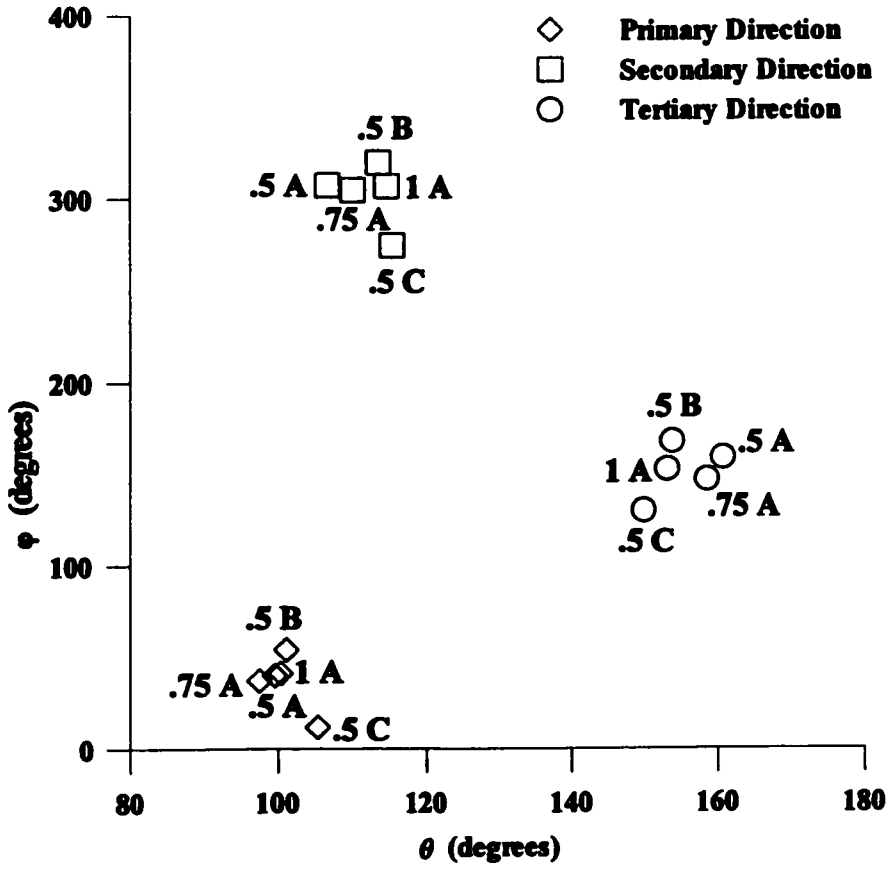

Figure 6.18: Principal fabric orientations, n = 2, APS descriptor evaluated in three locations of femur_2 image: R_G' = 135, 101, 68 voxels.

6.5 Final Remarks

A variety of ways of characterizing anisotropy information has been presented over the course of the analyses discussed in section 6.3. From the preceding discussions, it is apparent that caution must be exercised when conducting fabric analyses. It is recommended that a range of order of fit be tried and assessed by a normalized goodness of fit measure,

such as the χ^2 merit function. In general, the range of order of fit for which no significant further reduction in χ^2 is observed (i.e., generally for $n > 1$) tends to provide stable eigenvalues and principal fabric orientations. In the case of the trabecular bone images considered here, a second order of fit is sufficient to produce stable orientation information for most descriptors. A characterization of the micro-structural symmetry can be assessed via tensor basis coordinate plots. In cases where an unstable response is observed, as was seen in the femur_2 image with SVD, an increase in the sampling resolution should be applied and the resulting fabric measurements re-analyzed. Once a suitable fit to the data is chosen, composite shape plotting provides an unambiguous graphical representation of both the micro-structural symmetry and the detected principal triad.

The results of the analyses in this chapter suggest that some descriptors perform better than others in terms of detecting material fabric. SVD, as developed in this thesis, was shown to be somewhat inadequate as a measure of material fabric. In particular, SVD appears to overestimate the symmetry information and, as shown in the principal plane plots in figure 6.8, is not as numerically well behaved when compared with the SLD results presented in figure 6.7. The departure between data and fit is likely a result of the magnification of errors in intercept length since the measurement values are raised to powers of three and four in the point grid and line array approaches respectively. However, the accuracy of detection of principal orientations by SVD is on par with that of the APS, MIL, and SLD descriptors. Interestingly, the APS descriptor consistently generated the smoothest detection response of the various descriptors, and should be investigated further with a wider variety of bone architectures. The AP descriptor results, with regard to detected symmetry, are somewhat inconclusive at this stage without additional standard deviation estimates in the tensor basis coordinates. In general, a comprehensive mechanical testing program should be carried out to assess the correlation of different measures of fabric with mechanical properties.

An additional component of fabric analyses which deserves further attention, is the aspect of size effect. In section 6.4 it was shown, explicitly for the femur_2 image, that through an investigation of fabric properties evaluated with different sized VOI's, the homogeneity of the sample may be assessed. With other bone samples, wherein high porosity gradients occur, the influence of size on fabric analysis results may be more pronounced. The significance of size effect and, hence, homogeneity is important in the context of discretization of larger bone structures within FE analyses that incorporate fabric information.

CHAPTER 7 Modelling of Mechanical Behaviour of Bone

In this chapter, a numerical framework is presented for the constitutive and geometric modelling of whole bone entities. The mathematical details of a fabric-dependent constitutive law and failure criterion for bone are provided in section 7.1. The general discussion is similar to that reported in an earlier work, Pietruszczak et al. (1999), with slight modifications to maintain the consistency with the information on fabric tensors presented in chapter 2. In addition, the definition of the 'loading direction' has been modified in light of new research presented in Pietruszczak and Mroz (2001). The proposed material model is then applied within a numerical analysis of failure in the proximal femur. Here, static elastic analyses are performed and the resulting stress fields are verified for plastic admissibility of the failure criterion. Attainment of the criterion and subsequent behaviour of the bone material is considered to be brittle failure. Estimates of the orthotropic elastic properties are derived, based on typical values presented in the literature, in section 7.2. Derivation of the finite element model which incorporates geometry, porosity and density information from a sequence of CT images is discussed in section 7.3, while the boundary and loading conditions are discussed next in section 7.4. An analysis of the failure simulations, presented in section 7.5, pertain to those of a healthy and a simulated osteoporotic femur. In particular, the risk of failure is assessed in terms of the distribution of a suitably chosen scalar parameter.

7.1 Mathematical Formulation of Anisotropic Failure Criterion

The purpose of this section is to present the mathematical details of the constitutive relation and failure criterion which can be incorporated within FE analyses of bones in

general. The mathematical definitions of fabric tensors, their use in quantifying material micro-structure, and the details of their identification from representative bone samples have been discussed in chapters 2 through 6.

Bone material has a heterogeneous architecture and displays strong anisotropic properties. In order to describe its mechanical characteristics, it is essential to introduce some measure of material micro-structure. The formulation presented here employs the concept of areal porosity, defined previously in section 2.4.7, which is the areal fraction of voids on a plane passing through a material point. In general, this form of 'directional porosity' is equal to its scalar equivalent only when voids are uniformly distributed throughout the solid phase.

As was noted in chapter 2, the distribution of areal porosity can be expressed as a scalar-valued function defined over a unit sphere. For illustration purposes, one may consider the first order form of equation (2.8) and define a particular distribution function:

$$\bar{\eta}(v_i) \approx \eta(1 + D_{ij} v_i v_j) \tag{7.1}$$

In equation (7.1), η is the average porosity, v_i specifies the orientation relative to a fixed Cartesian coordinate system and D_{ij} is a symmetric traceless tensor, which describes the bias in the distribution of voids. For an isotropic material D_{ij} vanishes, whereas a smooth orthogonal anisotropy is represented by three distinct eigenvalues of D_{ij}. The representation (7.1) may also be expressed as

$$\bar{\eta}(v_i) \approx 3\eta A_{ij} v_i v_j \quad ; \quad A_{ij} = \frac{1}{3}(\delta_{ij} + D_{ij}) \rightarrow A_{ii} = 1 \tag{7.2}$$

where A_{ij} may be referred to as a fabric tensor.

The basic hypothesis underlying the failure criterion is that there exist a function F of the stress state σ_{ij} and the fabric A_{ij} such that if the ultimate state of the material is reached,

the value of this function is constant, say zero

$$F(\sigma_{ij}, A_{ij}, \eta) = 0 \tag{7.3}$$

Since the anisotropy of fabric is fully described by A_{ij}, F must be an isotropic function of both σ_{ij} and A_{ij}

$$F(\sigma_{ij}, A_{ij}, \eta) = F(T_{ip}T_{jq}\sigma_{pq}, T_{ip}T_{jq}A_{pq}, \eta) \tag{7.4}$$

where T_{ij} is the transformation tensor. A general representation of F may be obtained by expanding this function in a polynomial in the components of σ_{ij}. Cowin (1986) has developed a simple quadratic approximation

$$F = G_{ij}\sigma_{ij} + B_{ijkl}\sigma_{ij}\sigma_{kl} = \text{const.} \tag{7.5}$$

where

$$\begin{aligned} G_{ij} &= g_1\delta_{ij} + g_2 A_{ij} + g_3 A_{im}A_{mj} \\ B_{ijkl} &= f_1\delta_{ij}\delta_{kl} + f_2(A_{ij}\delta_{kl} + \delta_{ij}A_{kl}) + f_3(\delta_{ij}A_{kq}A_{ql} + \delta_{kl}A_{iq}A_{qj}) \\ &\quad + f_4 A_{ij}A_{kl} + f_5(A_{ij}A_{kq}A_{ql} + A_{is}A_{sj}A_{kl}) + f_6 A_{is}A_{sj}A_{kq}A_{ql} \\ &\quad + f_7(\delta_{ki}\delta_{lj} + \delta_{li}\delta_{kj}) + f_8(A_{ik}\delta_{lj} + A_{kj}\delta_{li} + A_{il}\delta_{kj} + A_{lj}\delta_{ki}) \\ &\quad + f_9(A_{ir}A_{rk}\delta_{lj} + A_{kr}A_{rj}\delta_{li} + A_{ir}A_{rl}\delta_{kj} + A_{lr}A_{rj}\delta_{ik}) \end{aligned}$$

and g's and f's are scalar valued functions of the basic invariants of A_{ij} and the average porosity. The representation above stems from general representation theorems for tensor-values functions developed for example in Boehler (1987).

There are apparent difficulties associated with approximation (7.5). Firstly, an extensive experimental program is required to identify the twelve functions of the material fabric. Secondly, it is known that the behaviour of porous materials is sensitive to the third stress invariant, so that the approximation (7.5), as well as other commonly used criteria (e.g., Tsai and Wu, 1971), may be quite inadequate to describe the conditions at failure.

In order to overcome the difficulties mentioned above, an alternative to representation

(7.3) is employed here, following a general approach advocated by Pietruszczak (1997). In particular, it is postulated that the functional form of the failure criterion incorporates directly $\bar{\eta}(v_i)$, equation (7.1), so that

$$F = F\left(\sigma_{ij}, \bar{\eta}(\hat{I}_i)\right) = 0 \tag{7.6}$$

Here, the function $\bar{\eta}$ is evaluated in the unit 'loading direction' $\hat{I}_i$, which is defined with respect to the principal material triad. The magnitudes of the traction components acting on the planes normal to the axes of orthotropy are

$$\begin{aligned} L_1 &= \left(\sigma_{11}^2 + \sigma_{12}^2 + \sigma_{13}^2\right)^{1/2} \quad ; \quad L_2 = \left(\sigma_{12}^2 + \sigma_{22}^2 + \sigma_{23}^2\right)^{1/2} \\ L_3 &= \left(\sigma_{13}^2 + \sigma_{23}^2 + \sigma_{33}^2\right)^{1/2} \end{aligned} \tag{7.7}$$

so that the generalized loading direction $\hat{I}_i$ can be defined as

$$L_i = L_1 \hat{e}_i^{(1)} + L_2 \hat{e}_i^{(2)} + L_3 \hat{e}_i^{(3)} \quad ; \quad \hat{I}_i = L_i / (L_k L_k)^{1/2} \tag{7.8}$$

where $\hat{\mathbf{e}}$'s are the unit vectors that define the principal triad in the original Cartesian frame of reference.

Since equation (7.6) must be an isotropic function of stress

$$F\left(\sigma_{ij}, \bar{\eta}(\hat{I}_i)\right) = F\left(T_{ip} T_{jq} \sigma_{pq}, \bar{\eta}(T_{ip} \hat{I}_p)\right) = F\left(I_1, I_2, I_3, \bar{\eta}(\hat{I}_i)\right) = 0 \tag{7.9}$$

where I's are the basic invariants of σ_{ij}. Alternatively, F may incorporate any convenient measures which are derived from the basic invariants. A general form of representation (7.9), pursued further in this chapter, is

$$F = F\left(I, \bar{\sigma}, \theta, \kappa_n(\hat{I}_i)\right) = 0 \tag{7.10}$$

where $I = -\sigma_{ii}$, $\bar{\sigma} = (\tfrac{1}{2} s_{ij} s_{ij})^{1/2}$, $\theta = 1/3 \sin^{-1}\{(\sqrt{3}\, s_{ij} s_{jk} s_{ki})/2\bar{\sigma}^3\}$ and s_{ij} denotes the stress deviator. In equation (7.10), κ_n, $n \in \{1, 2, ..., N\}$ represent a set of material parameters embedded in a typical formulation describing an isotropic response whereas the invariants

$(I, \bar{\sigma}, \theta)$ are chosen to provide a simple geometric interpretation of the failure criterion.

The specification of the failure criterion for bone is rather speculative at this stage, as the experimental information available (e.g., Cowin, 1989; Zysset and Curnier, 1996) is still too fragmentary. At the same time however, the architecture of bone structure bears some analogy to that of a class of cemented granular mixtures. Recognizing this fact, it seems rational to adopt a functional form typically employed for brittle-plastic materials. One particular formulation, describing an isotropic material, is that proposed by Pietruszczak et al. (1988), viz.

$$F = a_1\left(\frac{\bar{\sigma}}{g(\theta)\, f_c}\right) + a_2\left(\frac{\bar{\sigma}}{g(\theta)\, f_c}\right)^2 - \left(a_3 + \frac{I}{f_c}\right) = 0 \qquad (7.11a)$$

or equivalently,

$$F = \bar{\sigma} - g(\theta)\,\bar{\sigma}_c = 0 \quad ; \quad \bar{\sigma}_c = \frac{-a_1 + \sqrt{(a_1^2 + 4a_2(a_3 + I/f_c))}}{2a_2} f_c \qquad (7.11b)$$

Here, the parameters a_1, a_2, a_3 represent dimensionless material constants and f_c denotes the uniaxial compressive strength. Moreover, the function $g(\theta)$ is selected as

$$g(\theta) = \frac{\left(\sqrt{(1+a)} - \sqrt{(1-a)}\right)K}{K\sqrt{(1+a)} - \sqrt{(1-a)} + (1-K)\sqrt{(1 - a\sin 3\theta)}} \qquad (7.12)$$

$$a = \text{const.} \quad (a \to 1)$$

which satisfies $g(\pi/6) = 1$ and $g(-\pi/6) = K$ and for $a = 0.999$ guarantees convexity for $K \geq 0.565$. In general, the material parameters a_1, a_2, a_3 can be identified from standard material tests; i.e. uniaxial compression/tension and biaxial compression. The details on the identification procedure are provided by Pietruszczak et al. (1988). Typically, the strengths in uniaxial tension and biaxial compression are proportional to f_c, so that f_c may be

considered as the only independent parameter.

The simplest extension of equation (7.11) to anisotropic conditions, consistent with representation (7.10), is that in which a's are assumed to remain constant and $f_c = f_c(\hat{I}_i)$,

$$f_c(\hat{I}_i) = f_{co}\left(\frac{\rho}{\rho_o}\right)^{\gamma} = f_{co}\left(\frac{1 - \bar{\eta}(\hat{I}_i)}{1 - \eta_o}\right)^{\gamma} \tag{7.13}$$

Here, ρ is the density of the bone material (considered as orientation-dependent) and γ is a constant, typically within the range $1 \le \gamma \le 2$ (Keller, 1994). In the principal stress space, equation (7.11) represents an irregular cone with smooth curved meridians and a non-circular convex cross-section in the deviatoric (π) plane, as shown in figure 7.1. The shape of the π-plane section is defined through the function $g(\theta)$, equation (7.12).

In general, equation (7.11) together with equation (7.13) define the failure criterion for cortical as well as trabecular bone. In a phenomenological sense, both these tissues are considered to be the same material with different porosity characteristics, equation (7.1), which affect the strength viz. equation (7.13). It is interesting to note that in a special case, when the terms in $\bar{\sigma}^2$ and I are neglected, the general form (7.11) can be reduced to

$$F = \bar{\sigma} - \frac{\sqrt{3}}{3} f_c(\hat{I}_i) = 0 \tag{7.14}$$

which describes an anisotropic von Mises material. Over the last few years a number of researchers have interpreted the contours of $\bar{\sigma}$ as an indicator of the extent of failure. Clearly, representation (7.14) is applicable to pressure-insensitive materials (primarily metals) and has no relevance to the conditions at failure in bone tissue.

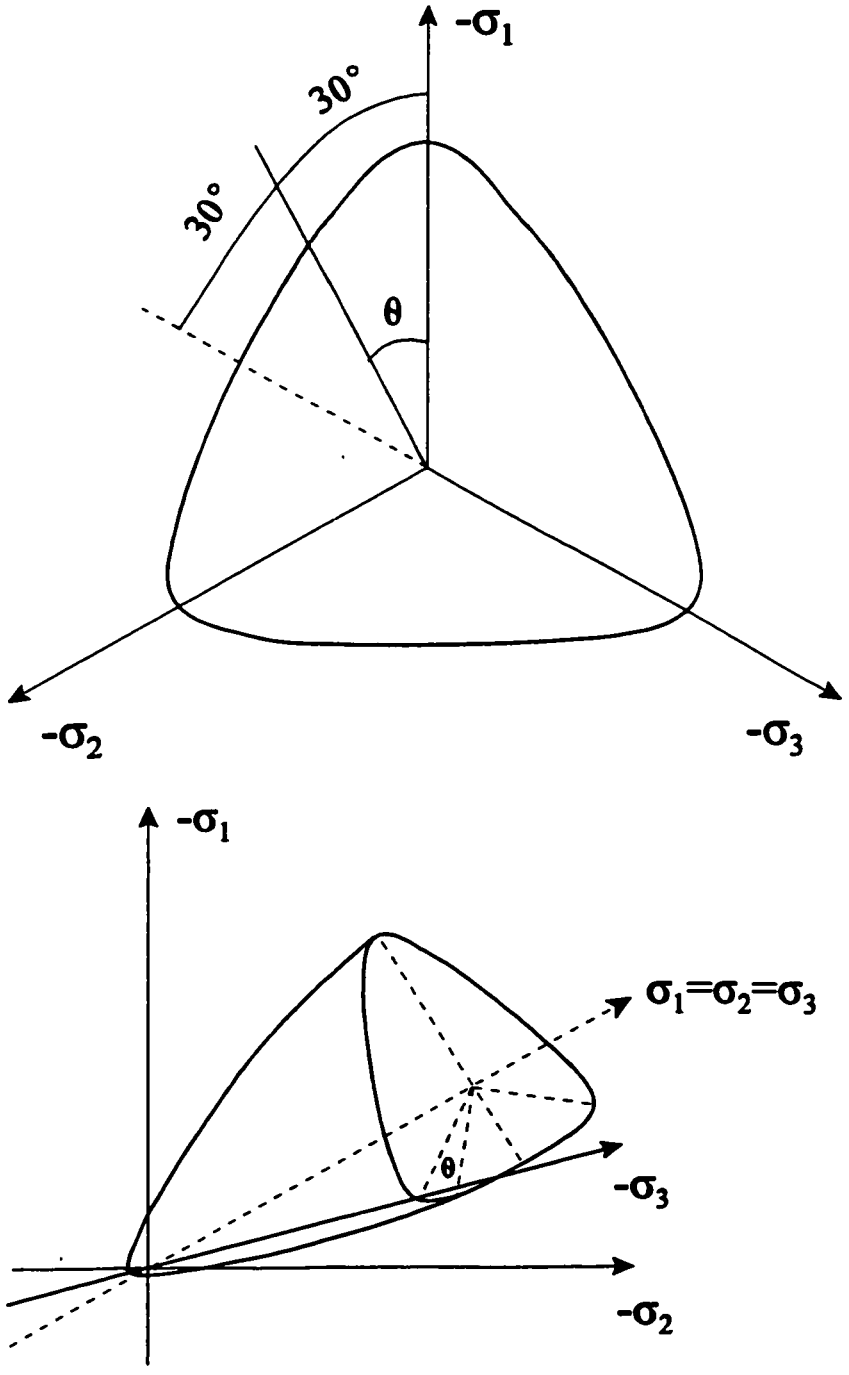

Figure 7.1: Failure surface in principal stress space (for $\bar{\eta}$ = const.).

7.2 Identification of Material Parameters

The first step in quantifying the material response for the numerical analysis that follows is the identification of constants appearing in the failure criterion (7.11). For this purpose, assume that equation (7.11) is satisfied by the stress states corresponding to axial compression ($\sigma_1 = -f_c$, $\sigma_2 = \sigma_3 = 0$), axial tension ($\sigma_1 = \alpha f_c$, $\sigma_2 = \sigma_3 = 0$) and, say, biaxial compression ($\sigma_1 = 0$, $\sigma_2 = \sigma_3 = -\zeta f_c$). Given the definition of stress invariants (I, $\bar{\sigma}$, θ), equation (7.10), the former conditions correspond to ($\bar{\sigma} = f_c/\sqrt{3}$, $I = f_c$, $\theta = \pi/6$), ($\bar{\sigma} = \alpha f_c/\sqrt{3}$, $I = -\alpha f_c$, $\theta = -\pi/6$) and ($\bar{\sigma} = \zeta f_c/\sqrt{3}$, $I = -2\zeta f_c$, $\theta = -\pi/6$), respectively. Moreover, assume that the strength in hydrostatic tension is about 50% of that predicted by a linear form of (7.11) satisfying the conditions of axial tension and biaxial compression. This leads to $a_3 \approx 3\alpha\zeta/[2(\zeta - \alpha)]$. Taking, for example, $\alpha = 0.2$ and $\zeta = 1.2$ gives: $a_1 = 0.69$; $a_2 = 2.88$; $a_3 = 0.36$; $K = 0.80$. Here, both α and ζ (representing the ratios of uniaxial tensile and biaxial compressive strengths to that corresponding to axial tension) have been chosen on an intuitive basis. Clearly, the values of these parameters need to be verified experimentally.

Following the work by Zysset and Curnier (1995), assume now that the orthotropic elastic moduli are defined as

$$E_i = E_o[\rho_s(1 - \eta)]^2 A_i^{-2} \; ; \; G_{ij} = G_o[\rho_s(1 - \eta)]^2 A_i^{-1} A_j^{-1} \; ; \; \mu_{ij} = \mu_o \frac{A_i}{A_j} \quad (7.15)$$

subject to the constraint $\mu_o = E_o/(2G_o) - 1$. In the above expressions, E's and G's are the Young's and shear moduli, respectively, and μ's are the Poisson's ratios. Moreover, $i,j=1,2,3$ ($i<j$), A's are the eigenvalues of the fabric tensor, ρ_s and η represent the density of the tissue and the average porosity, respectively, whereas E_o, G_o, μ_o are material constants.

Assume that the material fabric is orthotropic and is described by $D_1 = -0.15$, $D_2 = 0.04$,

$D_3 = 0.11$. The latter choice gives $E_1/E_3 = 1.7$, $E_1/E_2 = 1.5$ and $G_{12}/G_{23} = 1.3$, $G_{12}/G_{13} = 1.07$, which is consistent with typical experimental data for human femoral bone (Turner and Cowin, 1988) over a broad range of average porosities. To quantify the values of elastic constants, take $\rho_s = 1.93$ g/cm^3, $E_o = 470$ (MPa cm^6/g^2), and $G_o = 180$ (MPa cm^6/g^2), so that for $\eta = 0.05$ there is;

$$E_1 = 19.76 \text{ GPa}, \quad E_2 = 13.15 \text{ GPa}, \quad E_3 = 11.5 \text{ GPa}$$
$$G_{12} = 6.16 \text{ GPa}, \quad G_{13} = 5.72 \text{ GPa}, \quad G_{23} = 4.71 \text{ GPa}$$
$$\mu_{12} = 0.25, \quad \mu_{13} = 0.23, \quad \mu_{23} = 0.29$$

These estimates are consistent with data for human femoral cortical bone, as cited by Turner and Cowin, (1988). Finally, the exponent γ, appearing in the expression for f_c, equation (7.13), is assumed to be equal to 2 (cf. Keller, 1994).

7.3 Finite Element Model Generation

In this section, the procedure for the generation of the 3D FE model of an adult human right femur is described. The heterogeneous nature of the material is addressed by first defining a suitably detailed model from consecutive CT images. The spatial variation of material properties is then estimated from the distribution of average density/porosity derived from the CT data. Here, trabecular and cortical bone are considered to be the same material with different porosity characteristics.

The surface geometry of a right human femur has been defined using a serial reconstruction technique. The cadaver bone obtained for this study had been previously defatted and dried. The specimen was mounted, encased in a perspex cylinder, and filled

with vegetable oil to simulate a soft tissue background during CT scanning. Starting at the proximal end of the femur, 204 consecutive images (512 × 512 pixels, slice thickness: 1 mm) were scanned perpendicular to the long axis of the bone, taken at 1 mm intervals in the proximal region and at 7 mm along the diaphysis. External surface contours were obtained from each image using a boundary extraction program. Contour pixels were mapped to the Cartesian reference frame of the model using a pixel size of 0.219 mm × 0.219 mm and the recorded axial location (i.e., z-axis) along the bone. A subset of control points were chosen by visual inspection and connected, using cubic splines, to form a smooth contour. Three and four-sided surface patches were then created by joining consecutive contours with additional splines. The final closed polyhedron was meshed automatically into four noded tetrahedral elements using COSMOS/M vers. 1.75a (1996) FE software. Figure 7.2 shows the model of the femur which consists of 40681 tetrahedral elements and 9115 nodes.

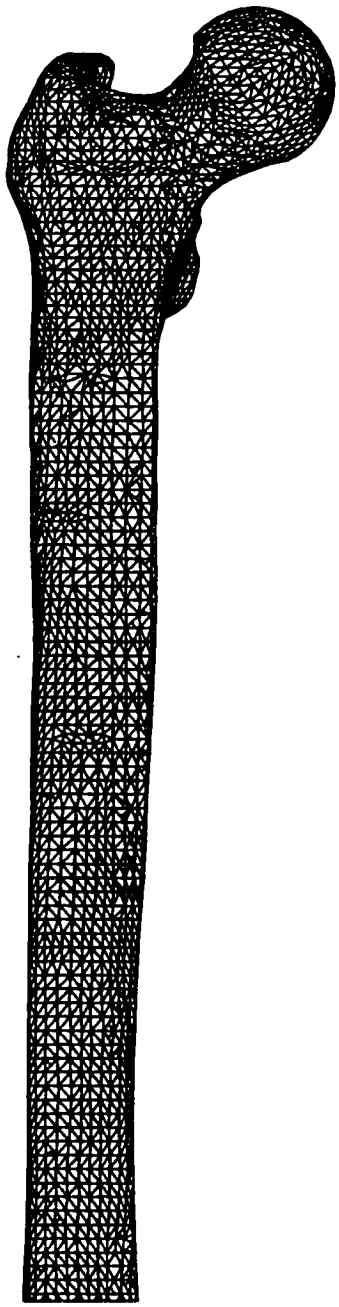

Figure 7.2: 3D Finite element discretization of a femur.

Owing to the spatial resolution of the CT data, a complete description of the material fabric and hence, the specification of the function $\bar{\eta}(v_i)$, was not possible. To define a heterogeneous distribution of bone material properties, a simple algorithm was developed to determine average density/porosity values on an element by element basis. A point inclusion and averaging procedure was applied to each element to assign a relative density value. The Cartesian coordinates of a pixel from a CT scan are readily determined given the known pixel size and z-location of the image plane. For tetrahedral elements, a simple inclusion test may be performed:

$$\frac{\sum_{i=1}^{4} V_i}{V_e} \begin{cases} = 1 \rightarrow \text{inside } V \text{ on} \\ > 1 \rightarrow \text{outside} \end{cases} \tag{7.16}$$

where V_i is the volume of a tetrahedron generated from three nodes and the test point, while V_e is the volume of the test element. The relative density of the pixel in question is determined by interpolation between the linear attenuation coefficients of two phantom image compartments (plastic and oil) and their known respective densities (ρ_p=1.174 g/cm^3, ρ_o=0.914 g/cm^3). A simple geometric average is applied to the subset of pixels contained within the element to arrive at an average relative density. An iterative smoothing procedure is required to address the case in which an element lies between image planes. Elements which fail the inclusion procedure are flagged and then post-processed by finding neighboring elements which share one face (i.e., three nodes in common). An average of the neighboring density values is applied.

An estimate of the average porosity for each element is given by a linear relation based on the CT density values. Consider a pixel on a given image plane with constant thickness. The resulting voxel has volume V representing void spaces filled with oil and the remainder occupied by bone material:

$$V = V_o + V_b \tag{7.17}$$

Dividing by V and recognizing that the porosity and bone volume fraction are now

$$\eta = \frac{V_o}{V} \quad ; \quad 1 - \eta = \frac{V_b}{V} \tag{7.18}$$

then the average density of a CT voxel is given by

$$\rho_{av} = \eta \rho_o + (1 - \eta) \rho_b \tag{7.19}$$

where ρ_b is the maximum density of bone tissue (1.93 g/cm^3) and ρ_o is the known density of oil. Expression (7.19) may be rearranged to give the average porosity:

$$\eta = \frac{\rho_{av} - \rho_b}{\rho_o - \rho_b} \tag{7.20}$$

The porosity contributions of individual voxels contained within an element are averaged as before to give the average element porosity. The image in figure 7.3 shows average porosity contours over a coronal section of the femur. An axial cross section is also presented along with the corresponding original CT image. Low porosity values signifying cortical bone are observed adjacent to the periosteal contour while high values signifying trabecular bone are observed in the proximal region and throughout the medullary canal.

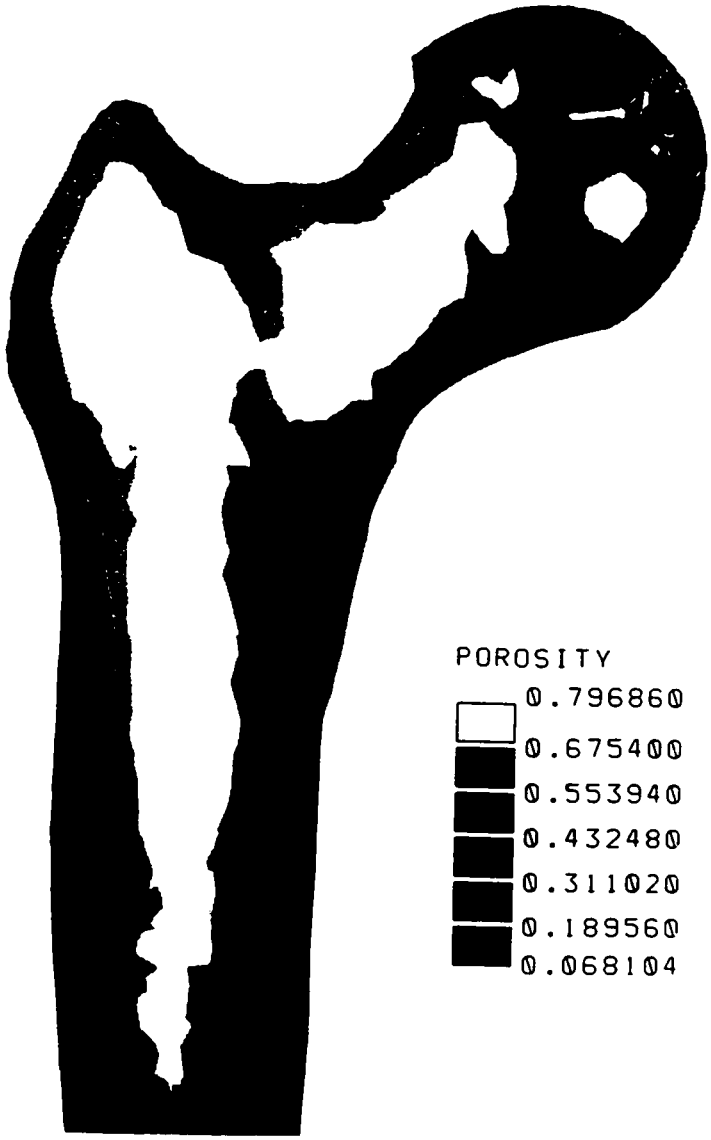

Figure 7.3: Porosity distribution on a coronal plane of the femur model.

7.4 Finite Element Analysis

In this section, a 3D FE analysis of a femur is discussed. The objective of the example given here is to outline a general methodology for assessing the risk of failure in a proximal femur. The numerical analysis is based on the FE method and examines the structural response of femoral bone to a specific type of fall to the lateral aspect of the greater trochanter. A two-stage procedure has been implemented (Pietruszczak et al., 1997) wherein the femur is subjected first to average physiological loads to estimate principal material directions at the element level. The second stage involves the analysis of damage distribution in the femur due to a fall to the hip. The results are presented for a healthy and an osteoporotic bone, simulated by a 20% uniform increase in porosity.

7.4.1 Estimates of Principal Material Directions

The principal directions of anisotropy can be estimated by invoking Wolff's hypothesis of trabecular architecture. The hypothesis states that the principal stress axes coincide with the principal trabecular directions in cancellous bone at remodelling equilibrium. In mathematical terms this implies that the matrix multiplication of σ_{ij} and A_{ij} is commutative, i.e.

$$\sigma_{ip} A_{jp} = \sigma_{jp} A_{ip} \tag{7.21}$$

or, since A_{ij} and D_{ij} are coaxial,

$$A_{ip} D_{jp} = A_{jp} D_{ip} \quad \rightarrow \quad \sigma_{ip} D_{jp} = \sigma_{jp} D_{ip} \tag{7.22}$$

The procedure involves a numerical analysis of a long bone (i.e., a femur) under an average physiological load P_i. The latter may be defined as a weighted average corresponding to typical physical activities:

$$P_i = \sum_{\alpha} \frac{t^{\alpha}}{t_o} P_i^{\alpha} \tag{7.23}$$

where t^{α} is the time interval, within t_o, associated with an activity resulting in P_i^{α}. The problem can be solved by using an iterative scheme under the constraints specified in equation (7.21) or equation (7.22). In particular, a Newton-Raphson procedure may be adopted:

$$(\int_V \mathbf{B}^T \mathbf{D}' \mathbf{B}\, dV)\mathbf{u} = \mathbf{P} + \mathbf{\Psi} \quad ; \quad \mathbf{\Psi} = -\int_V \mathbf{B}^T (\boldsymbol{\sigma} - \boldsymbol{\sigma}')\, dV \tag{7.24}$$

where $\boldsymbol{\sigma}' = \mathbf{D}'\boldsymbol{\varepsilon}$ and $\mathbf{D}'$ is an arbitrarily chosen operator.

It should be emphasized that the simplified procedure, as proposed above, needs to be implemented only in the case when experimental information is insufficient for the specification of the function $\bar{\eta}(v_i)$. Otherwise, the principal directions of anisotropy coincide with those of D_{ij} and thus A_{ij}.

7.4.2 Boundary and Loading Conditions

For both analyses, nodes at the distal end of the femur were rigidly fixed. This boundary condition was considered reasonable since the focus of loading activity and the area of interest was in the proximal end of the femur. Previous analyses (cf. Vichnin et. al, 1986) have shown this to be of little influence on the stress field in the proximal end of the femur.

The loading conditions for the specification of principal material axes are estimated

from the work of McLeish and Charnley (1970), Clark and Haynor (1987), and Kotzar et al. (1991) and simulate the one legged stance phase of gait. This loading configuration was assumed to represent the predominant physiological loading to which the femur is structurally adapted. Resultant loading directions were varied over slight changes in angle in the sagittal plane to simulate a physiological range of mobility, as shown in figure 7.4a. The abductor muscles act with combined magnitude of 2.3×BW (Body Weight = 750 N), with angles of 27° in the frontal plane and 4°, -6°, and -18° in the sagittal plane. Muscle tractions were applied over anatomically relevant groups of nodes defining the insertions of gluteus medius and minimus on the greater trochanter. A joint load of 3×BW acts on the femoral head with angles of 25° in the frontal plane and 5°, -10°, and -25° in the sagittal plane. The joint load was applied over a set of surface nodes of the supero-medial aspect of the femoral head and directed toward the joint center.

The second phase of the analysis involved the numerical simulations of a particular type of fall to the lateral aspect of the greater trochanter. The analysis has been conducted for two different porosity distributions in order to model the effect of degradation of material properties due to aging. The loading configuration for both analyses was derived from the work of Lotz et al. (1991a). A load magnitude of 1×BW was distributed among surface nodes of the lateral aspect of the greater trochanter. An equal and opposite load was applied to the femoral head in a similar manner. Figure 7.4b shows the locations and directions of the resultant loads acting on the femur. The loading magnitude required to initiate failure is consistent with previous experimental work (Backman, 1957; Lotz et al., 1991a; Smith, 1953).

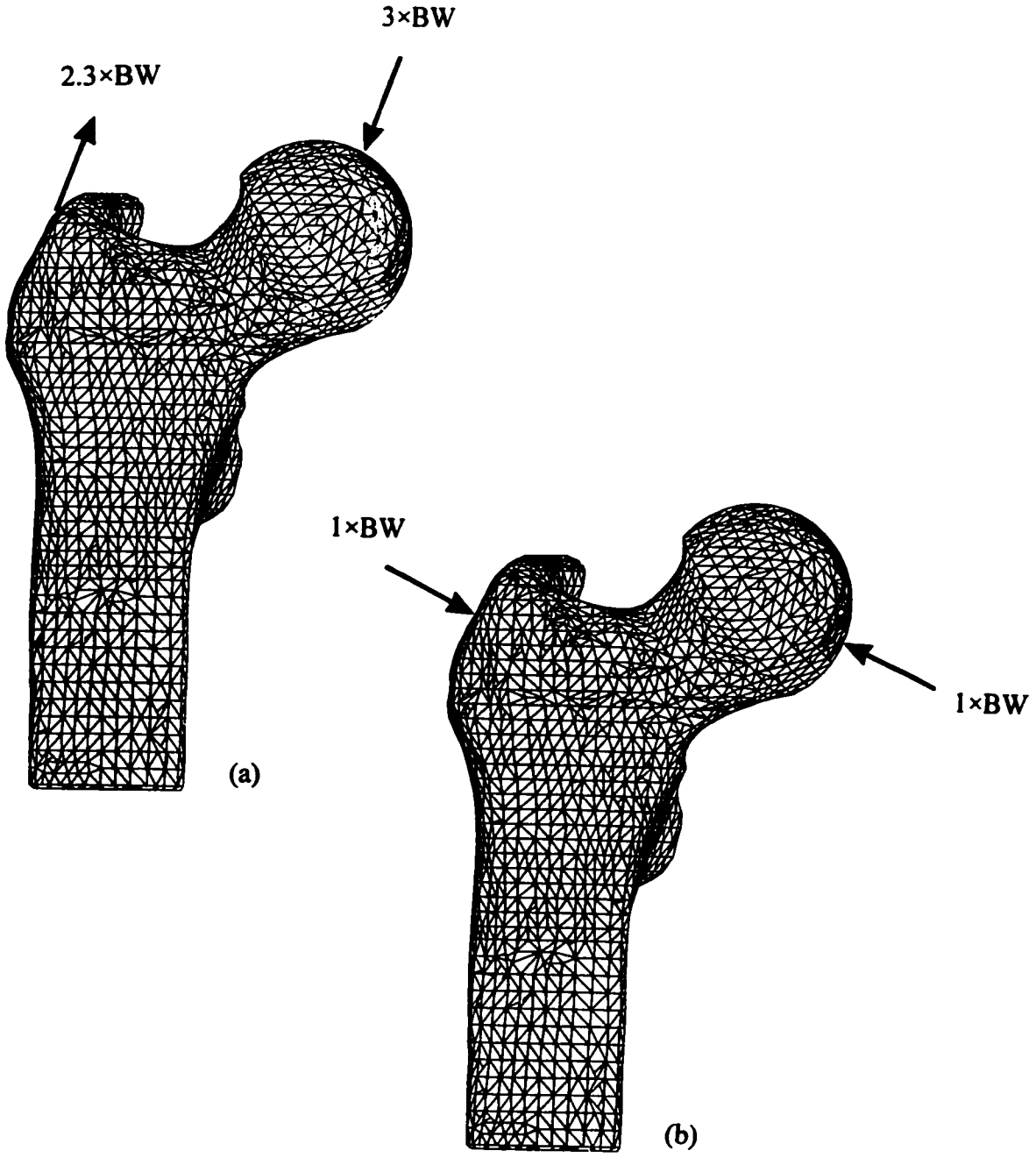

Figure 7.4: Loading configuration for (a) estimation of principal material directions and (b) simulation of a fall to the hip.

7.4.3 Results

The first simulation was carried out using the porosity characteristics derived from the original CT data, figure 7.3, which were considered to reflect a healthy bone. The results are given in figure 7.5, which shows the anterior view of the proximal femur together with superimposed surface distribution of a failure parameter, β, as well as a mid-coronal slice. The failure parameter was defined, based on the proposed failure criterion (7.11), as

$$\beta = \frac{\bar{\sigma}}{g(\theta)\,\bar{\sigma}_c} \tag{7.25}$$

It should be noted that, according to equation (7.11b), $F \le 0$ requires $0 \le \beta \le 1$. The case of $\beta \to 1$ results in $F \to 0$ and signifies the local failure of the bone material associated with formation of macro/micro cracks (e.g., fracture of individual trabeculae). Clearly, $\beta > 1$ is physically inadmissible as the stress state corresponds to $F > 0$.

The results shown in figure 7.5 indicate that, for the case considered, the values of the failure parameter fall within the admissible range of $0 \le \beta < 1$. High concentrations of β (i.e. $\beta \to 1$) are observed near the superior aspect of the femoral neck, implying that in this region the onset of failure will take place. Apparently, the thicker cortical shell along the lower profile of the femoral neck (see figure 7.3) serves to delay the onset of failure within the trabecular region.

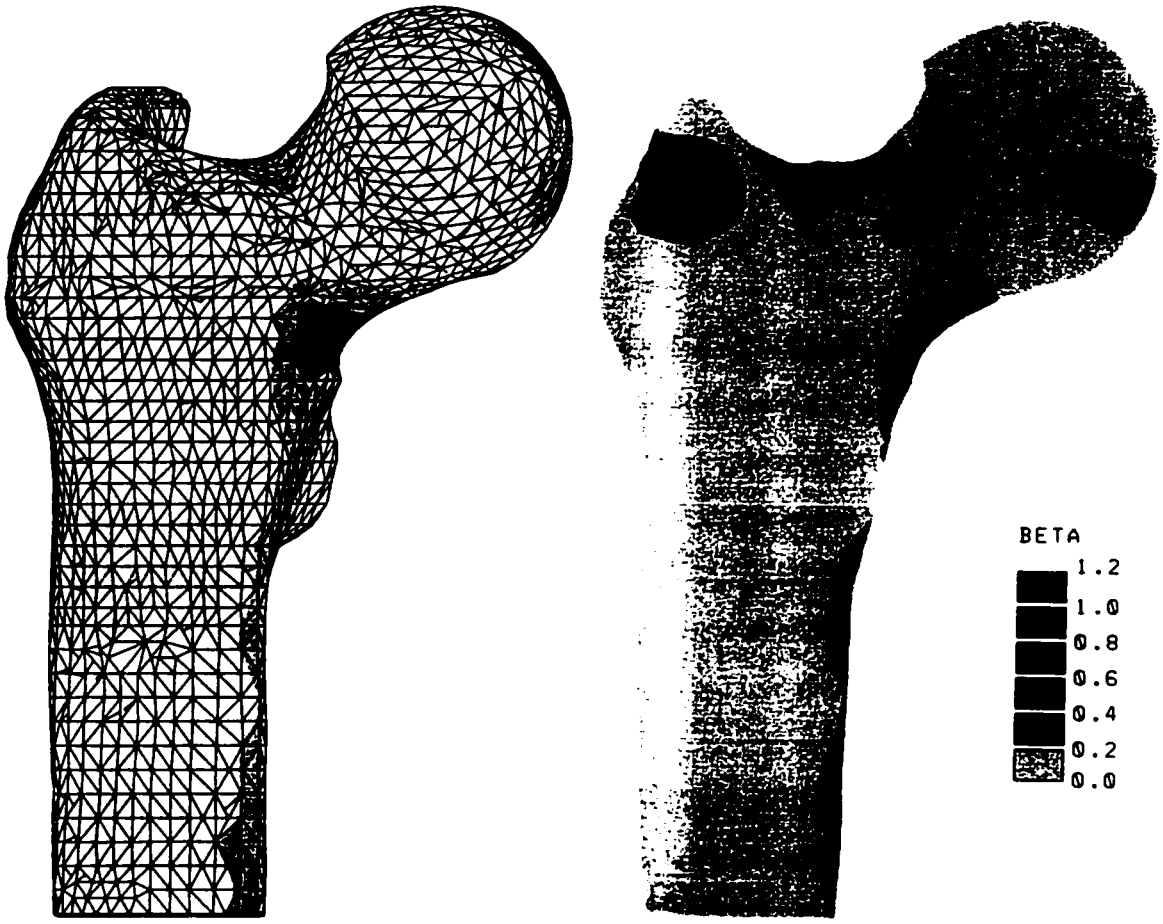

Figure 7.5: Distribution of the failure parameter, β, in a healthy bone.

Consider now the case of degradation of material properties due to aging. In general, the mechanism of aging involves bone resorption leading to an increase in average porosity coupled with evolution of the bone architecture. In order to illustrate the effect of aging on the risk of failure, the numerical analysis discussed above, has been repeated for the case of a 20% uniform increase in average porosity, simulating osteoporotic changes in an aged bone.

The main results of this analysis are given in figure 7.6, which presents the distribution of the failure parameter β. As mentioned earlier, β is formally defined in the interval $0 \leq \beta < 1$ and for $F > 0$ the value of β is, in general, indeterminate. Here, for the purpose of illustration, an arbitrary value of $\beta = 1.2$ was assigned to elements experiencing $F > 0$, in order to identify the domain where the stress field is plastically inadmissible. It is evident from figure 7.6 that the extent of material failure is now quite pronounced. In particular, in the superior and inferior regions of the femoral neck, the stress field violates $F \leq 0$ (i.e. $\beta > 1$). Such a distribution indicates that a lateral fall to the hip could, in this case, trigger a transcervical fracture. The failure zone will initiate at the outer cortical shell and propagate through the trabecular network in the femoral neck.

Apparently, for the case considered here, the proper mathematical solution of the problem requires an inelastic formulation which accounts for the localization of deformation. At this stage, such a solution is not yet feasible. This is primarily due to the lack of adequate experimental data describing the response of the bone material beyond the elastic range. At the same time however, the elastic solution alone, with appropriate interpretation in the context of the proposed failure criterion (7.11), may be sufficient to assess the potential for accidental bone fractures.

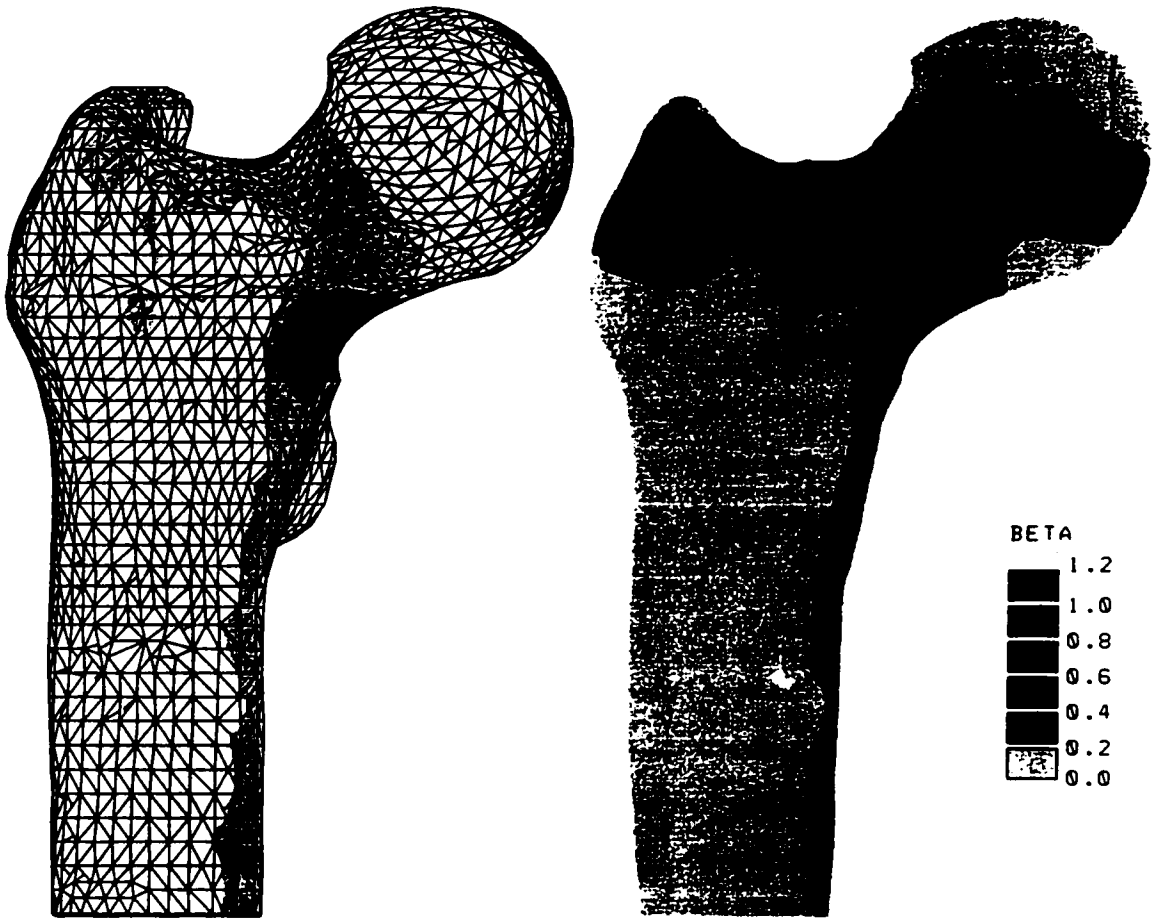

Figure 7.6: Distribution of the failure parameter, β, in a simulated osteoporotic bone.

7.6 Final Remarks

The primary goal of the research presented in this chapter was to provide a comprehensive mathematical framework for the assessment of fracture risk in bones. Within this framework, bone has been considered as an orthotropic elastic material with internal structure. A failure criterion has been proposed incorporating the effect of directional-dependence of strength characteristics.

An example has been provided simulating a femoral neck fracture due to a fall to the lateral aspect of the greater trochanter. The methodology followed here consisted of defining a suitably detailed anatomic model from CT data. The principal material directions were then estimated based on Wolff's hypothesis. Subsequent elastic analyses were conducted to assess the risk of failure under normal and simulated osteoporotic conditions. Distributions of the failure parameter were plotted and checked for regions beyond the physically admissible range.

In a typical scenario involving an accidental bone fracture, the onset of failure will take place in the cortical region. The subsequent propagation of the fracture zone may not require substantial mechanical effort as the trabecular bone is much weaker. Since cortical bone itself is predominantly elastic, it seems therefore reasonable to expect that a simple elastic analysis of the problem, combined with appropriate interpretation of the failure criterion (7.11), may be sufficiently accurate to estimate the potential for risk of failure. Apparently, further studies are required to assess the importance of other factors, in particular the appropriateness of a static analysis and the assumption of a single phase material. Also, additional experimental work is needed in order to identify the basic material parameters as well as to quantify the performance of the proposed failure criterion.

CHAPTER 8 Conclusions And Recommendations

In this chapter, a summary of the major points and conclusions from the preceding chapters is presented. Specifically, the highlights of two main avenues of research are discussed:

1) a unified computational framework for identification of fabric from 3D binary images in terms of combinations of lineal intercept quantities

2) incorporation of a fabric-based constitutive law and failure criterion for bone in finite element analyses

Subsequently, recommendations for future work arising from the research are described. The thesis concludes with some final remarks on bone modelling and fabric detection.

8.1 Summary and Conclusions

It was shown in chapter 1 that bone, in general, is a heterogeneous material with orthotropic symmetry. The anisotropy of bone is attributed primarily to the geometric arrangement of its porous microstructure. To describe its mechanical properties within a constitutive framework, a tensorial measure of material fabric, known as a 'fabric tensor,' was described in chapter 2. Here, the mathematical framework originally presented by Kanatani (1984) for defining distribution density functions in terms of Cartesian tensors was extended in light of recent work by Pietruszczak and Mroz (2001). By incorporating dyadic products of a second order fabric tensor into such functions, rather than pursuing higher order tensor representations, the following are achieved:

- a higher degree of accuracy in fitting directional measurement data
- orthotropic symmetry is retained

- a simple geometric interpretation is preserved
- the eigenvalues of a second order tensor can be correlated with mechanical properties

High resolution imaging techniques, such as micro-CT, afford the data from which 3D measurements of the porous microstructure of bone may be obtained. Specifically, from an arbitrarily oriented array of lineal probes passing through a binary data volume, the basic directionally dependent measurement quantities are:

- L - the length of test lines intersecting the sampling volume (non-spherical case)
- $\sum I^{\alpha}$ - the sum of intercept lengths arising from the intersection of the test lines and the phase of interest raised to a power, α
- N - the number of intercept lengths

The definitions of the descriptors; AP, MIL, MFP, SLD, and SVD, were given in terms of these quantities in section 2.4. Moreover, it was shown that the definition of MFP is algebraically simpler and yet equivalent to MIL. A new measure of fabric, known as areal pore size, APS, was defined. Finally, equations for defining MIL, SLD, and SVD that incorporate the test line spacing directly, were presented as simpler alternatives to the standard definitions appearing in the literature.

In chapter 3, a language independent pseudo-code was introduced for the specification of fabric detection algorithms. The benefits of such a specification are that

- implementation details, such as data structures and language, are left to the discretion of the reader
- algorithms may be scrutinized, checked in detail and optimized before encoding
- algorithms could be made available for use on an open source level

Component algorithms and transformation equations were defined for generating both uniformly and non-uniformly spaced arrays of test lines and for locating their intersections with a sampling domain of simple geometric shape. A bisection search algorithm was

employed as an alternative to the specification of domain dependent and computationally complex geometric intersection tests. Next, a two stage heuristic procedure that minimizes errors in intercept detection was presented, known as the pattern matching algorithm. The errors, or discretization artifacts, arise from the discrete representation of test lines and trabecular bone surface topologies within a binary 3D image space. Aggregate algorithms for obtaining AP, APS, MIL, VF, SLD, and SVD measurements using the line array approach were given. In addition, an isotropic point grid algorithm of the kind described by Odgaard et al. (1990) was presented as an alternative detection method for SLD and SVD measurements. In this thesis, exhaustive and time consuming approaches to sampling (i.e., random orientations) were avoided in favour of a uniform spatial sampling method known as the generalized spiral points method. Chapter 3 concluded with the pseudocode specification of the spiral points algorithm (figure 3.23) as originally described by Saff and Kuijlaars (1997).

In chapter 4, a series of validation tests and performance evaluations of the component and aggregate algorithms were conducted. Exact descriptor solutions were developed for isolated spherical and elliptical inclusions. The efficacy of the bisection search algorithm (figure 3.6) and pattern matching algorithms (figures 3.9 and 3.11) was demonstrated for the case of a 3D binary image of a spherical inclusion. In particular, pattern matching was found most effective for those descriptors that incorporate intercept counts, such as AP, APS, and MIL. The influence of grid spacing on the accuracy of both line array and point grid detection methods was also demonstrated. In both methods, a decrease in measurement error is observed but at the expense of an increase in execution time. A 3D image of a rotated elliptical inclusion was used to assess the orientation detection capabilities of the various descriptors. It was shown that, over a relatively wide range of grid spacings, the detected orientation of the principal axes was in good agreement with the known alignment configuration. Next, the efficiency of the uniform (MIL, SLD, SVD: figure 3.16) and non-

uniform line array algorithms (APS: figure 3.18, AP: figure 3.19) and the point grid algorithm (SLD II, SVD II: figure 3.22) was assessed in terms of time of execution versus grid spacing. For all algorithms, the time of execution increases exponentially with decreasing grid spacing since the number of sampling elements (e.g., grid points, test lines) is inversely proportional to grid spacing. Thus, the AP descriptor is seen as the most expedient since only one 2D set of test lines is used. On the other hand, the APS descriptor is the least efficient since a 3D arrangement of test lines is rotated a number of times around each primary sampling direction. Finally, the uniform line array implementation was found to be generally more efficient than the point grid method for SLD and SVD measurements.

Given a sufficient number of descriptor measurements, a distribution function can be fit to the data and its second order tensor component subjected to an Eigenvalue analysis to characterize the anisotropy of the sample. In chapter 5 it was shown that an ordinary least squares estimate of the parameters appearing in equation (2.8) are insufficient due to problems associated with a lack of homogeneous error variance. Moreover, for orders of fit greater than one, the coefficients become non-linear and a modified data fitting procedure must be employed. Therefore, an iteratively re-weighted least squares procedure was adopted for the linear case (i.e., n = 1: figure 5.1) and then augmented with a Levenberg-Marquardt optimization strategy for the non-linear case (figures 5.3 and 5.4). To determine an appropriate order of fit in a fabric analysis, it was demonstrated that the goodness of fit can be assessed by plotting normalized values of the χ^2 merit function.

Recent advances in 3D tomographic imaging, such as micro-CT, have afforded new opportunities for the identification of fabric in small bone biopsies. As a test of the implementation of the preceding algorithmic framework, and to assess the performance of the various descriptors, fabric analyses of two micro-CT images of trabecular bone biopsies were performed in chapter 6. Graphical presentation techniques for characterizing and

identifying material symmetry information were developed, based on a spectral decomposition of the second order fabric tensor (cf. Westin et al., 1999). Next, a method for determining a suitable sampling resolution was established wherein the known volume fraction, determined by direct voxel counting, is compared to that determined using the uniform line array approach over a wide range of grid spacings.

In both 3D bone images, it was demonstrated, in general, that an order of fit greater than one is necessary to capture fluctuations in descriptor measurements and to produce stable configurations of detected orientation triads. In terms of performance characteristics of the descriptors, APS consistently generated a smooth measurement response which may be attributed to the additional sample averaging around the main pole direction. On the other hand, a considerable amount of fluctuation was observed in the SVD measurements (e.g., figure 6.8), thereby necessitating a higher order of fit to the data and/or an increase in sampling resolution. Furthermore, SVD significantly overestimated the degree of anisotropy when compared with results obtained with the other descriptors, indicating that for the examples considered here, SVD may be an inadequate measure of fabric in trabecular bone (e.g., figures 6.11 and 6.15). However, at this stage, the symmetry results of the fabric analyses should be interpreted with caution, since the correlation of the descriptors with mechanical properties remains to be assessed.

An interesting aspect of fabric analyses which has been neglected in the literature is the assessment of sample homogeneity. It is important, from a modelling viewpoint, that a representative volume of material be established in order to obtain sensible fabric data. For example, in a FE analysis wherein the elements become analogs for sub-volumes of bone material within a larger skeletal structure, a more conservative mesh could be established with larger representative elements. In section 6.5, it was demonstrated that the sample homogeneity could be qualitatively assessed by comparing the anisotropy and orientation

information, derived from a specific descriptor, for different sizes and positions of the sampling domain (i.e., figures 6.15 and 6.16).

In chapter 7, the current potential for improvement in FE modelling of the mechanical behaviour of bone was illustrated through a discussion of material failure in bone tissue. The mathematical details of a fabric-dependent constitutive relation and failure criterion were presented which can be incorporated within FE analyses of bones in general. Next, the material parameters embedded in the mathematical formulation were specified. Specifically, the constants appearing in the failure criterion were chosen on an intuitive basis and remain to be verified experimentally. The orthotropic elastic moduli were then defined based on the work of Zysset and Curnier (1995). Here, the coefficients appearing in equation (7.15) were determined based on typical values reported in the literature. The heterogeneous nature of the material was addressed by first defining a suitably detailed bone model from consecutive CT images, the details of which were provided in section 7.3. The spatial variation of material properties was then estimated from the distribution of average density/porosity derived from the CT data. Trabecular and cortical bone were considered to be the same material with different porosity characteristics. Finally, local principal material triads were estimated by a novel approach in which the femur model was subjected to a range of physiological loads and solved for the average elastic stress field. An iterative FE solution scheme was employed under the constraint that the matrix multiplication of the stress and fabric tensors is commutative, in accordance with Wolff's hypothesis.

The use of the material and geometric model within a FE analysis was illustrated by a numerical example pertaining to the prediction of failure within a femur, under the simulated conditions of a fall to the hip. Static elastic analyses of the femur model were conducted to verify plastic admissibility of the proposed failure criterion. In particular, the distribution of failure within a femur was assessed under two porosity distributions, simulating a healthy

and an aged bone. In a typical scenario involving accidental bone fracture due to a sideways fall to the hip, the onset of failure will take place in the cortical region. The subsequent propagation of the failure zone may not require substantial mechanical effort as the trabecular bone is much weaker. Since cortical bone itself is predominantly elastic, it seems therefore reasonable to expect that a simple elastic analysis of the problem, combined with appropriate interpretation of the failure criterion (7.11), may be sufficiently accurate to estimate the potential for risk of fracture.

8.2 Recommendations for Future Work

To begin, there are several areas for potential improvement in the fabric detection algorithms. Firstly, the pattern matching algorithm, although seemingly effective, is restrictive in the sense that local neighbourhood topologies at the voxel level are not fully taken into account. One way of addressing this issue is to classify local topologies based on the contents of an additional 3D kernel passed over each voxel member of a discrete test line. Another is to avoid voxel stepping altogether and employ a polygonal approximation of the bone-marrow interface, such as that generated by the marching cubes algorithm (Lorenson and Cline, 1987). Here, the intersections between test lines and the triangular surface patches forming an isosurface can be explicitly calculated, thereby mitigating the need for pattern matching or neighbourhood classification. Secondly, in terms of implementation, the current fabric detection program exports raw text data which must be analyzed in various commercial programs. As a step toward distributing the code in the public domain, the subsequent data analysis and display components could be incorporated within the same algorithmic framework. Thirdly, the detection framework remains to be applied to and assessed under a wider variety of bone architectures wherein different degrees of anisotropy are likely to occur. It should be noted that interpretation of the anisotropy information by

means of tensor basis coordinates or by DA is only tentative in nature. The correlation with mechanical properties remains to be ascertained by a comprehensive experimental investigation, which was beyond the scope of the present research.

With regard to the FE modelling reported in this thesis, there are a number of limiting assumptions that remain to be addressed. Further studies are required to assess the importance of other factors, in particular the appropriateness of a static analysis and the assumption of a single phase material. Also, additional experimental work is needed in order to identify the basic material parameters as well as to quantify the performance of the proposed fracture criterion. Furthermore, a major component of research could be the development of a more refined FE model generation procedure from tomographic images of long bones in general. In particular, such models should incorporate the geometric isolation of cortical and trabecular bone compartments to afford a more accurate assignment of mechanical properties. Finally, the experimental validation of finite element models incorporating the proposed constitutive framework remains to be performed.

8.3 Final Remarks

There are several implications from a practical standpoint that arise from the outcomes of this work. In the medical field, the application of 'safe' imaging techniques which do not employ ionizing radiation, such as high resolution MRI, may eventually permit in vivo identification of fabric in living bone tissue for incorporation within FE analyses. Here, it may be possible to assess the risk of fracture through the development of a FE-based clinical software tool. Furthermore, the application of some measures of fabric may be useful in monitoring pathological processes and for assessing the effectiveness of treatments. There is also the potential application of the fabric detection framework developed here for use in experimental studies and characterization of anisotropic permeability in geomaterials.

References

Ashman, R. H., Cowin, S. C., Van Buskirk, W. C., and Rice, J. C. "A continuous wave technique for the measurement of the elastic properties of cortical bone," Journal of Biomechanics, 1984, Vol. 17, pp. 349-361.

Ashman, R. H., Rho, J. Y., and Turner, C. H. "Anatomical variation of orthotropic elastic moduli of the proximal human tibia," Journal of Biomechanics, 1989, Vol. 22, pp. 895-900.

Backman, S. "The proximal end of the femur. Investigations with special reference to the etiology of femoral neck fractures," Acta Radiologica [Suppl.], 1957, Vol. 146.

Bay, B. K., Hamel, A. J., Olson, S. A., and Sharkey, N. A. "Statically equivalent load and support conditions produce different hip joint contact pressures and periacitabular strains," Journal of Biomechanics, 1997, Vol. 30, pp. 193-196.

Beaupre, G. S., and Hayes, W. C. "Finite element analysis of a three-dimensional open-celled model for trabecular bone," Journal of Biomechanical Engineering, 1985, Vol. 107, pp. 249-255.

Brown, T. D., and Pedersen, D. R. "Global mechanical consequences of reduced cement/bone coupling rigidity in proximal femoral arthroplasty: A three-dimensional finite element analysis," Journal of Biomechanics, 1988, Vol. 21, pp. 115-129.

Boehler, J. P. "Applications of Tensor Functions in Solid Mechanics," CISM Courses and Lectures, No. 292, Boehler, J. P., ed., Springer-Verlag, Berlin, 1987.

Burstein, A. H., Reilly, D. T., and Martens, M. "Ageing of bone tissue: Mechanical properties," Journal of Bone and Joint Surgery [Am], 1976, Vol. 58, pp. 82-86.

Carter, D. R., and Spengler, D. M. "Mechanical properties and composition of cortical bone," Clinical Orthopedics, 1978, Vol. 135, pp. 192-217.

Chung, H. W., Wehrli, F. W., Williams, J. L., Kugelmass, D., and Wehrli, S. "Quantitative analysis of trabecular micro structure by 400 MHz magnetic resonance imaging," Journal of Bone and Mineral Research, 1995, Vol. 10, pp. 803-811.

Clark, J. M., and Haynor, D. R. "Anatomy of the abductor muscles of the hip as studied by computed tomography," Journal of Bone and Joint Surgery, 1987, Vol. 69-A, pp. 1021-1031.

COSMOS/M. Finite element analysis system, Structural Research & Analysis Corp., 1996.

Cowin, S. C. "The Mechanical Properties of Bone," Mechanical Properties of Bone, S.C. Cowin, ed., ASME AMD 1981, Vo. 45, pp. 131-143.

Cowin, S. C. "The relationship between the elasticity tensor and the fabric tensor," Mechancis of Materials, 1985, Vol. 4, pp. 137-147.

Cowin, S. C. "Fabric dependence of an anisotropic strength criterion," Mechanics of Materials, 1986, Vol. 5, pp. 251-260.

Cowin, S. C. "Wolff's law of trabecular architecture at remodeling equilibrium," Journal of Biomechanical Engineering., 1986, Vol. 108, pp. 83-88.

Cowin, S. C. Bone mechanics, CRC Press, 1989.

Cowin, S. C. "Remarks on the paper entitled 'Fabric and elastic principal directions of cancellous bone are closely related'," Journal of Biomechanics, 1997, Vol. 30, pp. 1191-1192.

Crowninshield, R. D., Johnston, R. C., Andrews, J. G., and Brand, R. A. "A biomechanical investigation of the human hip," Journal of Biomechanics, 1978, Vol. 11, pp. 75-85.

Currey, J. D. "The effects of porosity and mineral content on the Young's modulus of elasticity of compact bone," Journal of Biomechanics, 1988, Vol. 21, pp. 131-139.

Dalstra, M., Huiskes, R., and van Erning, L. "Development and validation of a three-dimensional finite element model of the pelvic bone," Journal of Biomechanical Engineering, 1995, Vol. 117, pp. 272-278.

Evans, F. G. Mechanical properties of bone, Charles C Thomas, Publisher, 1973.

Etter, D. M. Structured Fortran 77 for scientists and engineers, 4th Edition, Benjamin/Cummings Publ. Co., Redwood Ca. USA, 1993.

Gelfand, I. M., Minlos, R.A., and Shapiro, Z.Y. Representations of the rotation and Lorentz groups and their applications, Pergamon Press, New York, 1963.

Gilbertson, L. G., Goel, V. K., Kong, W. Z., and Clausen, J. D. "Finite element methods in spine biomechanics research," Critical Reviews in Biomedical Engineering, 1995, Vol. 23, pp. 411-473.

Goldstein, S. A., Wilson, D. L., Sonstegard, D. A., and Matthews, L. S. "The mechanical properties of human tibial trabecular bone as a function of metaphyseal location," Journal of Biomechanics, 1983, Vol.16, pp. 965-969.

Goulet, R. W., Goldstein, S. A., Ciarelli, M. J., Kuhn, J. L., Brown, M. B., and Feldkamp, L. A. "The relationship between the structural and orthogonal compressive properties of trabecular bone," Journal of Biomechanics, 1994, Vol.27, pp. 375-389.

Greenwald, A. S., and O'Connor, J. J. "The transmission of load through the human hip joint," Journal of Biomechanics, 1971, Vol. 4, pp. 507-528.

Hampton, S. J., Andriacchi,, T. P., and Galante, J. O. "Three dimensional stress analysis of the femoral stem of a total hip prosthesis," Journal of Biomechanics, 1980, Vol. 13, pp. 443-448.

Harrigan, T. P., and Mann, R. W. "Characterization of micro structural anisotropy in orthotropic materials using a second rank tensor," Journal of Material Science, 1984, Vol. 19, pp. 761-767.

Harrigan, T. P., Jasty, M., Mann, R. W., and Harris, W. H. "Limitations of the continuum assumption in cancellous bone," Journal of Biomechanics, 1988, Vol. 21, pp. 269-275.

Harrigan, T. P., and Harris, W. H. "A three-dimensional non-linear finite element study of the effect of cement-prosthesis debonding in cemented femoral total hip components," Journal of Biomechanics, 1991a, Vol. 24, pp. 1047-1058.

Harrigan, T. P., and Harris, W. H. "A finite element study of the effect of diametral interface gaps on the contact areas and pressures in uncemented cylindrical femoral total hip components," Journal of Biomechanics, 1991b, Vol. 24, pp. 87-91.

Hobatho, D. M., Darmana, R., Pastor, P., Barrau, J. J., Larose, S., and Morucci, J. P. "Development of a three-dimensional finite element model of a human tibia using experimental modal analysis," Journal of Biomechanics, 1991, Vol. 24, pp. 371-383.

Huiskes, R., and Chao, E. Y. S., "A survey of finite element analysis in orthopaedic biomechanics: The first decade," Journal of Biomechanics, 1983, Vol. 16, pp. 385-409.

Huiskes, R., and Hollister, S. J. "From structure to process, from organ to cell: Recent developments of FE-analysis in orthopaedic biomechanics," Journal of Biomechanical Engineering, 1993, Vol. 115, pp. 520-526.

Inglis, D., and Pietruszczak, S. "On fabric descriptors for anisotropic porous media," International Journal of Solids and Structures, 2001, (submitted).

Jara, H., Wehrli, F. W., Chung, H., and Ford, J .C. "High-resolution variable flip angle 3D MR imaging of trabecular microstructure *in vivo*," Magnetic Resonance in Medicine, 1993, Vol. 29, pp. 528-539.

Kalindi, S. R., and Ahmad, P. "A numerical investigation of the mechanics of swelling-type intramedullary hip implants," Journal of Biomechanical Engineering, 1997, Vol. 119, pp. 241-247.

Kanatani, K. "Distribution of directional data and fabric tensors," International Journal of Engineering Science, 1984, Vol. 22, No. 2, pp. 149-164.

Kanatani, K. "Procedures for stereological estimation of structural anisotropy," International Journal of Engineering Science, 1985, Vol. 23, No. 5, pp. 587-598.

Keaveny, T. M., Wachtel, E. F., Ford, C. M., and Hayes, W. C. "Differences between the tensile and compressive strengths of bovine tibial trabecular bone depend on modulus," Journal of Biomechanics, 1994, Vol. 27, pp. 1137-1146.

Keaveny, T. M., and Bartel, D. L. "Fundamental load transfer patterns for press-fit, surface-treated intramedullary fixation stems," Journal of Biomechanics, 1994, Vol. 27, pp. 1147-1157.

Keaveny, T. M., Pinilla, T. P., Crawford, R. P., Kopperdahl, D. L., and Lou, A. "Systematic and random errors in compression testing of trabecular bone," Journal of Orthopaedic Research, 1997, Vol. 15, pp. 101-110.

Keaveny, T. M., Wachtel, E. F., Zadesky, S. P., and Arramon, Y. P. "Application of the Tsai-Wu quadratic multi axial failure criterion to bovine trabecular bone," Journal of Biomechanical Engineering, 1999, Vol. 121, pp. 99-121.

Keller, T. S. "Predicting the compressive mechanical behaviour of bone," Journal of Biomechanics, 1994, Vol. 27, pp. 1159-1168.

Keyak, J. H., Rossi, S. A., Jones, K. A., and Skinner, H. B. "Prediction of femoral fracture load using automated finite element modeling," Journal of Biomechanics, 1998, Vol. 31, pp. 125-133.

Kohles, S. S., Bowers, J. R., Vailas, A. C., and Vanderby, R. Jr. "Ultrasonic wave velocity measurement in small polymeric and cortical bone specimens," Journal of Biomechanical Engineering, 1997, Vol. 119, pp. 232-236.

Kotzar, G. M., Davy, D. T., Goldberg, V. M., Heiple, K. G., Berilla, J., Heiple, K. G. Jr., Brown, R. H., and Burstein, A. H. "Telemetrized in vivo hip joint data: A report on two patients after total hip surgery," Journal of Orthopaedic Research, 1991, Vol. 9, pp. 621-633.

Kuo, A. D., and Carter, D. R. "Computational methods for analyzing the structure of cancellous bone in planar sections," Journal of Orthopaedic Research, 1991, Vol. 9, pp. 918-931.

Kuo, C. Y., Frost, J. D., and Chameau, J. L. A. "Image analysis determination of stereology based fabric tensors," Geotechnique, 1998, Vol. 48, No. 4, pp. 515-525.

Lang, S. B. "Ultrasonic method for measuring elastic coefficients of bone and results on fresh and dried bovine bones," IEEE Transactions on Bio-Medical Engineering, 1970, Vol. 17, pp. 101-105.

Lappi, V. G., King, M. S., and Le May, I. "Determination of elastic constants for human femurs," Journal of Biomechanical Engineering, 1979, Vol. 27, pp. 1159-1168.

Levenberg, K. "A method for the solution of certain nonlinear problems in least squares," Quarterly Journal of Applied Mathematics, 1944, Vol. 2, pp. 164-168.

Little, R. B., Wevers, H. W., Siu, D., and Cooke, T. D.V. "A three-dimensional finite element anlayis of the upper tibia," Journal of Biomechanical Engineering, 1986, Vol. 108, pp. 111-119.

Lorensen, W. E., and Cline, H. E. "Marching cubes: A high resolution 3D surface reconstruction algorithm," Computer Graphics, 1987, Vol. 21, No. 4, pp. 163-169.

Lotz, J. C., Cheal, E. J., and Hayes, W. C. " Fracture prediction for the proximal femur using finite element models: Part I - Linear analysis," Journal of Biomechanical Engineering, 1991a, Vol. 113, pp. 350-360.

Lotz, J. C., Cheal, E. J., and Hayes, W. C. "Fracture prediction for the proximal femur using finite element models: Part II - Nonlinear analysis," Journal of Biomechanical Engineering, 1991b, Vol. 113, pp. 361-365.

Mann, K. A., Bartel, D. L., Wright, T. M., and Burstein, A. H. "Coulomb frictional interfaces in modeling cemented total hip replacements: A more realistic model," Journal of Biomechanics, 1995, Vol. 28, pp. 1067-1078.

Mann, K. A., Ayers, D. C., and Damron, T. A. "Effects of stem length on mechanics of the femoral hip component after cemented revision," Journal of Orthopaedic Research, 1997, Vol. 15, pp. 62-68.

Marom, S. A., and Linden, M. J. "Computer aided stress analysis of long bones utilizing computed tomography," Journal of Biomechanics, 1990, Vol. 23, pp. 399-404.

Marquardt, D. W. "An algorithm for least squares estimation of non-linear parameters," Journal of the Society for Industrial and Applied Mathematics, 1963, Vol. 2, pp. 431-441.

Martin, R. B. "Porosity and specific surface of bone," Critical Reviews in Biomedical Engineering, 1982, Vol. 10, pp. 179-222.

McLeish, R. D., and Charnley, J. "Abduction forces in the one-legged stance," Journal of Biomechanics, 1970, Vol. 3, pp. 191-209.

McNamara, B. P., Viceconti, M., Cristofolini, L., and Taylor, D. "Experimental and numerical pre-clinical evaluation relating to total hip arthroplasty," Computer Methods in Biomechanics & Biomedical Engineering, Middleton, Jones and Pande, eds., Gordon & Breach Publishers, 1996, pp. 1-10.

McNamara, B. P., Cristofolini, L., Toni, A., and Taylor, D. "Relationship between bone-prosthesis bonding and load transfer in total hip reconstruction," Journal of Biomechanics, 1997, Vol. 30, pp. 621-630.

Merz, B., Niederer, P. Müller, R., and Rüegsegger, P. "Automated finite element analysis of excised human femora based on precision-QCT," Journal of Biomechanical Engineering, 1996, Vol. 118, pp. 387-390.

Mourtada, F. A., Beck, T. J., Hauser, D. L., Ruff, C. B., and Bao, G. "Curved beam model of the proximal femur for estimating stress using dual-energy x-ray absorptiometry derived structural geometry," Journal of Orthopaedic Research, 1996, Vol. 14, No. 3, pp. 483-492.

Myers, R. M. Classical and Modern Regression with Applications, 2nd Edition, Boston: PWS-KENT Publishing Company, 1990.

Nambu, T., Gasser, B., Schneider, E., Bandi, W., and Perren, S. M. "Deformation of the distal femur: A contribution towards the pathogenesis of osteochondrosis dissecans in the knee joint," Journal of Biomechanics, 1991, Vol. 24, pp. 421-433.

Odgaard, A., Jensen, E. B., and Gundersen, H. J. G., "Estimation of structural anisotropy based on volume orientation. A new concept," Journal of Microscopy, 1990, Vol. 157, pp. 149-162.

Odgaard, A., Kabel, J., Van Rietbergen, B., Dalstra, M., and Huiskes, R. "Fabric and elastic principal directions of cancellous bone are closely related," Journal of Biomechanics, 1997, Vol. 30, pp. 487-495.

Odgaard, A. "Three-dimensional methods for quantification of cancellous bone architecture," Bone, 1997, Vol. 20, pp. 315-328.

Pietruszczak, S., Jiang, J., and Mirza, F. A. "An elastoplastic constitutive model for concrete," International Journal of Solids and Structures, 1988, Vol. 24, pp. 705-722.

Pietruszczak, S., and Krucinski, S. "Description of anisotropic response of clays using a tensorial measure of structural disorder," Mechanics of Materials, 1989, Vol. 8, pp. 327-249.

Pietruszczak, S., Inglis, D., and Pande, G. N. "Modelling of the mechanical behaviour of a femur with hip prosthesis," Computer Methods in Biomechanical & Biomedical Engineering - II, Jones, Middleton and Pande, eds., Gordon & Breach Publishers, 1997, pp. 289-298.

Pietruszczak, S. "On inelastic behaviour of anisotropic frictional materials," Mechanics of Cohesive Frictional Materials, 1998, Vol. 4, pp. 100-111.

Pietruszczak, S., Inglis, D., and Pande, G. N. "A fabric-dependent fracture criterion for bone," Journal of Biomechanics, 1999, Vol. 32, pp. 1071-1079.

Pietruszczak, S., and Mroz, Z. "On failure criteria for anisotropic cohesive-frictional materials," International Journal for Numerical and Analytical Methods in Geomechanics, 2001, Vol. 25, pp. 509-524.

Press, W. H., Teukolsky, S. A., Vetterling, W. T. and Flannery, B. P. Numerical Recipes in C, The Art of Scientific Computing, Second Edition, Cambridge University Press, Cambridge UK, 1992.

Rakhmanov, E. A., Saff, E. B., and Zhou, Y. M. "Minimal discrete energy on the sphere," Mathematical Research Letters, 1994, Vol. 1, pp. 647-662.

Reilly, D. T., and Burstein, A. H. "The elastic and ultimate properties of compact bone tissue," Journal of Biomechanics, 1975, Vol. 8, pp. 395-405.

Rubin, P. J., Rakotomanana, R. L., Leyvraz, P. F., Zysset, P. K., Curnier, A., and Heegaard, J. H. "Frictional interface micromotions and anisotropic stress distribution in a femoral total hip component," Journal of Biomechanics, 1993, Vol. 26, No. 6, pp. 725-739.

Saff, E. B., and Kuijlaars, A. B. J. "Distributing many points on a sphere," The Mathematical Intelligencer, 1997, Vol. 19, No. 1, pp. 5-11.

Sasov, A. Y. "Microtomography - I. Methods and equipment," Journal of Microscopy, 1987, Vol. 147, pt. 2, pp. 169-178.

Sasov, A. Y. "Microtomography - II. Methods and equipment," Journal of Microscopy, 1987, Vol. 147, pt. 2, pp. 179-192.

Sasov, A. Y., and Van Dyck, D. "Desktop x-ray microscopy and microtomography," Journal of Microscopy, 1998, Vol. 191, pp. 151-158.

Schaffler, M. B., and Burr, D. B. "Stiffness of compact bone: effects of porosity and density," Journal of Biomechanics, 1988, Vol. 21, pp. 13-16.

Smit, T. H., Schneider, E., and Odgaard, A. "Star length distribution: a volume-based concept for the characterization of structural anisotropy," Journal of Microscopy, 1998, Vol. 191, pt. 3, pp. 249-257.

Smith, L. D. "Hip fracture: The role of muscle contraction or intrinsic forces in the causation of fractures of the femoral neck," Journal of Bone and Joint Surgery [Am], 1953, Vol. 35, pp. 367-382.

Standish, T. A. Data Structures, Algorithms and Software Principles in C, Addison-Wesley Publishing Company, Inc., USA, 1995.

Stone, J. L., Beaupre, G. S., and Hayes, W. C. "Multiaxial strength characteriastics of trabecular bone," Journal of Biomechanics, 1983, Vol. 16, pp. 743-752.

Taylor, M., Tanner, K. E., Freeman, M. A. R., and Yettram, A. L. "Cancellous bone stresses surrounding cemented and press fit femoral components of a Freeman hip prosthesis in relation to clinical migration", Computer Methods in Biomechanics & Biomedical Engineering, Middleton, Jones and Pande, eds., Gordon & Breach Publishers, 1996, pp. 47-55.

Torzilli, P. A., Takebe, K., Burnstein, A. H., and Heiple, K. G. "The structural properties of immature canine bone," Journal of Biomechanical Engineering, 1981, Vol. 103, pp. 232-238.

Tsai, S. W., and Wu, E. M. "A general theory of strength for anisotropic materials", Journal of Composite Materials, 1971, Vol. 5, pp.58-80.

Turner, C. H., and Cowin, S. C. "Errors induced by off-axis measurements of the elastic properties of bone," Journal of Biomechanical Engineering, 1988, Vol. 110, pp. 213-215.

Turner, C. H., Cowin, S. C., Rho, J. Y., Ashman, R. B., and Rice, J. C. "The fabric dependence of the orthotropic elastic constants of cancellous bone," Journal of Biomechanics, 1990, Vol. 23, pp. 549-561.

Underwood, E. E. Quantitative Stereology, New York: Addison-Wesley, 1970.

Van Buskirk, W. C., Cowin, S. C., and Ward, R. N. "Ultrasonic measurements of orthotropic elastic constants of bovine femoral bone," Journal of Biomechanical Engineering, 1981, Vol. 103, pp. 67-71.

Van Rietbergen, Odgaard, A., Kabel, J., and Huiskes, R. "Direct mechanics assessment of elastic symmetries and properties of trabecular bone architecture," Journal of Biomechanics, 1996, Vol. 29, pp. 1653-1657.

Verdonschot, N., and Huiskes, R. "The effects of cement-stem debonding in THA on the long-term failure probability of cement," Journal of Biomechanics, 1997, Vol. 30, pp. 795-802.

Vichnin, H. H., and Batterman, S. C. "Stress analysis and failure prediction in the proximal femur before and after total hip replacement," Journal of Biomechanical Engineering, 1986, Vol. 108, pp. 33-41.

Weibel, S. Stereological methods: theoretical foundations, Academic Press, London, 1980.

Weinans, H., Huiskes, R., and Grootenboer, H. J. "Quantitative analysis of bone reactions to relative motions at implant-bone interfaces," Journal of Biomechanics, 1993, Vol. 26, pp. 1271-1281.

Westin, C. F., Maier, S. E., Khidhir, B., Everett, P., Jolesz, F. A., and Kikinis, R. "Image Processing for Diffusion Tensor Magnetic Resonance Imaging," Medical Image Computing and Computer Assisted Intervention – MICCAI'99, proceedings, C. Taylor and A. Colchester (Eds.), Springer, 1999, pp. 441-452.

Whitehouse, W. J. "The quantitative morphology of anisotropic trabecular bone," Journal of Microscopy, 1974, Vol. 101, pt. 2, pp. 153-168.

Williams, J. L., and Lewis, J. L. "Properties and an anisotropic model of cancellous bone from the proximal tibial epiphysis," Journal of Biomechanical Engineering, 1982, Vol. 104, pp. 50-56.

Zioupos, P., and Currey, J. D. "Changes in the stiffness, strength, and toughness of human cortical bone with age," Bone, 1998, Vol. 22, pp. 57-66.

Zysset, P. K., and Curnier, A. "An alternative model for anisotropic elasticity based on fabric tensors," Mechanics of Materials, 1995, Vol. 21, pp. 243-250.

Zysset, P. K., and Curnier, A. "A 3D damage model for trabecular bone based on fabric tensors," Journal of Biomechanics, 1996, Vol. 29, pp. 1549-1558.

APPENDIX A Algorithm Summary

A number of algorithms have been developed for deriving the fabric descriptor measurements outlined in section 2.4. In this section, a summary is provided in table A.1 below to clarify the relations amongst the different algorithms and the variables used in chapters 3 and 5.

Algorithm	**Figure, Page**	**Calling Arguments**	**Return Arguments**
GetGridSize	3.3, 36	δ	N_δ
GetUniformLineArray	3.4, 36	δ, N_δ	X
GetProjectedLineArray	3.5, 38	X, **A**, **v**	P
GetBoundaryPoint	3.6, 39	$\mathbf{p}_1$, $\mathbf{p}_2$, δ_b	**t**
GetTestLineSegments	3.7, 40	P, **v**, δ_b	T
GetLinePattern	3.9, 42	**p**, **v**, C_S	Q
GetInterceptLengths	3.11, 44	Q, $\mathbf{t}_1$, $\mathbf{t}_2$, $\hat{\mathbf{v}}$, C_S	I
GetLengthOfTestLines	3.14, 46	T, $\hat{\mathbf{v}}$	L
GetVoxelCounts	3.15, 46	C_S	N^T, N^P
ScanUniformLineArray	3.16, 48	Θ, Φ, δ, δ_b, C_S	VF, MIL, SLD, SVD
GetNonUniformLineArray	3.17, 50	δ, N_δ	X
ScanNonUniformLineArray	3.18, 52	Θ, Φ, N_ψ, δ, δ_b, C_S	APS
ScanEquatorialLineArray	3.19, 53	Θ, Φ, N_ψ, δ, δ_b, C_S	AP

GetPointGrid	3.20, 54	δ, N_δ, C_S	X
GetEndOfIntercept	3.21, 55	**x**, **v**, δ_b, C_S	**p**
ScanPointGrid	3.22, 56	Θ, Φ, δ, δ_b, C_S	SLD, SVD
GetSpiralPoints	3.23, 58	N	Θ, Φ

Table A.1: Summary of fabric detection algorithms.

A summary of the algorithms appearing in chapter 5 for fitting fabric data are given below in table A.2.

Algorithm	**Figure, Page**	**Calling Arguments**	**Return Arguments**
IRWLS	5.1, 87	**X**, **y**, δ_e	**a**
LevenbergMarquardt	5.3, 91	**W**, $\mathbf{a}_0$, λ_0, δ_λ, δ_s, N	**a**, $\hat{\boldsymbol{\varepsilon}}$, n
IRWNLLS	5.4, 92	**X**, **y**, δ_e, λ_0, δ_λ, δ_s, N	**a**, n

Table A.2: Summary of fabric data fitting algorithms.

APPENDIX B DA from MIL Measurements

A distribution function of the form described in chapter 2 does not appear in the literature pertaining to the MIL tensor. Therefore, the second order tensor appearing in equation (2.8) is not the same as that specified by Harrigan and Mann (1984). Here, DA is defined as a ratio based on the maximum and minimum eigenvalues of the following matrix:

$$M = \begin{bmatrix} A & \frac{D}{2} & \frac{E}{2} \\ \frac{D}{2} & B & \frac{F}{2} \\ \frac{E}{2} & \frac{F}{2} & C \end{bmatrix} \quad ; \quad DA = \frac{\sqrt{|\lambda_3|}}{\sqrt{|\lambda_1|}} \tag{B.1}$$

the coefficients of which are derived from least squares fitting of MIL data to the equation of an ellipsoid:

$$A\hat{v}_1^2 + B\hat{v}_2^2 + C\hat{v}_3^2 + D\hat{v}_1^2\hat{v}_2^2 + E\hat{v}_1^2\hat{v}_3^2 + F\hat{v}_1^2\hat{v}_3^2 = 1/MIL(\hat{v})^2 \tag{B.2}$$

A least squares fit of equation (B.2) to MIL measurements obtained with the algorithm in figure 3.16 was established for both micro-CT images (i.e., see section 6.2). A Mathematica code (vers. 4.0.1.0, ©1988 - 1999, Wolfram Research, Inc.) was developed for this purpose and is repeated here for convenience.

Load Packages:

```
<< Statistics`
<< Statistics`DescriptiveStatistics`
```

Macro function to read data from a given ASCII text file generated by Fabric3D analysis program. Input: full path double slash delimited in double quotes. Output: table of raw file data.

```
readDataFun [str_ ] := Drop[Rest [ReadList [str, Number, RecordLists -> True]], -2];
```

Macro function to convert raw data from readDataFun[] output into a useable table form of: v_1, v_2, v_3, y where v_i are components of a unit direction vector associated with fabric measurement y. 'dat' is a matrix of column ordered data output from the fabric detection code.

```
getDataToFitFun [ dat_, col_ ] := Transpose [ Table [ {Sin [ dat [ [All, 1] ] ] Cos [
        dat[[All, 2]] ], Sin [ dat[[All, 1]] ] Sin [ dat[[All, 2]] ], Cos [ dat[[All, 1]] ],
        1.0 / ( dat[[All, col]] dat[[All, col]]) } ] ];
```

The procedure starts here:

```
filestr = Experimental`FileBrowse [ False ];
rawdat = readDataFun [ filestr ];
dat = getDataToFitFun [ rawdat, col ];
fullreport = { BestFit, BestFitParameters, ANOVATable, EstimatedVariance,
ParameterTable, PredictedResponse, FitResiduals };
linregressdat = Regress [ dat, { v1^2, v2^2, v3^2, v1 v2, v1 v3, v2 v3 }, { v1, v2, v3 },
```

```
RegressionReport → fullreport, IncludeConstant → False ];
fits = BestFitParameters /. linregressdat;
M = { { fits[[1]], fits[[4]] / 2.0, fits[[5]] / 2.0},
      { fits[[4]] / 2.0, fits[[2]], fits[[6]] / 2.0},
      { fits[[5]] / 2.0, fits[[6]] / 2.0, fits[[3]] }};
evm = 1.0 / Sqrt [ Abs [ Eigenvalues[ M ] ] ];
da = Max [ evm ] / Min [ evm ];
```